Mechanics of Proton Exchange Membranes: Time, Temperature, and Hydration Dependence of the Stress-Strain Behavior of Persulfonated Polytetrafluorethylene

by

Meredith Natania Silberstein

Bachelor of Science
Massachusetts Institute of Technology, 2005

Submitted to the Department of Mechanical Engineering
in partial fulfillment of the requirements for the degree of

MASTER OF SCIENCE IN MECHANICAL ENGINEERING

at the

MASSACHUSETTS INSTITUTE OF TECHNOLOGY

~~January 2008~~
[February 2008]

Author . . . .

Department of Mechanical Engineering
January 22, 2008

Certified by . . . .

Mary C. Boyce
Kendall Family Professor of Mechanical Engineering
Thesis Supervisor

Accepted by . . . .

Lallit Anand
Chairman, Department Committee on Graduate Students

Mechanics of Proton Exchange Membranes:
Time, Temperature, and Hydration Dependence of the Stress-Strain Behavior of Persulfonated Polytetrafluorethylene

by

Meredith Natania Silberstein

Submitted to the Department of Mechanical Engineering
on Jan 22, 2008, in partial fulfillment of the
requirements for the degree of
MASTER OF SCIENCE IN MECHANICAL ENGINEERING

Abstract

Fuel cells are an important part of the future strategy for reducing dependence on fossil fuels as the world's supplies become more limited and greenhouse gasses become more of a concern. Proton Exchange Membrane Fuel Cells (PEMFC), in which protons from hydrogen gas are passed across a membrane to react with oxygen gas producing electricity, with water as the only waste product, are a cleaner and potentially more efficient chemical energy conversion method. However, the current usefulness of PEMFC is limited by the lifespan and high cost of the fuel cell unit, and more specifically the membrane electrode assembly (MEA). At the center of most contemporary MEA is a thin membrane ($\sim 25 - 100\mu m$ thick) of persulfonated polytetrafluoroethylene manufactured by Dupont and known commercially as Nafion. Nafion has the unique quality of being microphase separated into hydrophobic and hydrophilic domains composed of backbone rich and sulfonic acid side chain rich regions respectively. This polymer electrolyte membrane is responsible for rapidly conducting the protons from the hydrogen side to the oxygen side while preventing electrons, hydrogen, and oxygen from passing through. Because of this selective permeability requirement it is important that the membrane possess good mechanical durability so that it does not form pinholes during operation (something which it has been shown to do experimentally). The goal of this thesis was to develop an understanding of the mechanical properties of Nafion as well as a comprehensive material model that captures all the features that are important to how a membrane deforms in an operational fuel cell, including the time, temperature, and hydration dependence of the elastic regime, yield, strain hardening, and stress relaxation at low to moderate strains. In order to accomplish this understanding a comprehensive experimental study was undertaken in which Nafion was characterized in uniaxial tension under monotonic, cyclic, and stress relaxation loading profiles at strain rates from $0.001/s$ to $0.1/s$, temperatures from 25^oC to 100^oC, and from dry to fully hydrated conditions. The evolution of the microstructure with applied deformation was then investigated with diffraction techniques. Wide and small angle x-ray scattering data was collected during uniaxial tensile monotonic extension, cyclic, and stress relaxation loading profiles. The SAXS peaks and two WAXS peaks were seen to be isotropic in the initial state. Their evolution with strain was interpreted to indicate that the ionic clusters deform to an elliptical shape with major axis parallel to the tensile direction with an applied strain, whereas the backbone segments align themselves parallel to the tensile direction with an applied strain. Combining these results with those in literature we revise an existing conceptual model for how each of the micromechanical features evolves with strain and how that contributes to the stress response. From mechanical and microstructural data, a constitutive model was developed which is able to capture the key features of the mechanical behavior of Nafion as functions of time, temperature, and hydration. The model is then applied to a simulated fuel cell. The results from the fuel cell simulations indicate that the hypothesis that cyclic stress states and permanent membrane deformation result from hygro-thermal cycling and can lead to pinhole formation.

Thesis Supervisor: Mary C. Boyce
Title: Gail E. Kendall Professor of Mechanical Engineering

Acknowledgements

Firstly, I wish to thank my advisor Mary C. Boyce who has been teaching me for just about six years now. There have been a lot of highs and lows (and I'm sure many more to come) but I still consider stopping by your office to ask for help finding a UROP position the best decision I've ever made. You continue to amaze me with your enthusiasm, work ethic, and insight.

I would like to thank the mechanics and materials group for answering all my programming and continuum questions and for providing a pleasant work environment, who'd have I thought I would like working in a not-quite-windowless basement. In particular I need to thank Shawn Chester for all the technical support with Abaqus and Latex and for continually being faster than both email and the internet. And of course Una and Ray, without whom we'd all be lost.

I'd also like to express my appreciation towards Yang Shao-Horn and her research group for letting my crash their group meetings and use their equipment and teaching me all about fuel cells. Ethan Crumlin, thanks for designing and building a water chamber for my tensile tests, that data is awesome. I feel like we've come a long way from 2.003 problem sets.

Thanks to David Londono and the rest of the Dupont guys for setting up all the x-ray scattering equipment. And for not getting mad when we crashed the Instron into the beam source.

And of course I can't leave out my family, friends, and sMITe. Adam and Rebecca, your empathy was much appreciated this past year, I'm glad I wasn't the first in the family to go through the PhD process. Lynne, thanks for being my only friend not to call me crazy when I decided to come back here, and for listening for endless hours to every detail of my life and research troubles even when you have no idea what I'm talking about.

This work was supported in part by the MIT Vest Institute Fellowship and in part by the National Science Foundation grant CMMI-0700414.

Contents

List of Figures

List of Tables

1 Introduction

Fuel cells are an important part of the future strategy for reducing dependence on fossil fuels as the world's supplies become more limited. Their direct chemical to electrical method allows for a cleaner and more efficient conversion of fuel to useable energy. Proton Exchange Membrane Fuel Cells (PEMFC), in which protons from hydrogen gas are passed across a membrane to react with oxygen gas producing electricity, with water as the only waste product, are the preferred fuel cells for power conversion. However, the current usefulness of PEMFC is limited by the lifespan and high cost of the fuel cell unit. Both the lifespan and cost of the unit are driven by the membrane electrode assembly (MEA) which consists of a selectively permeable membrane with a catalyst layer and porous carbon electrode support on each side. Particularly in the unsteady operating conditions of automobiles, the MEA fails far earlier than the required lifespan. The membrane is known to develop pinholes in operation, which then allows crossover of the hydrogen and oxygen gasses, decreasing and eventually stopping electricity generation. The cause of pinhole formation is unknown but one of the leading theories is that it is related to mechanical stress in the membrane caused by the hygro-thermal cycling. However, little research has been conducted to date to build an understanding of the MEA mechanics.

Fuel cells are a technology which converts chemical energy directly into electrical energy. In this regard they are similar to batteries, however, unlike batteries the fuel supply is replenishable. They are an appealing alternative to traditional combustion engines because they are not theoretically limited to the Carnot efficiency. PEMFC are typically the fuel cells chosen for low temperature and low pressure applications. In particular, people are looking to PEMFC to replace internal combustion engines in vehicles. The fuel for PEMFC is typically hydrogen but also sometimes methane or other hydrocarbons. In a hydrogen PEMFC the fuel is passed through gas channels at the anode where it is reacted with a catalyst that splits it into positive hydrogen ions and electrons. The hydrogen ions pass through an electrolyte membrane to the cathode while the electrons are forced to travel around a circuit in which power is extracted. At the cathode the hydrogen ions and electrons are reacted with oxygen at a second catalyst layer to form water as the waste byproduct (Figure 1). Fuel cell units are arranged in stacks in order to achieve a usable voltage and power

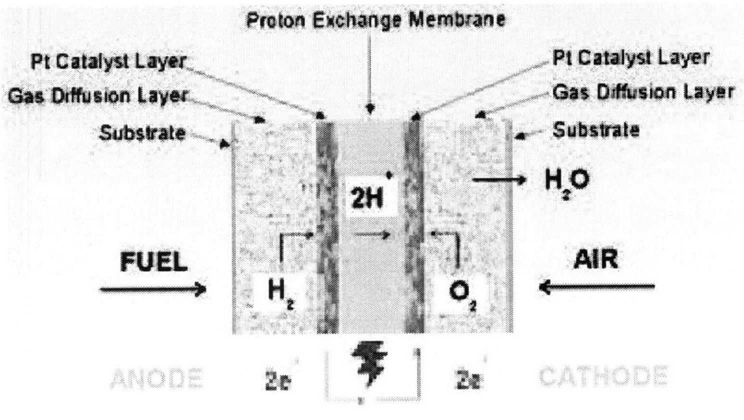

Figure 1: Schematic of proton exchange membrane fuel cell (PEMFC) from Johnson Matthey Fuel Cells.

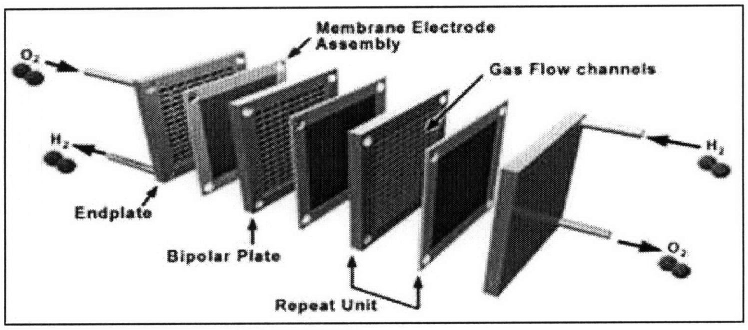

Figure 2: Schematic of fuel cell stack from Kar (2005).

output (Figure 2).

The choice of material for the polymer electrolyte membrane (PEM) is critical to fuel cell efficiency. The PEM needs to have high proton conductivity, high selectivity to prevent the electrons and oxygen from passing through, and high durability to survive long term and unsteady operation. Fuel cell membranes generally have the least ionic resistance and therefore highest efficiency when they are well hydrated and at elevated temperatures. Nafion, the perfluorosulfonated ionomer manufactured by Du Pont de Nemours and Company, is the current benchmark membrane for PEMFC. It consists of a polytetrafluoroethylene backbone with sulfonic acid side chains as shown in figure 3. This results in a material that is micro-phase separated into hydrophobic and hydrophillic regimes (Figure 4) .

Proton conduction through Nafion occurs through one of two mechanisms. The first is a hopping

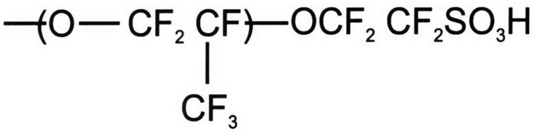

$-\!\!\left(O-CF_2\,\underset{\displaystyle CF_3}{\underset{|}{C}F}\right)\!\!-OCF_2\,CF_2SO_3H$

Figure 3: Chemical structure of Nafion.

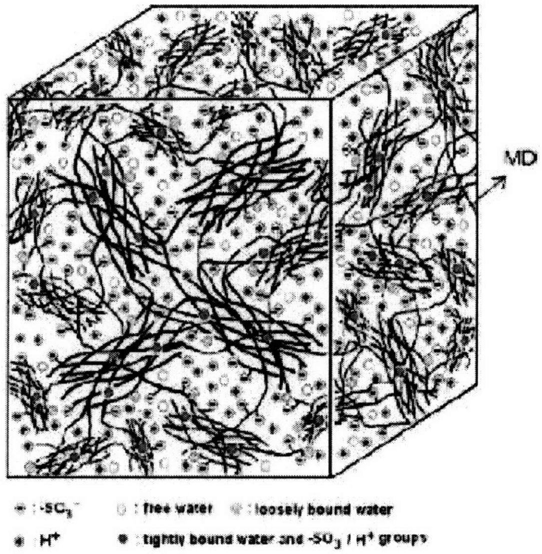

Figure 4: Three dimensional schematic of the microphase separated structure of Nafion from Liu, Kyriakides et. al. (2006).

mechanism in which the protons are passed among the fixed negative charge sulfonic side chains; this method dominates at low to moderate hydration levels. At high hydration levels the protons are able to attach to the water molecules and flow through channels in the membrane at a much faster rate; this second method is referred to as a vehicular mechanism. The vehicular mechanism is highly preferable as its faster conduction translates to a lower ionic resistance and therefore lower ohmic losses. Since conductivity is also exponentially related to temperature, Nafion based fuel cells should be run at as high a temperature as possible without boiling off the water.

In order to optimize performance PEMFC are generally operated between 80^oC and 90^oC with humidified gas feeds. However, when fuel cells are not in operation they are allowed to dry out and cool down to room temperature. It is believed that this transitioning between the cold-dry state and the wet-hot state leads to mechanical degradation which strongly contributes to the ultimate failure of the membrane. The hygro-thermal cycling negatively affects the membrane through two superimposed mechanisms. The first is the reduction in stiffness, strength, and toughness as a direct result of the elevated temperature and water content. The second arises from the combined effect of the physical constraints placed on the MEA by the fuel cell stack and the swelling that occurs when the membrane is infused with water. The membrane is constrained in-plane by a gasket which seals the hydrogen and oxygen gas in for each layer of the fuel cell stack, and out-of-plane by a the porous carbon gas diffusion layer ($\sim 100\mu m$ thick, $E = 20MPa \rightarrow 1GPa$) and the bipolar plate ($\sim 10mm$ thick, $E = 10GPa$). The cycling to and from these extreme loading conditions is thought to accumulate damage which unfortunately degrades the membrane performance. While the teflon-like backbone provides a relatively stiff support in which the liquid-like vehicular conduction can take place the membrane is still not durable enough for use in commercial vehicles. Current PEMFC in automobiles fail at 2000 hours, less than half the target lifespan of 5500 hours.

The goal of this research is twofold: to better understand the microstructure of Nafion so that other materials can be synthesized which mimic the good features and improve upon the poor, and to accurately model the mechanical behavior of Nafion so that short term design solutions can be proposed to improve fuel cell durability. This thesis aims to understand and model the fuel cell relevant mechanical properties of Nafion, in particular the time, temperature, and hydration dependent stress-strain behavior. Chapter 2 first reviews the mechanical studies on Nafion that have been done to date and then presents and discusses the tensile testing that I have conducted. Chapter 3 reviews the current understanding of Nafion microstructure as deciphered by SAXS, WAXS, and microscopy. It then presents results from SAXS and WAXS conducted while Nafion was subjected to different uniaxial tensile loading conditions. Chapter 4 develops the constitutive model both theoretically and mathematically. The model predictions are compared to the experimental data. In chapter 5 the model is applied to an idealized fuel cell system. The final chapter discusses future directions for this work both in terms of modeling of Nafion as well as PEMFC membrane design.

2 Mechanical Testing

2.1 Mechanical Properties Background

Research on the mechanical properties of Nafion since its synthesis in the late 1960's has been fairly limited. Only in the last five years have researchers begun to study it as an important component of fuel cell design.

Yeo and Eisenberg (1977) conducted the first comprehensive study of the physical properties of Nafion which included drying and thermal stability, water diffusion, glass transition temperature, stress relaxation, dynamical mechanical testing, dielectric evaluation, and xray diffraction. This was followed by Takamatsu and Eisenberg (1979) which determined the density and expansion coefficients of Nafion. Both these studies were conducted before the use of Nafion as a fuel cell membrane was discovered and therefore represent a broad evaluation of Nafion as a material rather than one targeted at the fuel cell relevant properties. In particular they examined the effect substituting different ions in for the hydrogens on the sulfonic acid groups has on each of the properties. Small strain stress relaxation tests were performed at temperatures from 30^oC to 185^oC for both dry and hydrated acid form Nafion. Time-temperature superposition was shown to hold for dry Nafion but fail for hydrated Nafion (Figures 5, 6). Dynamic mechanical analysis (DMA) revealed three transition regions: the α peak at -100^oC which moves minimally with hydration; the β peak at 0^oC which moves to lower temperatures with hydration and merges with the α peak at a ratio of 2.5 water to sulfuric acid molecules; and the γ peak which occurs at 110^oC, the same temperature as the glass transition of pure backbone material(Figure 7). The γ peak was assigned as the glass transition of Nafion due to its lack of change with hydration, coincidence with the pure PTFE peak, and greater $tan\delta$ peak value. Ion exchange resulted in a higher temperature β transition and a greater $tan\delta$ peak value with peak height inversely proportional to cation size (excluding hydrogen). The combination of the stress relaxation and DMA results was taken to indicate the presence of two significant mechanical mechanisms, backbone motion and cluster motion, with the cluster motion mechanism suppressed under dry conditions. Small angle x-ray scattering (SAXS) resulted in a single diffuse peak which was taken to support the concept of side chain clusters distributed

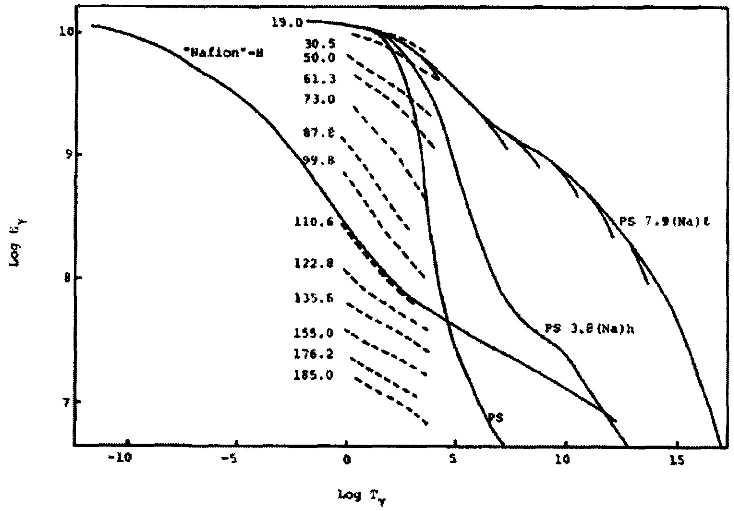

Figure 5: Original stress relaxation curves and master curve for Nafion-H as well as master curves for polystyrene (PS) and two styrene ionomers (PS3.8(Na)h and PS7.9(Na)l) with $T_{ref} = T_g$ from Yeo and Eisenberg (1977).

throughout Nafion(Yeo and Eisenberg (1977)).

Takamatsu and Eisenberg found that the thermal expansion behavior of extruded Nafion is anisotropic and dependent on thermal history for both the acid form as well as the Li, Na, K, and Cs salt forms. Below 80^oC the expansion coefficient is consistent between runs, but above 80^oC the curves diverge rapidly. Figure 8 shows the dimensional change of acid form Nafion as a function of annealing temperature. A linear expansion test was also conducted on a specimen that had been soaked in water for 24 hours (Figure 9). For the first run the linear expansion was much greater than dry specimen with the tangent coefficient of thermal expansion becoming negative around 100^oC, subsequent runs approach the behavior of the annealed specimen. While the form of Nafion that is being phased in today is the cast rather than extruded and is unlikely to show such anisotropic behavior, this expansion data shows the importance of material preparation and storage in determining its properties.

Morris and Sun (1993) measured density and thickness changes of Nafion 117 (extruded, $183\mu m$ thick) with water content. Density was determined by the hydrostatic weighing method. Thickness measurements were obtained by measuring multiple layers with a micrometer. The results are

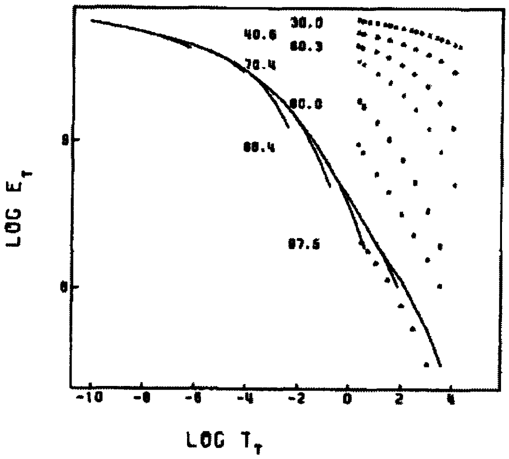

Figure 6: Original stress relaxation curves and master curve for hydrated Nafion-H ($0.5H_2O/SO_3H$) with $T_{ref} = T_g$ from Yeo and Eisenberg (1977).

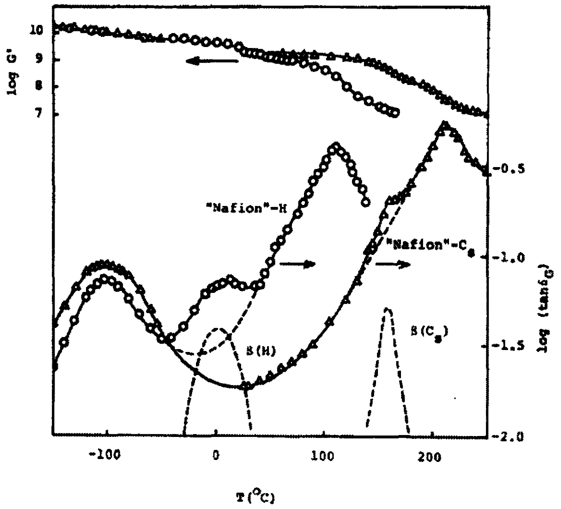

Figure 7: Mechanical loss tangent vs. temperature for Nafion-H and Nafion-CS at $1Hz$ from Yeo and Eisenberg (1977); dashed lines represent values for the β peak above background.

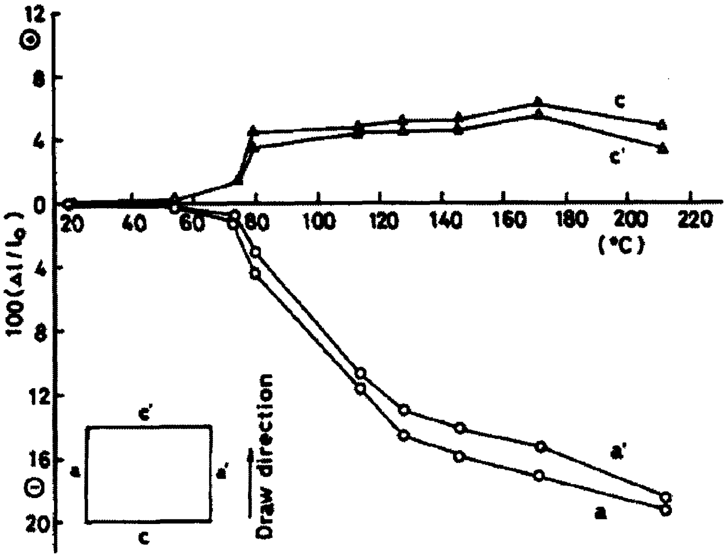

Figure 8: Dimensional changes of uniaxially oriented H-form membrane (EW=1100) in the a-c plane, as a function of annealing temperature from Takamatsu and Eisenberg (1979).

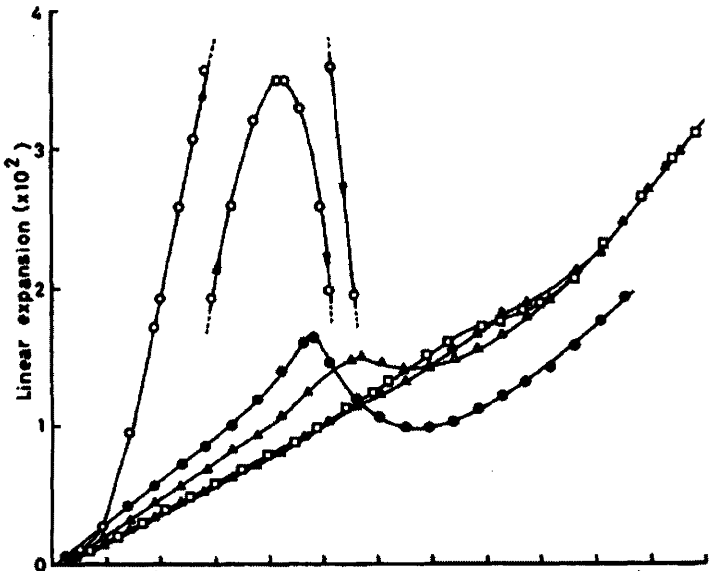

Figure 9: Linear expansion in the thickness direction vs. temperature for the Cs salt which was rolled, annealed at 200^oC, and then immersed in distilled water at room temperature for over 24 hours; (∘) first heating run; (∘) second heating run; (△) third heating run; (△) fourth heating run; (□) fifth heating run; from Takamatsu and Eisenberg (1979).

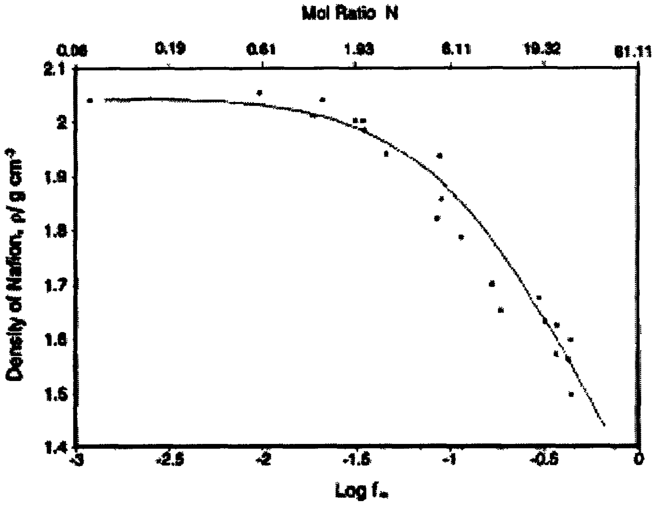

Figure 10: Density of Nafion 117 as a function of water content from Morris and Sun (1993).

shown in figures 10 and 11 below. The change in diameter is calculated from the density and thickness. Therefore the conclusion that Nafion swells more out-of-plane than in-plane is highly dependent on the accuracy of the thickness measurement. Given the low elastic modulus of Nafion and the likelihood that water would be pushed out during such a measurement, this swelling data is questionable.

The effects of temperature and humidity on the elastic modulus, yield stress, break stress, and elongation at break of Nafion 112(extruded, $50.8\mu m$ thick) were systematically studied by Tang, Karlsson et. al. (2006). Uniaxial tensile tests were conducted within an environmental chamber that allowed for control of both temperature and relative humidity. The specimens were fixed in the machine at zero stress and strain at ambient conditions, the temperature and then relative humidity were each raised to their target values, the grips were readjusted to a zero stress condition to accommodate the expansion, and the specimen was extended at a constant rate. The swelling was calculated from the change in the grip distance required for a zero stress condition. The elastic modulus and yield stress were found to decrease with increasing temperature and humidity with the elastic modulus and yield stress decreasing by 80% and 60% respectively from 25^oC and $30\%RH$ to 85^oC and $90\%RH$. Increasing temperature was also shown to lead to lower break stress and higher break strain, but no trend was seen in the break point with changes in humidity. The hygro-

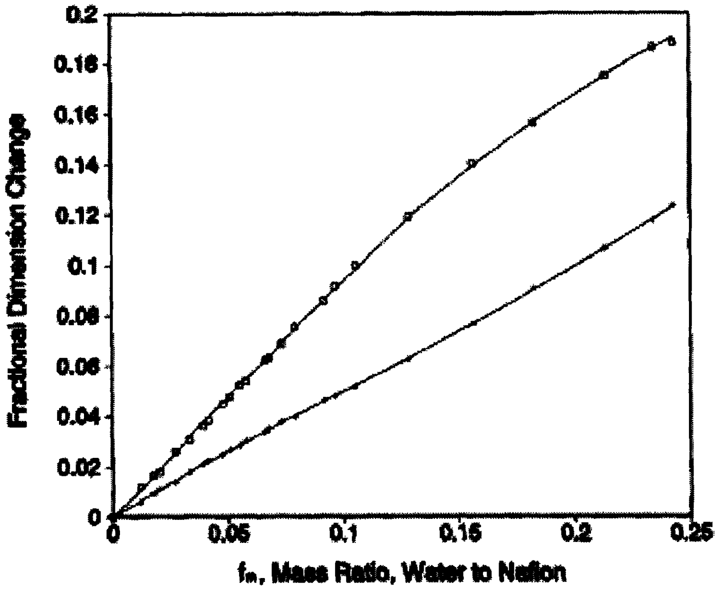

Figure 11: Fractional dimension changes of Nafion 117 as a function of water content: (□) thickness; (+) diameter from Morris and Sun (1993).

swelling was found to be highly non-linear in relative humidity with the tangent swelling coefficient increasing with increasing relative humidity and greater swelling occurring at higher temperatures for a given relative humidity. The dimensional change from 25^oC and $30\%RH$ to 85^oC and $90\%RH$ was around 12%.

Satterfield et. al. (2006) performed uniaxial tensile, creep, and swelling pressure tests (in which the pressure is evaluated in an environmental cell with a fixed strain condition) on extruded and recast Nafion 115 (extruded, $127\mu m$ thick). The test specimens were evaluated with respect to density and length before and after hydration. It was found that at 23^oC the extruded and recast Nafion increased in length by 10% and 12% respectively while fully hydrated whereas at 80^oC the corresponding length changes were 20% and 24%. This indicates the significant dependence of swelling on temperature. The tensile tests revealed a significant decrease in the elastic modulus with increasing temperature and water content as well as a slight decrease in the strain hardening slope with increasing temperature and no observable change in the strain hardening slope with water content. Typical creep curves for extruded Nafion at 23^oC under dry and fully hydrated conditions are shown in figure 12. While the rate of creep slows down significantly with time, the

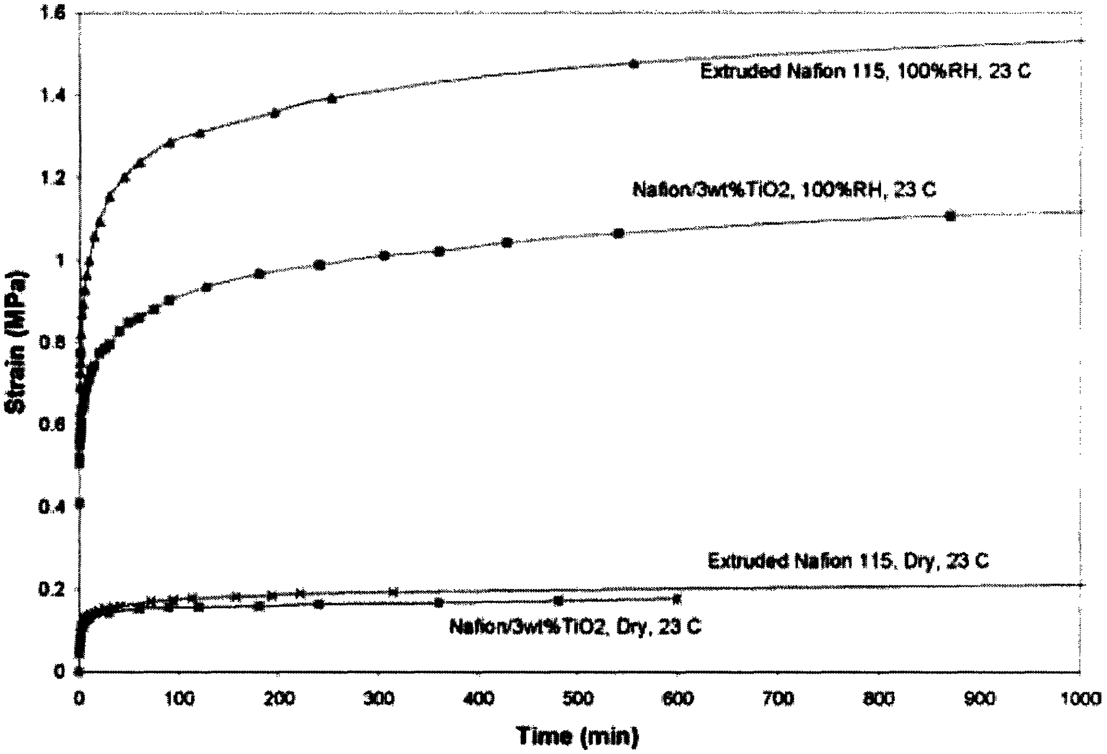

Figure 12: Creep data for Nafion 115 and Nafion/3 wt % titania 115 at 23^oC for both $0\%RH$ (dry) and $100\%RH$ with an applied engineering stress of $7.5MPa$ from Satterfield et. al. (2006).

strain does not approach a constant value. This is a key indicator that the network entanglements slip at a finite rate. The swelling pressure was evaluated in an environmental cell with a fixed strain condition; in each test the temperature was increased prior to the injection of water into the cell. The force increases only minimally with the temperature increase from 30^oC to 90^oC but increases almost 20% with water injection in roughly 30 minutes, the force then gradually decreases at a decreasing rate reaching a value 7% below the maximum force after roughly 40 hours. Similar to the creep behavior, the force never reaches a steady value.

Liu, Kyriakides et. al. (2006) examined rate effects of the mechanical behavior of Nafion 117 at ambient conditions (ca. 23^oC and 40% relative humidity). Uniaxial tensile tests were conducted at nominal strain rates from $4.167 \times 10^{-4}s^{-1}$ to $0.0117s^{-1}$. Increasing strain rate had minimal effect on the elastic modulus and ultimate stress and strain, but resulted in a significant increase in the yield stress and decrease in the yield strain. The results are summarized in table 1. Stress

Strain Rate $(\min^{-1})$	Initial Modulus (MPa)	Yield Stress (MPa)	Yield Strain (%)	Ultimate Strength (MPa)	Elongation at Break (%)
0.7	270 ± 4	12.6 ± 0.2	6.6 ± 0.8	36.5 ± 2.4	251 ± 14
0.3	253 ± 7	11.7 ± 0.1	7.5 ± 0.3	34.2 ± 2.9	235 ± 14
0.12	256 ± 18	10.9 ± 0.3	7.8 ± 0.9	25.9 ± 2.1	177 ± 27
0.07	263 ± 10	10.8 ± 0.2	8.3 ± 0.6	36.7 ± 2.3	262 ± 16
0.025	250 ± 5	9.8 ± 0.4	9.4 ± 0.5	31.8 ± 2.3	250 ± 9

[a] The samples were prepared with the same treatments and tested in the same environment. The water concentrations were 5.3 ± 1.5%.

Table 1: Summary of selected tensile properties of Nafion 117-H films at different strain rates under ambient conditions from Liu et. al. (March 2006).

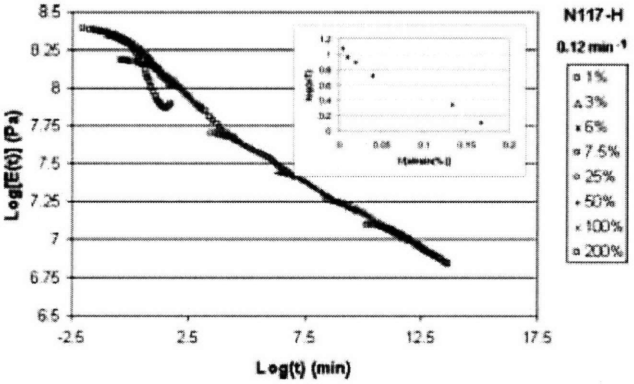

Figure 13: Shifted logarithm plot of $E(t)$ versus $t(min)$ for N117-H films and plot of log a_T versus 1/strain(%) from Liu et. al. (March 2006).

relaxation tests were conducted at an initial strain rate of $2.0 \times 10^{-4} s^{-1}$ and nominal hold strains from 0.01 to 2. The master curve for the relaxation modulus is shown in figure 13. The master curve is somewhat reasonable above the yield strain, but the data exhibits large deviations from the master curve at low strains. This is similar to the results of Yeo and Eisenberg (1977) in which master curves from the DMA data could not be constructed because of the multiple deformation mechanisms. The authors suggested that non-linear viscoelasticity would be useful for analyzing the data but did not pursue that analysis.

Liu, Hickner et. al (Oct 2006) conducted stress relaxation tests on extruded Nafion 117 under both dry and water soaked conditions. Stress relaxation was found to occur faster in air than

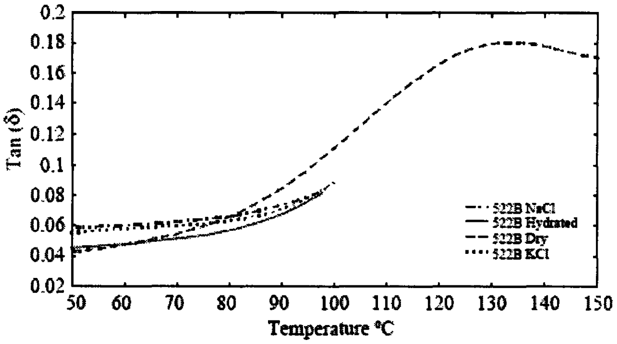

Figure 14: Comparison of tan(δ) of the MEA 522B in dry, hydrated, and exchanged with KCL and NaCL from Kundu et. al. (2005).

in water. The was rationalized by attributing the relaxation in air to relatively fast backbone motions, while the stress in the hydrated membrane during the initial expansion is greatly reduced due to the plasticizing effect of water resulting in a smaller overall stress decay and therefore mathematically longer relaxation times. An additional cause of the longer mathematical relaxation time for hydrated membranes might be the slower motion associated with poroelastic behavior.

Kundu et. al. (2005) conducted isothermal uniaxial tension tests and dynamic mechanical analysis (DMA) at temperatures from 40^oC to 140^oC for dry specimens and to 100^oC for wet specimens on Nafion 117 and Nafion 112 as well as four different MEA. The ion exchanged form of these materials with Ni^+, Mg^{2+}, Cu^{2+}, Na^+, and K^+ was characterized in addition to the acidic form. Young's modulus and yield stress were found to increase with increasing radius of the cluster ion. This increase was attributed to the increased ionic interaction of the clusters resulting in reduced chain mobility. Dynamic mechanical analysis revealed much lower values of storage and loss moduli for the hydrated relative to dry membranes at the lower end of the temperature range with a much smaller reduction in those values as the temperature is increased. The location of the peak of the glass transition could not be compared since it occurs over the boiling point of water, but the onset was seen to occur at a lower temperature. This data for one of the MEA's is shown in figure 14.

2.2 Experimental Methods

2.2.1 Materials

Nafion is classified by its processing, equivalent weight, and thickness. The processing can be either extruded or dispersion cast; the types of Nafion with only an "N" preceding the identifying number are extruded, those preceded by "NRE" are dispersion cast. The equivalent weight (EW) is defined as the weight of Nafion in grams per mole of sulfonic acid groups; all the forms of Nafion discussed in this thesis have an EW of 1100. In the old Nafion nomenclature this was represented by the first two identifying numbers, however this has been abandoned in the naming of new Nafion membranes over the last few years. The final number identifies the thickness of the film in mils. For example, "N117" is extruded Nafion of EW 1100 that is $7mils$ ($17.8\mu m$) thick.

Commercial NRE212 films ($2mils$, dispersion cast, Dupont, Ion Power Inc) were used for the experimental characterization of Nafion. The films were stored in a desiccator cabinet upon removal from the initial packaging to minimize variability in data from aging and humidity effects. The material was tested either as-received or after a chemical pre-treatment commonly used by scientists to purify and acidify the membrane in experimental fuel cell systems.

The pre-treatment entailed soaking the membrane in hydrogen peroxide (H_2O_2) for 1 hour at $85°C$ to remove any impurities, soaking in deionized water for 1 hour $85°C$ to rinse the hydrogen peroxide, soaking in sulfuric acid (H_2SO_4) for 1 hour at $85°C$ to fully acidify the membrane, and finally soaking in deionized water at $80°C$ for an additional hour to rinse away the excess sulfuric acid. The pre-treated specimens were dried in a desiccator cabinet for at least 24 hours prior to testing.

2.2.2 Dynamic Mechanical Analysis

Dynamic mechanical analysis (DMA) testing was performed on a TA Instruments Q800 Dynamic mechanical analyzer. Specimens were cut $5mm$ wide with a set of parallel blades. The specimens were positioned in the grips to have a gauge length of approximately $10mm$ and were tested at a frequency of $1Hz$ and amplitude of $15\mu m$. The temperature was increased from $-10°C$ to $170°C$ at a heating rate of $3°C$ per minute.

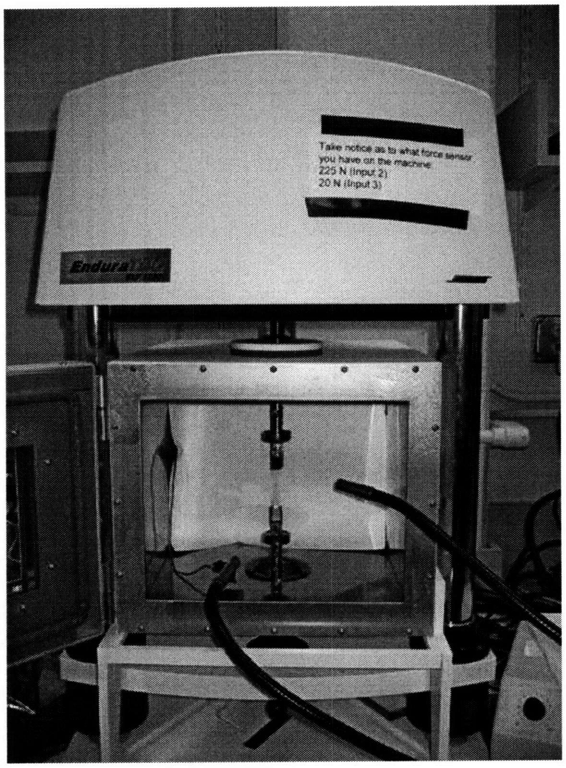

Figure 15: Picture of the EnduraTEC Electroforce 3200 (ELF) used for all tensile testing with the temperature chamber installed.

2.2.3 Tensile Testing

Uniaxial tension tests were conducted at constant engineering strain rates from $0.001/s$ to $0.1/s$, at temperatures from $25°C$ to $100°C$, and at various water contents. The material was cut into tensile specimens using a dogbone shaped die with gauge length of either $9.54mm$ or $4.0mm$ and gauge width $3.14mm$. The nominal thickness is $54\mu m$. The thickness of each specimen was determined from the average of three measurements taken along the gauge length with a Mitutoyo micrometer. All tensile tests were conducted on an EnduraTEC Electroforce 3200 (ELF) (Figure 15). Cyclic and stress relaxation tests were conducted in displacement control mode while creep tests were conducted in force control mode. The maximum strain achieved in each trial is limited by the $12mm$ stroke length of the ELF.

A Qimagine Retiga 1300 video extensometer was used to monitor strain in order to eliminate the effect of slipping at the grips, machine compliance, and deformation outside the gage length

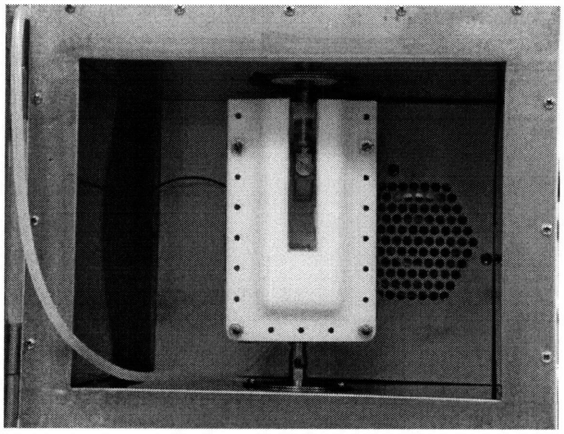

Figure 16: Picture of the custom built water chamber built for use with the EnduraTEC Electroforce 3200 (ELF) used for all tensile testing.

from the stress-strain data. The specimen was marked by Sharpie with black dots and illuminated by a Fiber-lite PL900. Two points within the gauge length of the specimen aligned along the axis of applied tension were tracked using the vic2d software from Correlated Solutions Inc designed for that purpose. The relative change in the distance between the points was used to determine strain.

Temperatures above room temperature were achieved using a Sun Systems ET1 Environmental Chamber attached to the ELF. The specimens were allowed to equilibrate at temperature for 30 minutes prior to testing. The same video extensometer setup was used for the thermal tests except that an ultraviolet lamp was used instead of the visible spectrum Fiber-lite to illuminate the specimen through the chamber door.

For the hydration tests, the specimens were first imaged when dry and then submerged in deionized water for at least 30 minutes. The tension test was conducted as soon as possible after removal of the specimen from water. Hydration tests were also conducted in a custom built water chamber fitted to the ELF(Figure 16). The specimen was mounted in the grips and imaged. Water was then added to completely submerge the specimen. The top grip was raised until the specimen reached a zero-strain position at which point the tension test was conducted. For both types of hydration tests the change in the length and width of the specimen between the relaxed dry and wet states, as determined by the video extensometer, was used to calculate the amount of swelling as well as to estimate the swollen cross sectional area.

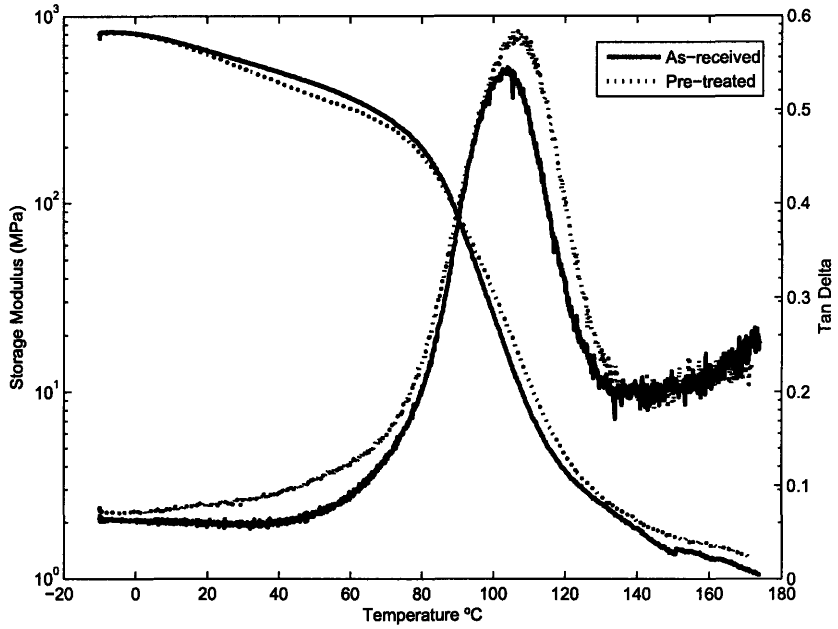

Figure 17: DMA data for as-received and pre-treated NRE212.

Hydration tests at elevated temperatures were conducted by heating the water prior to putting it into the water chamber.

2.3 Experimental Results and Discussion

2.3.1 Dynamic Mechanical Analysis

The DMA testing showed a broad transition temperature regime. While the peak of the tan delta curve occurs at $105°C$, the storage modulus begins to drop noticeably as early as $20°C$ with a steep drop beginning at approximately $70°C$. There is no observable shift in the viscoelastic DMA storage or loss curves or glass transition due to the chemical pretreatment.

2.3.2 Tensile Testing

Images taken by the video extensometer during a uniaxial tension test at a strain rate of $.01/s$ are shown in figure 18. This behavior is qualitatively the same as that observed in all tensile tests. The deformation is uniform throughout the test with no necking occurring.

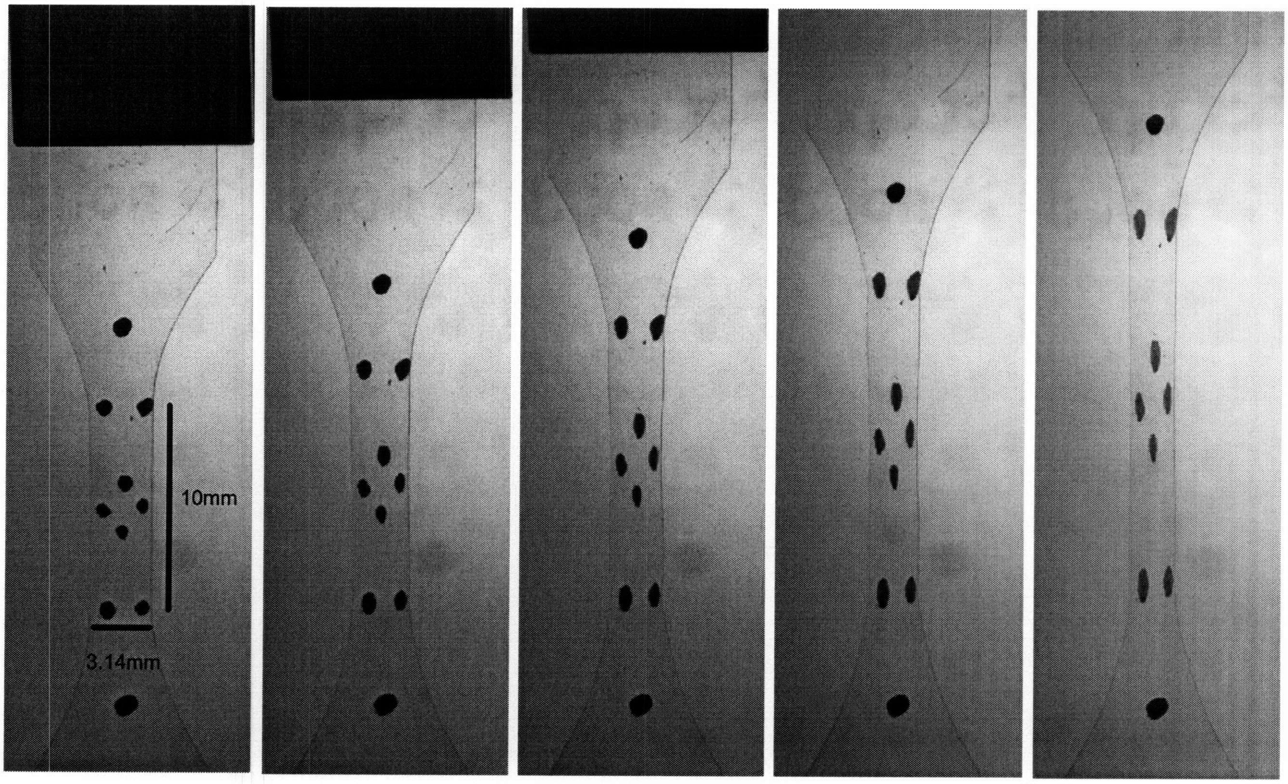

Figure 18: NRE212 true stress-true strain behavior in uniaxial tension at 25°C and .01/s as observed by the video extensometer.

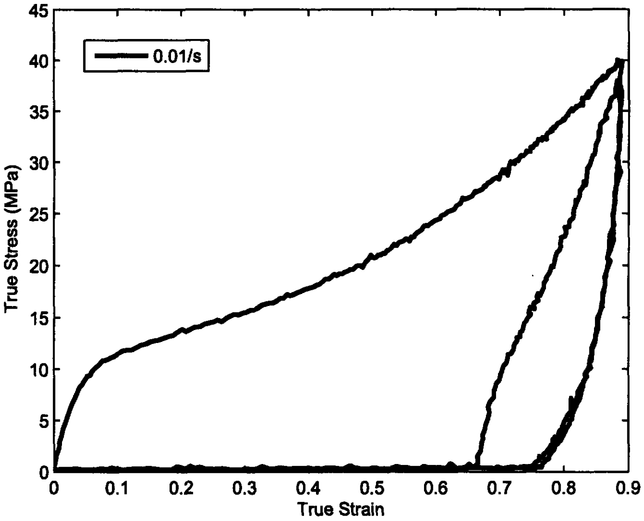

Figure 19: True stress-true strain behavior in uniaxial tension at 25°C and $.01/s$.

The force-displacement data as taken from the ELF and video extensometer respectively was reduced to true stress and true strain assuming isotropic incompressible behavior where true stress is defined as force over the current cross-sectional area and true strain is defined as the natural log of the current length over the initial length. Nafion uniaxial tensile behavior, as shown in figure 19, can be divided into three basic regions. There is a small linear-elastic region at strains less than about 0.02. The curve then exhibits a gradual rollover as yielding occurs up to a strain of 0.1. Strain hardening becomes the dominant feature as the stress-strain relation curves increasingly upward at large strains. The unloading is slightly non-linear for this test conducted to a maximum strain of 0.89, only a small amount of strain is recovered when the specimen is unloaded to zero stress (0.76 versus 0.89). Further recovery occurs during the time when the grip displacement is still changing (the grips are programmed to return to their original position and then to separate giving the reloading, the thin flexible specimen elastically buckles during the unloading), and the specimen begins its reload from a strain of 0.66. The reload curve shows an elbow at a stress slightly below that of yield on the initial loading and does not quite reach the stress of the initial loading curve when it reaches the maximum strain for the second time.

The data was shown to be repeatable given the same environmental conditions. Figure 20 shows

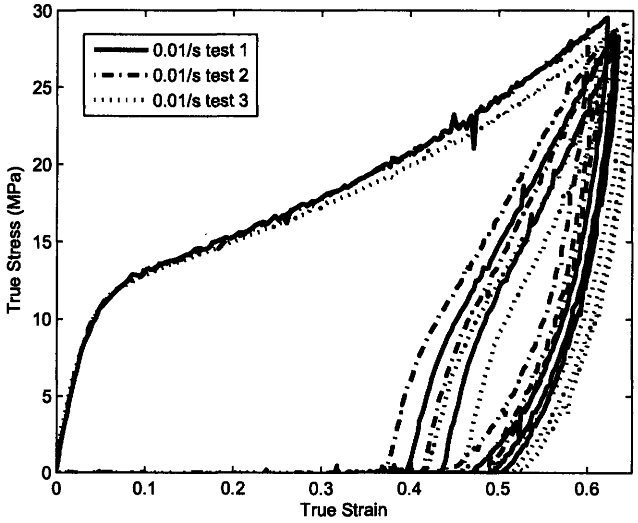

Figure 20: True stress-true strain behavior in uniaxial tension was found to be repeatable for the same testing and environmental conditions.

three uniaxial tension tests conducted at the same strain rate and temperature. The linear-elastic and yielding regions overlay perfectly and there are only slight deviations at larger strains and during unloading and subsequent reloading.

In order to check for transverse isotropy, tensile tests were conducted on specimens cut from the NRE212 sheet at mutually perpendicular orientations. While a slight difference in stress-strain behavior is seen between the two orientations it is well within the experimental error; the unloading and reloading behavior is also nearly identical (Figure 21).

A moderate strain rate dependence is evident from tests conducted at room temperature at engineering strain rates of $0.001/s$, $0.01/s$, and $0.1/s$ (Figure 22). There is a significant increase in the yield stress and a slight decrease in the yield strain and increase in the elastic modulus as the strain rate is increased, there is no change in the post-yield tangent modulus, and the material recovers to the same strain at zero stress for all three strain rates. This is in agreement with the findings of Liu et. al. (March 2006). Figure 23 shows the roughly linear dependence of the yield stress on the logarithmic strain rate.

The viscoplastic behavior is also evident when Nafion is subjected to a cyclic loading profile. The stress-strain behavior shown in figure 24 comes from uniaxially loading and unloading a speci-

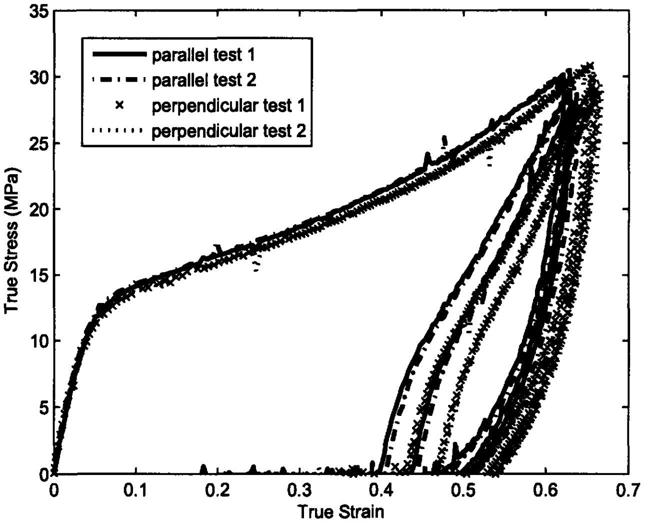

Figure 21: True stress-true strain behavior of specimens cut from film at perpendicular orientations in uniaxial tension at 25°C and .01/s.

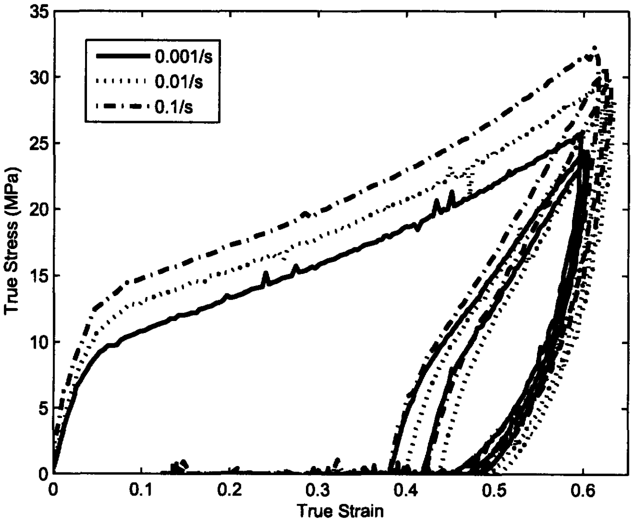

Figure 22: True stress-true strain behavior in uniaxial tension at multiple strain rates at 25°C.

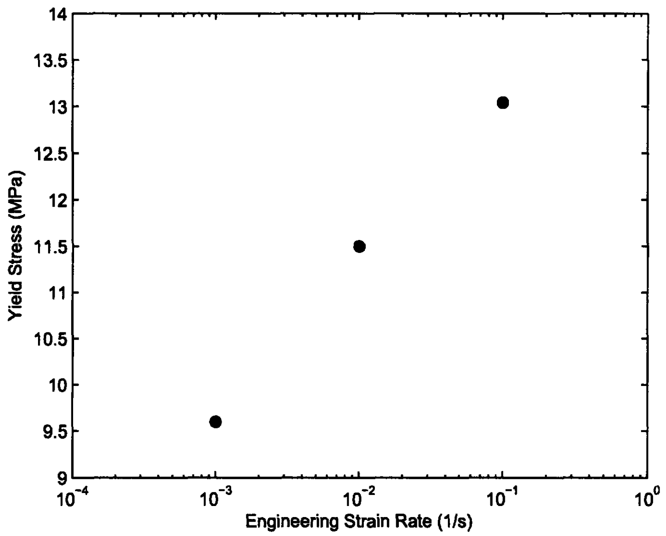

Figure 23: Yield stress as a function of engineering strain rate at 25°C.

men to increasing strain values. At each strain past yield the material recovers more than would be predicted by a linear elastic unloading. For example, after an imposed strain of 0.44, the material recovers to a residual strain of 0.29 whereas linear elastic unloading would have given a residual strain of 0.37. The unloading behavior is characterized by a relatively stiff linear region (roughly 90% of the initial elastic modulus) which becomes increasingly more compliant as unloading progresses. Further recovery occurs during the time when the grip displacement is still being changed but the specimen is buckled ($54s$ for the 0.44 max strain cycle), hence reloading curves begin at a smaller strain than the strain immediately after unloading (0.23 versus 0.29). The reloading is highly nonlinear prior to rejoining the initial curve. Reloading is characterized by an initially stiff linear region ($\sim$ 66% of the initial modulus) which rolls over to a more compliant behavior; the rollover begins at a stress level substantially lower than the initial yield stress ($\sim$ 68%). The unloading and reloading curves mirror each other about the imaginary line that can be drawn from the peak stress on the reloading curve and midpoint between the unload and reload strain at zero stress (from $strain = 0.44$, $stress = 20.4$ to $strain = 0.25$, $stress = 0$ for the 0.44 max strain cycle). This general behavior holds for cycles to maximum strains around and below 0.4, but at higher strains the cyclic unloading and reloading undergo a qualitative (and of course continues to

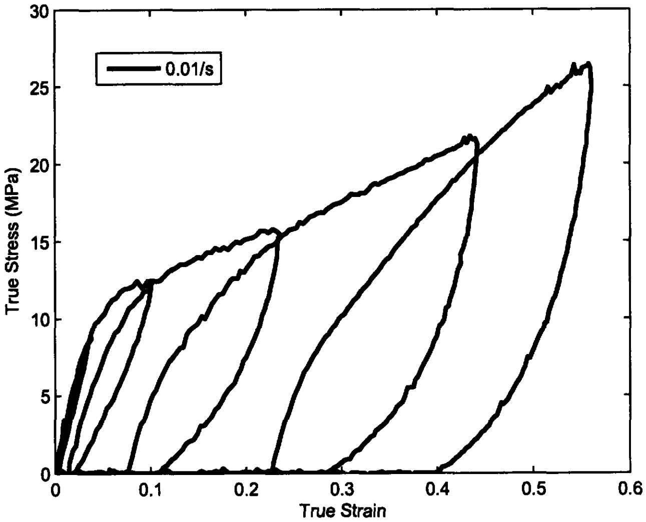

Figure 24: True stress-true strain behavior under uniaxial tensile cyclic loading conditions at $0.01/s$ and $25°C$.

undergo a quantitative) change. The unloading and reloading start to lose their symmetry; the unload is still gradual although the strain recovery is a smaller percentage of the total strain, and the reload develops a clearer and lower yield point at which the slope of the curve changes noticeably.

Time dependent behavior is also evident from stress-relaxation tests in which the strain is held constant while the stress is measured (Figures 25-27). In figure 25 the specimen is strained at two different strain rates to the same strain level and held there for 300 seconds. It can be seen that while the specimen tested at the higher strain rate has an initially stiffer stress response, it relaxes to the same stress level as that to which the specimen pulled at the slower rate relaxes.

Figures 26 and 27 show how the stress-relaxation behavior varies with applied strains from the linear viscoelastic region of behavior to just past yield to well into the post-yield region. The characteristic time constant decreases significantly through yield but then holds constant where twice the time constant is calculated from the time the stress takes to decay 67% of the difference between the stress when the load is first applied and the stress after 2 minutes (approximated as the steady state stress). The ratio of the steady-state stress to the peak stress decreases quickly through yield and then continues to decrease more slowly showing the transition from a linear viscoelastic only relaxation behavior to relaxation due to both linear viscoelastic processes and

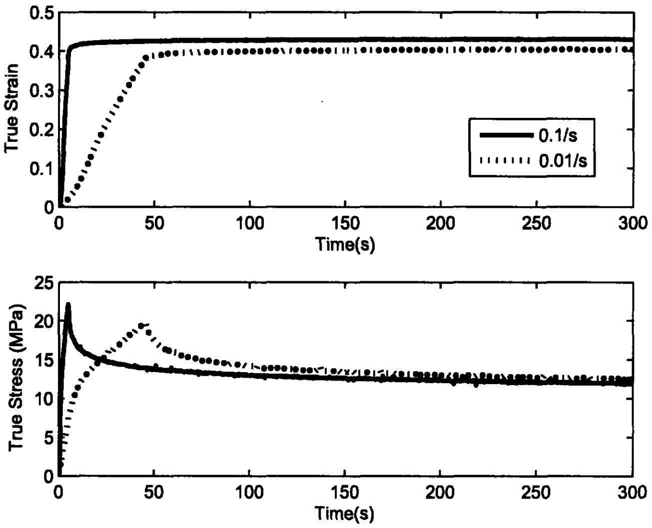

Figure 25: True strain-time and true stress-time for uniaxial tensile stress relaxation tests at initial loading rates of $0.1/s$ and $0.01/s$ at $25°C$.

non-linear viscoplastic processes. The difference between the peak stress and steady-state stress increases with increasing strain as a result of the increasing peak strain and the lesser contribution of the decrease in the steady-state to peak ratio.

Another method for understanding time dependent behavior is creep testing for which the stress is held constant while the strain is measured. The strain and stress are shown through time for three different enforced stress conditions in figure 28 below. Creep occurs for all three strain levels and does not approach a steady state value. This is in agreement with the results of Satterfield et. al. (2006).

The mechanical behavior has a strong nonlinear dependence on temperature. Tests conducted at an engineering strain rate of $0.01/s$ at temperatures from $25°C$ to $100°C$ are shown in figure 29 below. When the temperature is increased there is a decrease in the initial elastic response and the yield stress, an increase in the yield strain, and the yield behavior tends more towards a roll over rather than a clear yield point. This is the same trend as found by Tang et. al. (2006) in their study on Nafion 112 and Satterfield et. al. (2006) in their study on Nafion 115. This change in behavior is most evident in the change in yield stress with temperature as shown in figure 30. Aside from the change in elastic modulus and yield stress already referred to, there are no apparent

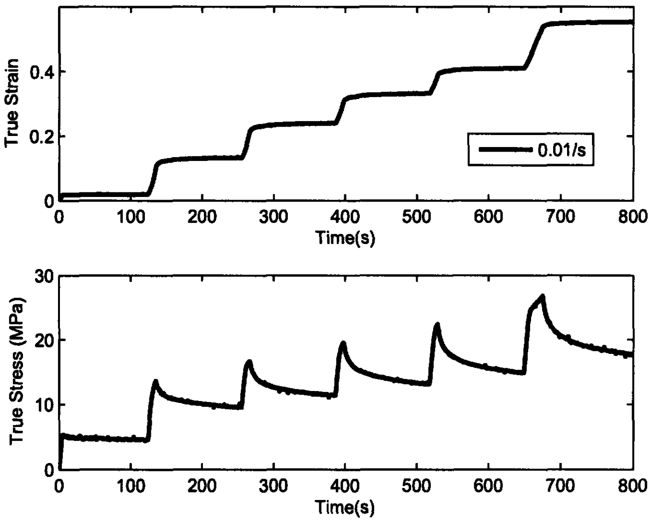

Figure 26: True strain-time and true stress-time for uniaxial tensile stress relaxation tests at increasing strain levels for loading rates of $0.01/s$ at $25°C$.

changes in either the cyclic or the stress relaxation behavior(Figures 31 - 33).

There is a strong dependence of the mechanical behavior on hydration (Figure 34). The elastic modulus and yield stress decrease rapidly as the water content is increased from that present at ambient humidity and temperature but then the values plateau so that the difference in behavior among specimens with significant water content is minimal regardless of the specific water content. The swelling percentage indicated is calculated from the change in the distance between dots marked on the specimen from the dry state to the hydrated state at the start of the test; this change is found using video extensometer images and is calculated as the average of at least five pairs of dots.

The two methods for hydrating the specimen are compared in figure 35: in the first method, referred to as "in air", the specimen is soaked in water for 45 minutes and then placed in the ELF and tested; in the second method, referred to as "water immersed", the specimen is placed in the ELF inside a water bath and tested while still in the water. It can be seen that for short time periods the hydration methods give equivalent hydration as evidenced by equivalent mechanical behavior. The method in which the specimen is continually immersed in water during testing is more reliable over longer testing periods, however it does not allow for testing at different hydration levels. The drying of the non-immersed specimen is evident in the second cycle in which the specimen reaches

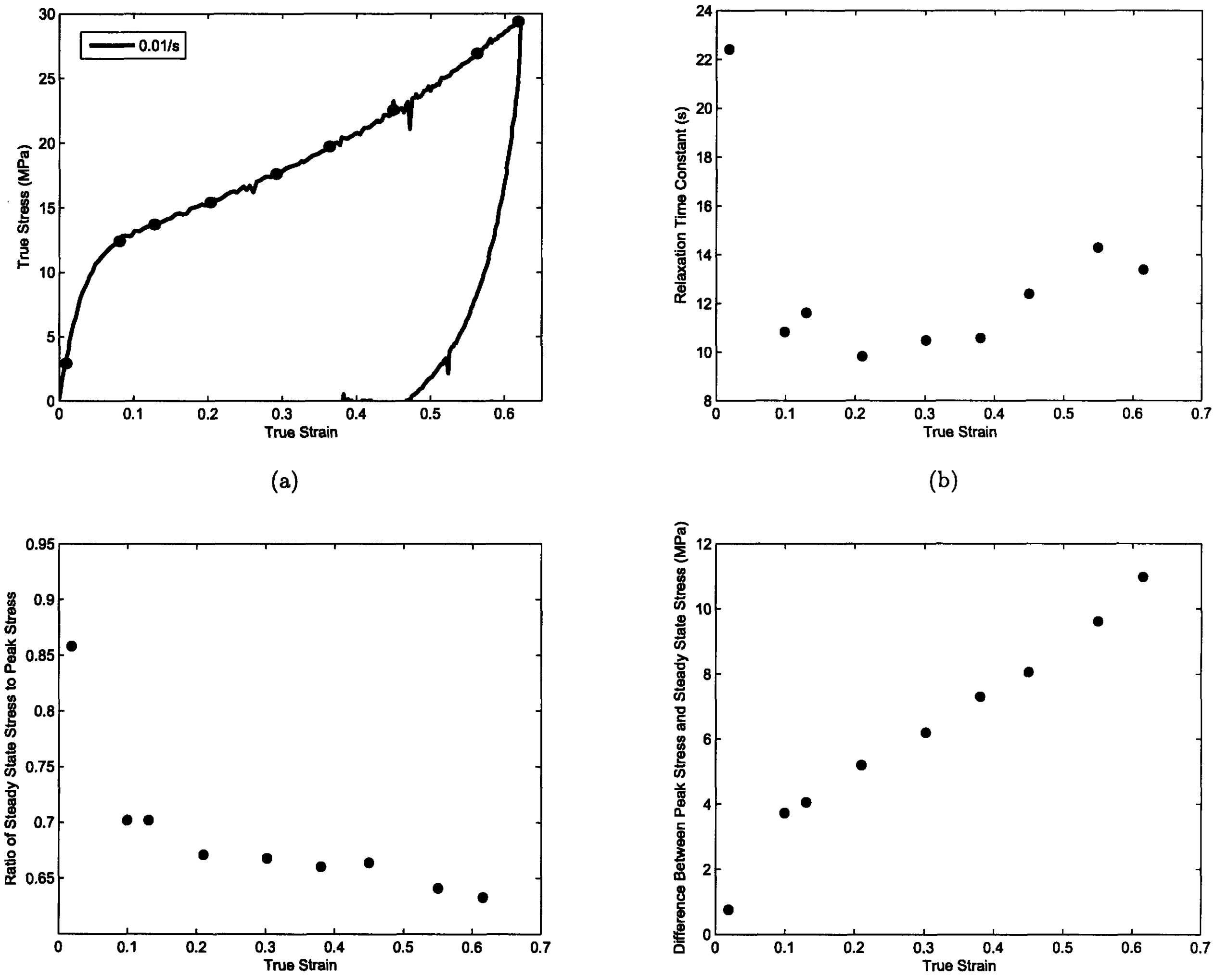

(a) (b)

(c) (d)

Figure 27: Stress relaxation data reduction: (a)Indicates where on the stress-strain curve the stress-relaxation tests were conducted; (b)Relaxation time constants associated with stress-relaxation at a range of strain levels; (c)Ratio of the steady state stress to the peak stress at a range of strain levels; (d)Difference between the peak stress and the steady state stress a range of strain levels.

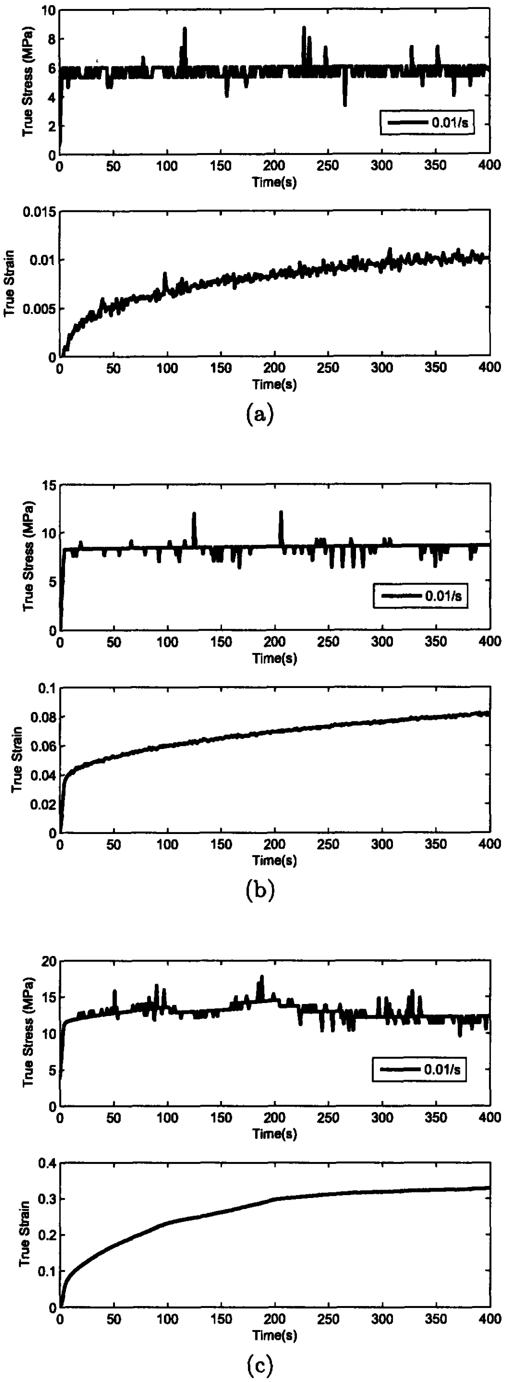

Figure 28: True stress-time and true strain-time for uniaxial tensile creep tests performed at different stress levels: (a)$6MPa$, (b)$9MPa$, and (c)$12MPa$.

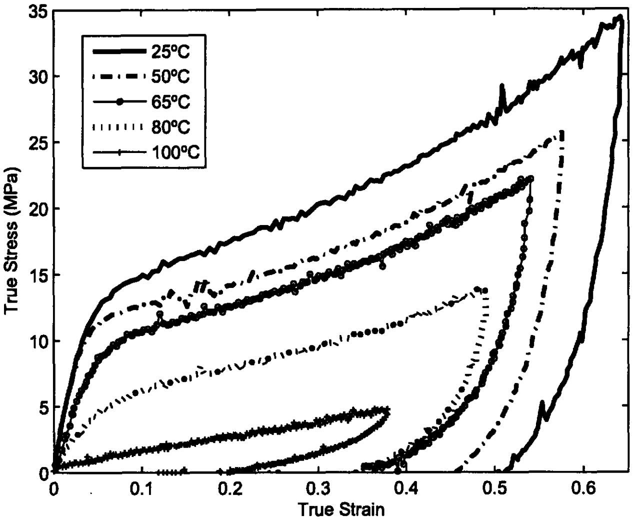

Figure 29: True stress-true strain behavior in uniaxial tension at multiple temperatures at $0.01/s$.

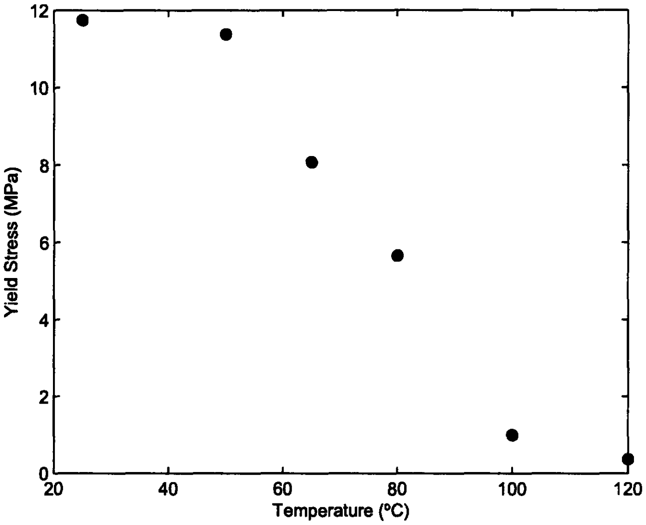

Figure 30: Yield stress as a function of temperature at 0.01/s.

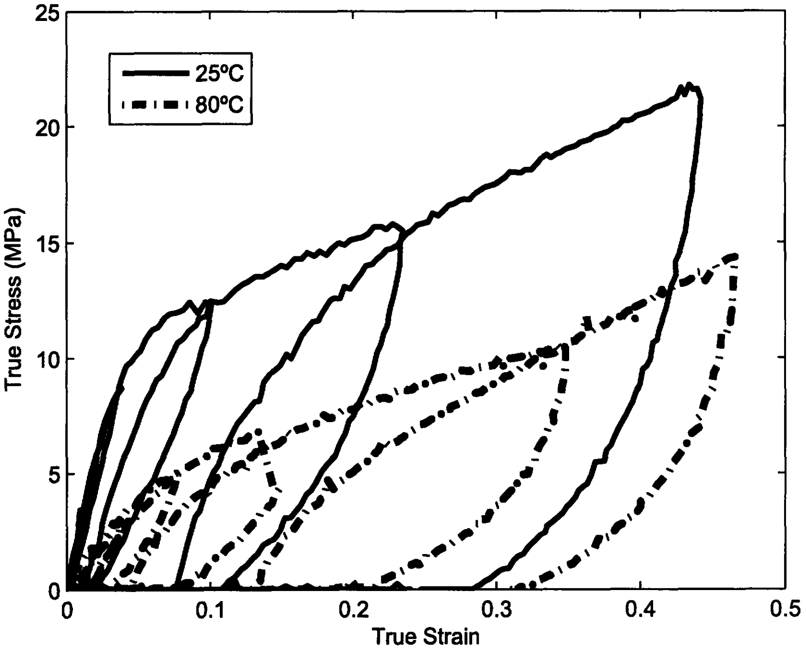

Figure 31: True stress-true strain behavior in uniaxial tension at .01/s at 25°C and 80°C.

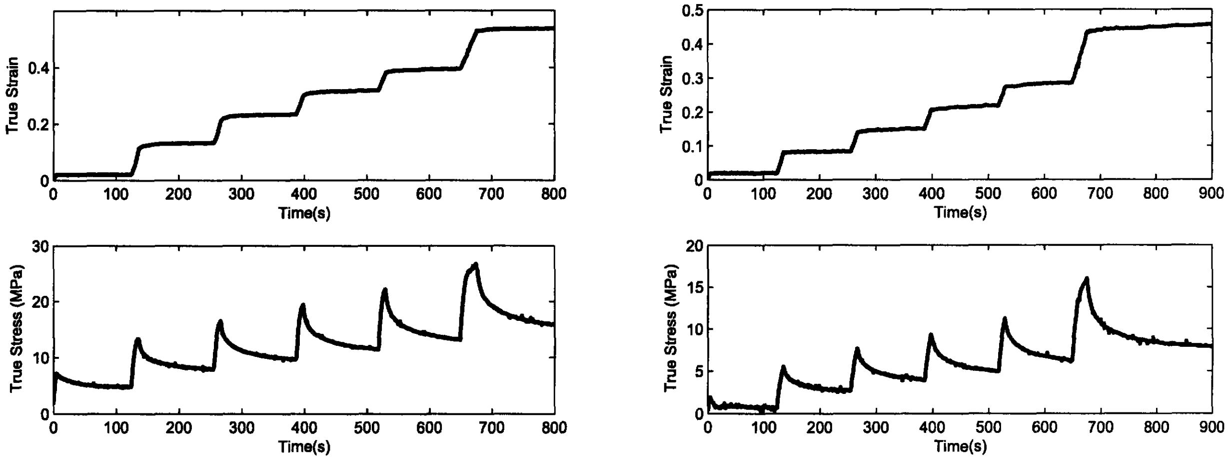

(a)

(b)

Figure 32: True strain-time and true stress-time for uniaxial tensile stress relaxation tests at increasing strain levels for loading rates of 0.01/s at (a) 50°C and (b) 80°C.

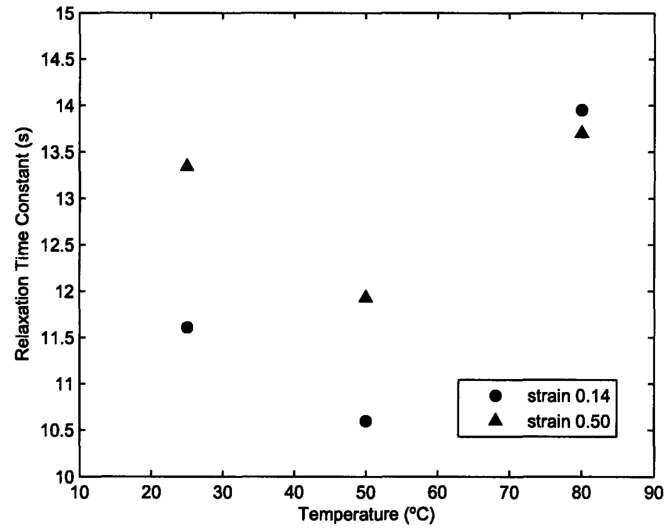

Figure 33: Stress relaxation time constant as a function of temperature for two strain levels.

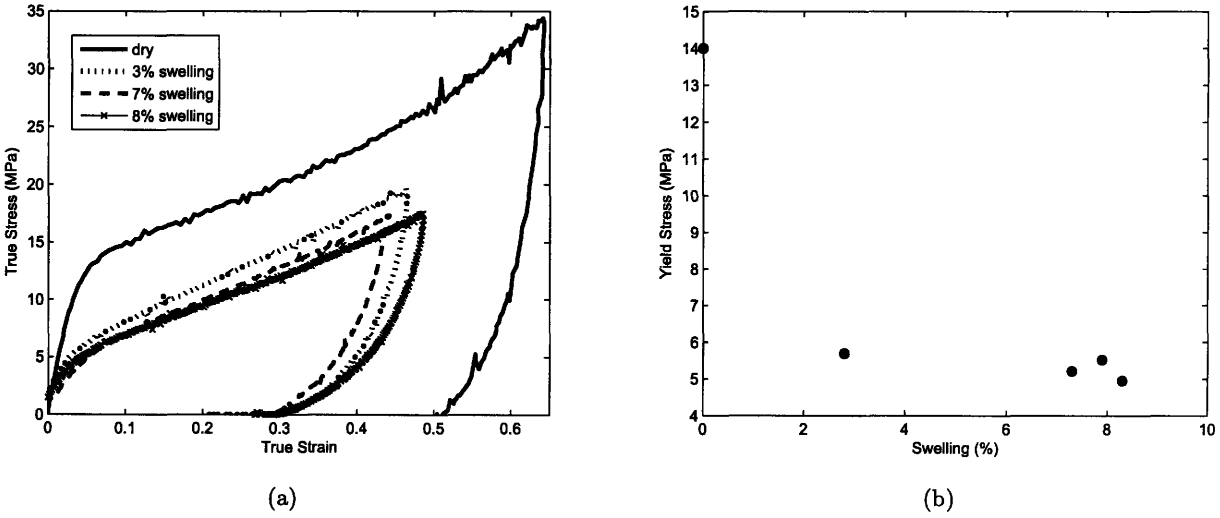

(a)

(b)

Figure 34: Effect of hydration on uniaxial tensile behavior at $0.01/s$ and $25°C$ (a)True stress-true strain curve at multiple hydration levels (b)Yield stress as a function of swelling percentage.

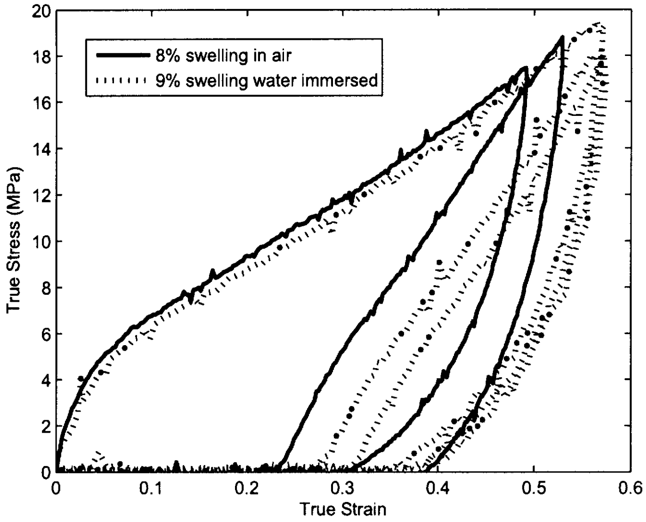

Figure 35: True stress-true strain behavior in uniaxial tension at $0.01/s$ and $25°C$ for two hydration methods: one in which the specimen is soaked in water for $30mins$ and then tested in air, and one in which the specimen is tested while immersed in water.

a greater strain level than during the first cycle even though the ends of the specimens are being brought to the same maximum positions.

The cyclic and stress relaxation behavior of Nafion under hydrated conditions is qualitatively the same as that under dry conditions, however for a given strain there is more recovery upon unloading, particularly for the cycles which go to larger maximum strains (Figure 36). For instance, from a maximum strain of 0.56 the dry specimen recovers to a strain of only 0.4 at zero stress for unloading while the water immersed specimen recovers to a strain of 0.31. The hydrated specimen also loses its unload/reload symmetry at a lower strain as it is already clearly visible in the cycle to a maximum strain of 0.4.

The stress relaxation behavior of a specimen immersed in water during testing is shown in figure 37 (a). While the trends are the same for water immersed specimens as for dry specimens, the time constants for stress relaxation are longer for hydrated specimens (Figure 37 (b)). This is likely a poroelastic effect, particularly since the same trend is not seen with changes in temperature.

Figure 38 shows a typical stress-strain curve resulting from heating (to $80°C$) and hydrating Nafion at the same time relative to the dry $80°C$ stress-strain curve, and the wet room temperature

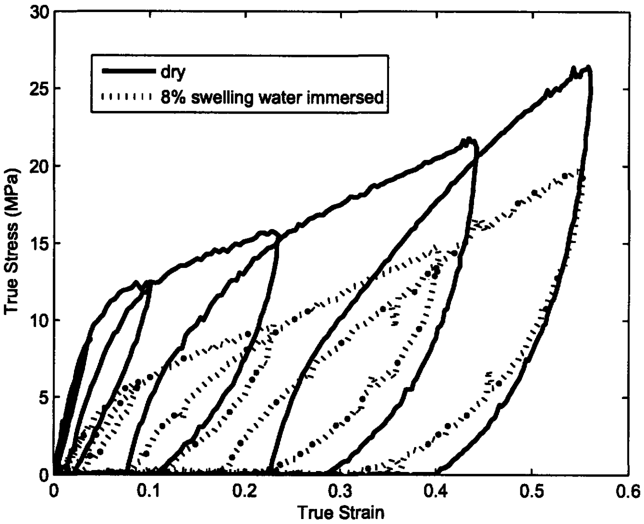

Figure 36: True stress-true strain behavior under uniaxial tensile cyclic loading conditions at $0.01/s$ and $25°C$ while dry and while water immersed.

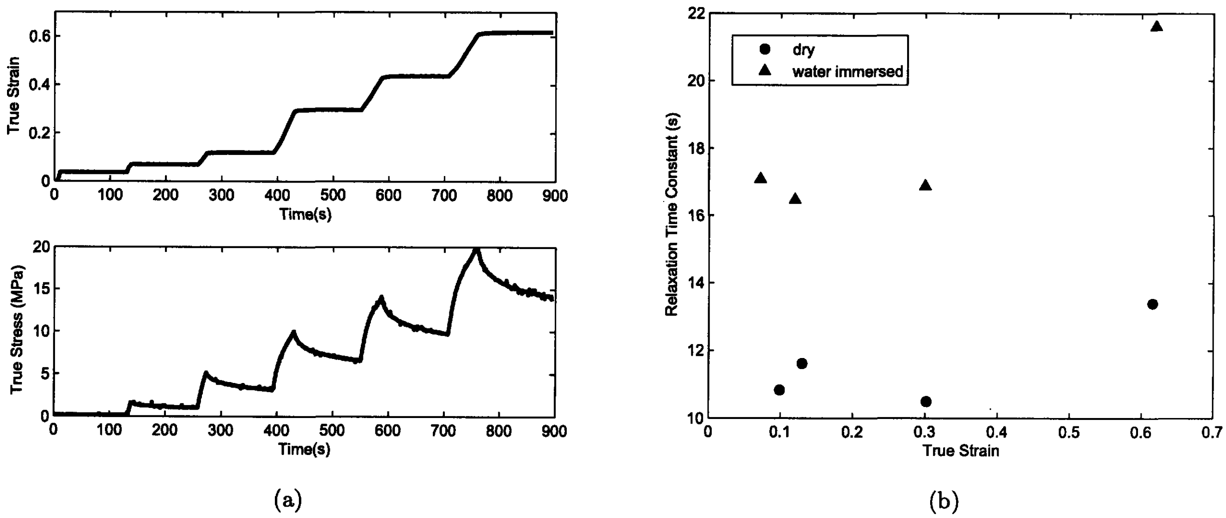

(a) (b)

Figure 37: Effect of hydration on stress relaxation behavior at $25°C$ and $0.01/s$ while loading. (a)Stress relaxation-time at increasing strains for water immersed Nafion. (b)Stress relaxation time constant as a function of strain for dry and water immersed Nafion.

stress-strain curve. The reduction in elastic modulus and yield stress relative to that at room temperature and relative humidity is greater for the combined hydrated and heated specimen than for a specimen subjected to either one alone. The effect of hydrating the specimen over a range of temperatures can be seen in figure 39 in which the yield stress is given at different temperatures for both the dry and hydrated specimens. It should be noted that the specimens at higher temperatures expand more than those at room temperature (figure 39) where the $80°C$ microstructure is well into the middle of the leathery transition to rubbery behavior (and hence in an expanded free volume state) which allows more water molecules to be absorbed into the membrane. It is therefore possible that part of the decrease in yield stress results from the increase in water content rather than being a direct effect of the temperature increase. However, this seems unlikely since in the room temperature hydration tests conducted via method one, the yield stress dependence on water content seems to be highly non-linear and plateau around a water content that results in 7% swelling. The overall yield stress reduction factors can be calculated for each of heating a dry specimen, fully hydrating a room temperature specimen, and fully hydrating a heated specimen, where reduction factor for a set of conditions is defined as the yield stress over the reference yield stress taken at room temperature and humidity. If the product of the first two reduction factors matches the third then this would indicate that the thermal and hydration dependence of the mechanical properties can be modeled as uncoupled within the tested temperature range. These factors were calculated for $50°C$ and $80°C$; for $50°C$ the product of the thermal and hydration reduction factor is 0.31 while the combined thermo-hydration reduction factor is 0.29; for $80°C$ the product of the thermal and hydration reduction factor is 0.15 while the combined thermo-hydration reduction factor is 0.07. This calculation implicitly assumes that the change in modulus due to increased water content is minimal since the water content is in the plateau region. Based on these numbers it is clear that an uncoupled assumption can be used at $50°C$; however such an assumption should be used with caution as the temperature approaches $80°C$ and even higher temperatures, as this is getting into the heart of the glass transition regime during which the material is undergoing significant structural rearrangements.

A limited set of tensile tests was also performed on chemically pre-treated Nafion. In each case

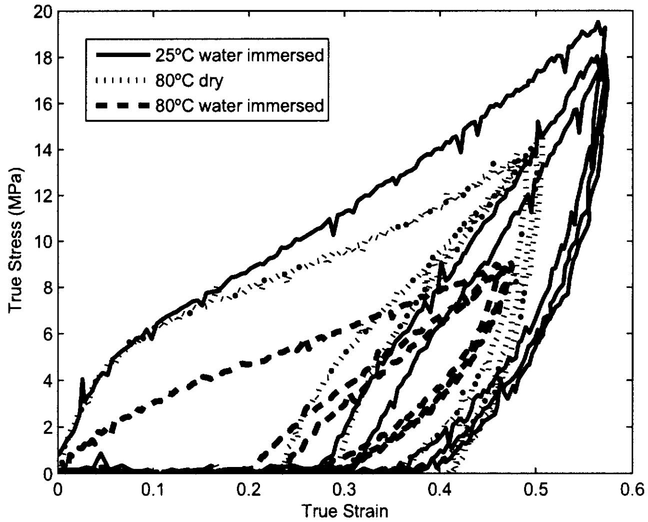

Figure 38: Effect of heating and hydration on uniaxial tensile true stress-true strain behavior.

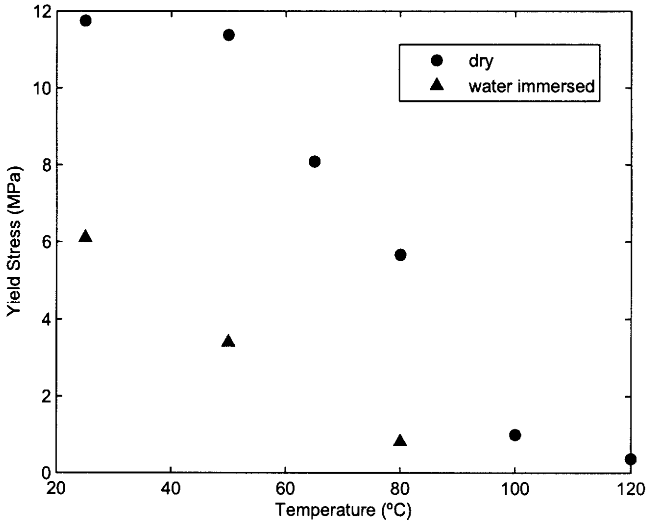

Figure 39: Yield stress as a function of temperature for both dry and water immersed Nafion at 0.01/s.

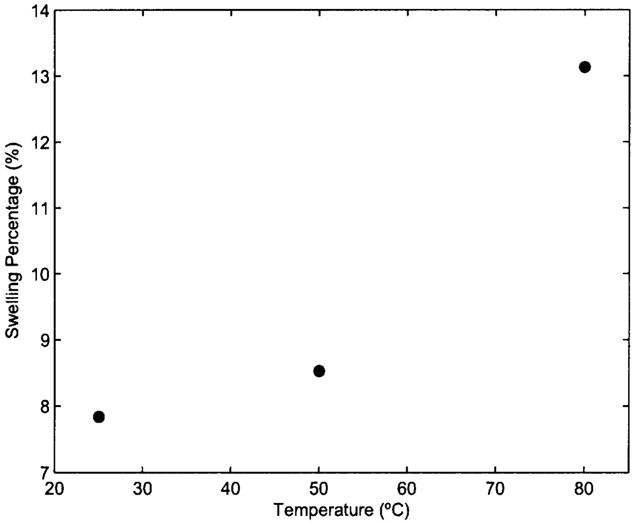

Figure 40: Swelling percentage as a function of temperature for water immersed Nafion.

the pre-treated material was shown to exhibit a slightly lower stress than that of the as-received material for the corresponding strain but to have qualitatively the same behavior as the as-received material. Figures 41 through 44 shows the true stress-true strain curves of the pre-treated material versus the as-received under a range of environmental conditions.

In order to investigate which part of the pre-treatment causes the decrease in mechanical properties, uniaxial tensile tests were conducted on partially pre-treated specimens (Figure 45). The five pre-treating options were 1) none (i.e. as-received), 2) soaking in water at room temperature for 1 hour, 3)heating in air to $80°C$ 3)soaking in water at $80°C$ for 1 hour (i.e. the fourth step of the pre-treating process only) 4)soaking in hydrogen peroxide (H_2O_2) at $85°C$ and then soaking in water at $85°C$ for 1 hour (i.e. the first two steps of the pre-treating process only) 5)the full pre-treatment including soaking the membrane in hydrogen peroxide (H_2O_2) for 1 hour at $85°C$, soaking in deionized water for 1 hour at $85°C$, soaking in sulfuric acid (H_2SO_4) for 1 hour at $85°C$, and finally soaking in deionized water at $80°C$. After each of the pre-treating methods the membrane was allowed to fully dry and cool. It is clear from these results that it is the simultaneous heating and hydrating the membrane that reduces its mechanical properties.

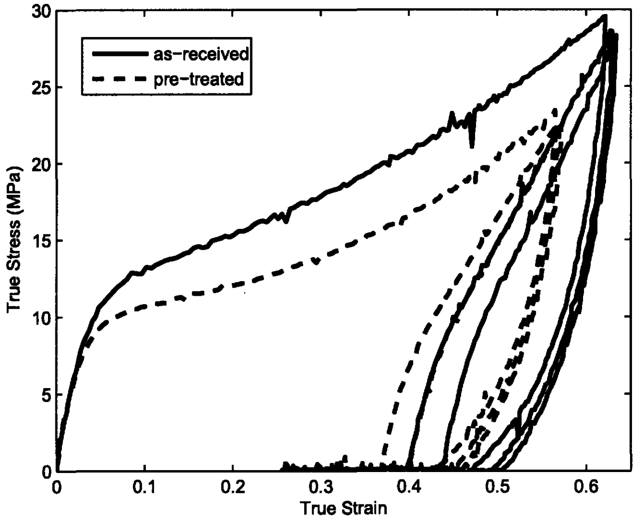

Figure 41: Comparison of pre-treated and as-received material true stress-true strain behavior in uniaxial tension at $0.01/s$ and $25°C$.

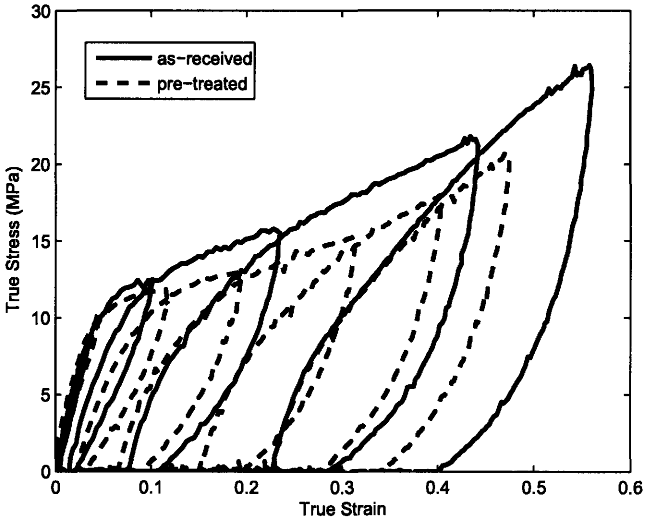

Figure 42: Comparison of pre-treated and as-received material true stress-true strain behavior under uniaxial tensile cyclic loading conditions at $0.01/s$ and $25°C$.

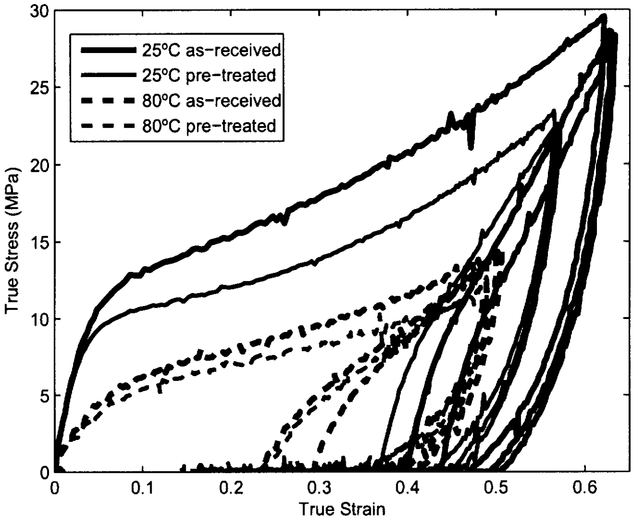

Figure 43: Comparison of pre-treated and as-received material true stress-true strain behavior in uniaxial tension at $0.01/s$ and $25°C$ and $80°C$.

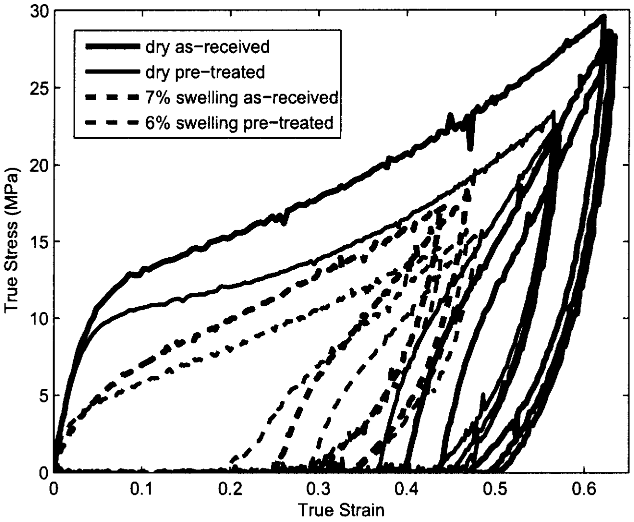

Figure 44: Comparison of pre-treated and as-received material true stress-true strain behavior in uniaxial tension at $0.01/s$ and $25°C$ while dry and hydrated.

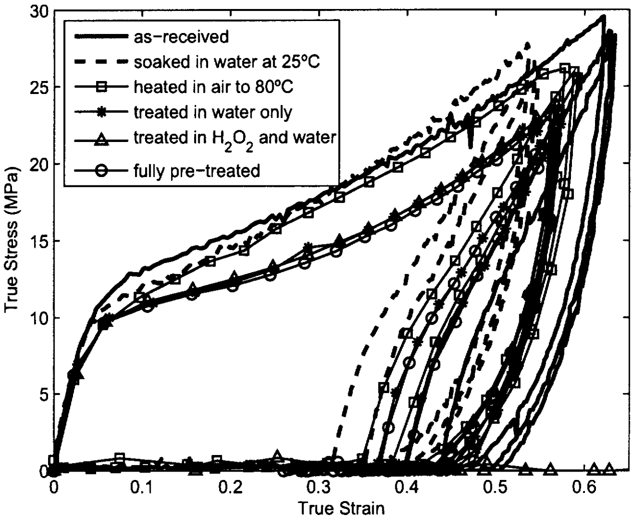

Figure 45: Comparison of pre-treated, partially pre-treated, and as-received material true stress-true strain behavior in uniaxial tension at $0.01/s$ and $25°C$.

2.4 Summary of Mechanical Experimental Results

The key features of the mechanical behavior observed through uniaxial tensile tests are:

1) Initial linear elastic behavior, roll over yield, and strain hardening (Figure 46).

2) Strain rate dependence of yield stress (Figure 47).

3) Nonlinear elastic unloading and reloading (Figure 48).

4) Transition of stress relaxation behavior from the linear viscoelastic region through the yield and post-yield regions (Figure 49).

5) Dependence of all of the above on temperature and hydration (Figure 50).

In the following chapter xray diffraction techniques will be used to try to understand the microstructure, how it evolves with strain, and how this evolution might be connected to the stress response of the material summarized above.

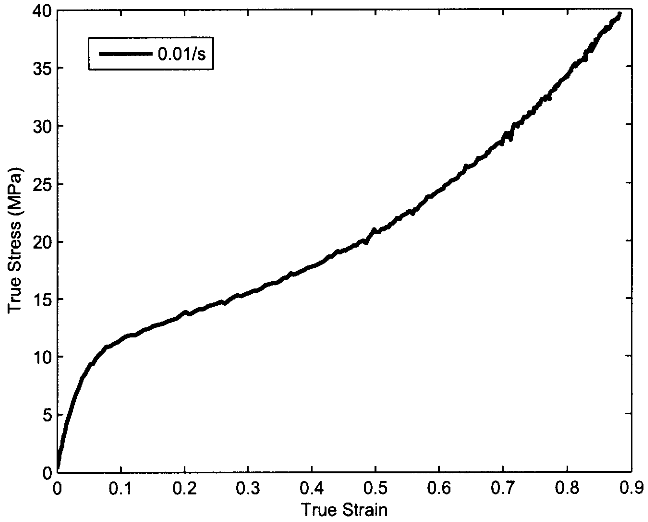

Figure 46: True stress-true strain behavior in uniaxial tension at 25°C and .01/s showing an initial linear-elastic behavior followed by a rollover type yielding and strain hardening.

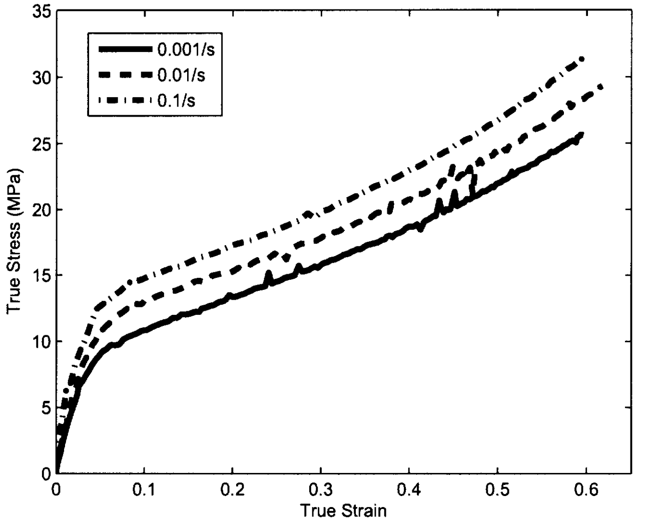

Figure 47: True stress-true strain behavior in uniaxial tension at multiple strain rates at 25°C showing the strain rate dependence of the yield stress.

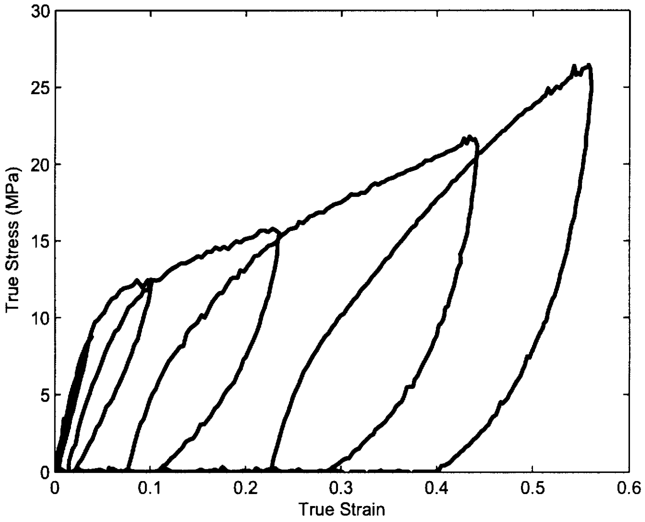

Figure 48: True stress-true strain behavior under uniaxial tensile cyclic loading conditions at $0.01/s$ and $25°C$ exhibiting nonlinear elastic unloading and reloading.

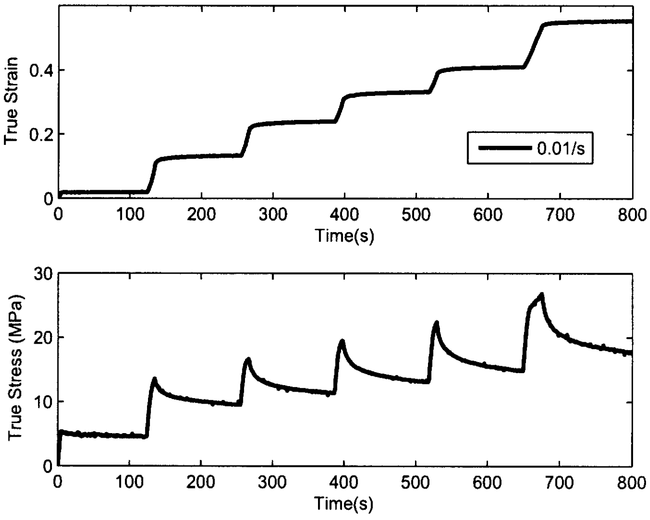

Figure 49: True strain-time and true stress-time for uniaxial tensile stress relaxation tests at increasing strain levels for loading rates of $0.01/s$ at $25°C$. The magnitude of the stress relaxation increases rapidly through yield and moderately as the strain is increased further.

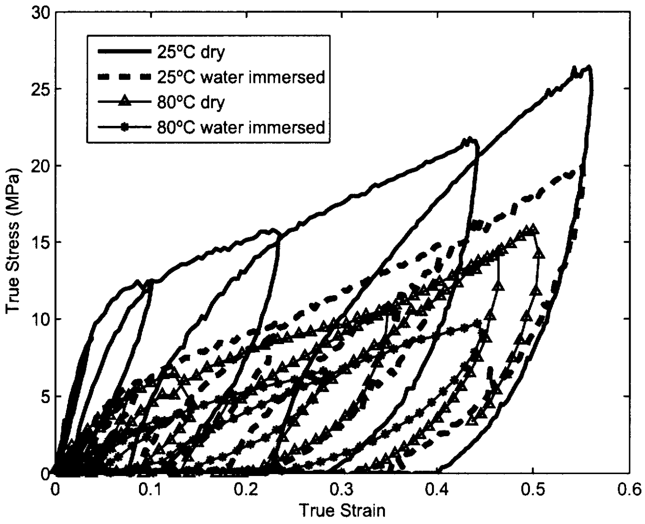

Figure 50: The effects of temperature and hydration on the true stress-true strain behavior under uniaxial tensile cyclic loading conditions at $0.01/s$.

3 Small angle and wide angle xray scattering

3.1 Background

Small angle x-ray scattering (SAXS) and wide angle x-ray scattering (WAXS) are techniques frequently used to make arguments about the structure of Nafion. While many research groups have used SAXS and WAXS as well as other methods to decipher the structure of Nafion, there is as of yet no consensus.

SAXS is an x-ray scattering technique used to look at features roughly 5 to $25nm$ by recording diffraction angles around $0.01\mathring{A}^{-1}$ to $0.2\mathring{A}^{-1}$. WAXS records larger diffraction angles, on the order of $0.5\mathring{A}^{-1}$ to $5\mathring{A}^{-1}$, thereby allowing the examination of smaller features. Peaks in SAXS and WAXS patterns are a result of electron density differences that results from different structural features. When an xray is passed through a material it diffracts off the electrons orbiting around atoms in the material. Depending on the spacing of those atoms, the diffracted parts of the beam will interfere either constructively or destructively. The averaged effects of these constructive and destructive interferences throughout the beam path will result in a spectrum of intensities at different angles at the exit of the beam from the material. These spectrums are generally recorded as intensity versus q-value, where q is a measure of the exit angle with units of either inverse angstroms or inverse nanometers. Unlike with crystallography, SAXS and WAXS can be used to analyze materials that are only partially ordered. While there are not sharp spikes in the spectrum as there are in crystalline structures, there are clear peaks whose location, width, and relative magnitude can be used to infer the size, distribution, and orientation of different semi-ordered structures in a non-crystalline material.

There are typically three features observed in SAXS and WAXS spectrums of Nafion. The SAXS spectrum has a single peak at $0.1 - 0.2\mathring{A}^{-1}$ that is commonly referred to as either the ionomer or cluster peak and attributed to the aggregates of sulfonic acid side chains caused by the sidechain hydrophilicity and backbone hydrophobicity. In the WAXS spectrum there are two peaks: a lower angle peak at roughly a q-value of $1.2\mathring{A}^{-1}$ generally attributed to intermolecular backbone structure, and a higher angle peak around a q-value of $2.7\mathring{A}^{-1}$ which is sometimes observed.

Halim and Scherer conducted SAXS and WAXS analysis on extruded Nafion 117 as well as recast Nafion formed under dry and hydrated conditions. They found that dry-cured recast Nafion and Nafion 117 had the same SAXS peaks at slightly different magnitudes, but that the wet-cured recast Nafion has a significantly higher intensity cluster peak at a lower q-value. From the peak position they inferred that the ionic cluster size is the same in dry-cured and Nafion 117, and that both are smaller than the cluster size in wet-cured Nafion. From the greater peak intensity of the wet-cured Nafion, they concluded that the film contains more clusters. In the WAXS results which included angles from 3^o to 26.4^o, one asymmetric amorphous peak was observed. While the asymmetry was taken to suggest that a low degree of crystallinity was present in each type of film, the percentage and characteristic dimension could not be extracted due to the overwhelming amorphous contribution to the peak.

Elliot et. al. (2000) conducted SAXS tests on Nafion N115 in swollen and oriented states. They found that the ionomer peak moved to a lower angle and increased in intensity with swelling suggesting an increase in spacing between clusters and an increase in the size of individual clusters. They suggest that this increase in size is accounted for largely by the coalescing of multiple clusters into single clusters thereby accounting for the frequently observed discrepancy between the magnitude of the microscopic and macroscopic swelling on Nafion. This affirmed the conclusion reached by James et. al. (2000) using atomic force microscopy (AFM). In the dry state specimens were drawn to 50% strain in the direction parallel to and perpendicular to the direction of extrusion. In the former case the applied strain increases the arcing perpendicular to the extrusion direction, in the latter the intensity parallel to the extrusion increases but it does not result in a symmetric scatter profile (Figure 51).

Heijden et. al. (2004) examined Nafion N117 and N125 with SAXS and WAXS while they were subjected to uniaxial tension in order to establish a relationship between structural orientation and stretch as well as determine any stretch induced crystallinity changes. Five features were identified in the combined SAXS and WAXS results taken from q-values of $.001\AA^{-1}$ to $5\AA^{-1}$: a low angle upturn attributed to large scale electron inhomogeneities, a matrix knee characterized as the correlation distance between the crystalline parts along polymer aggregates, the SAXS

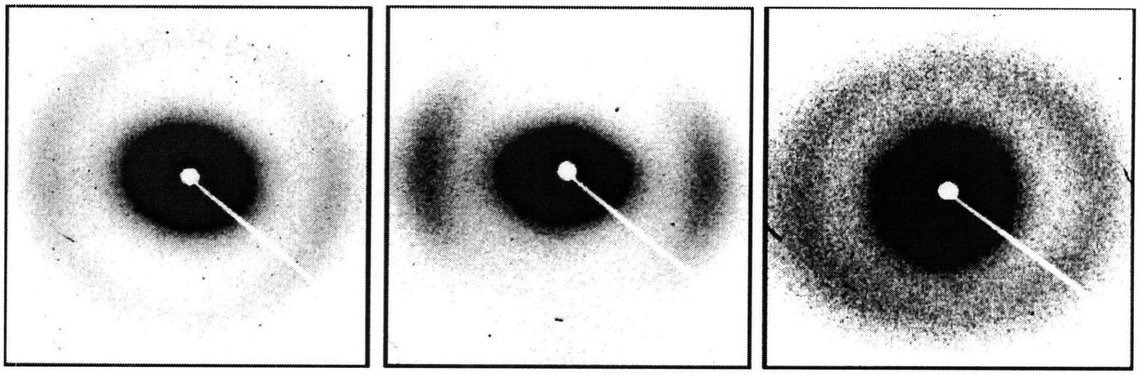
(a) (b) (c)

Figure 51: SAXS intensity map for Nafion N115 from Elliot et. al. (2006). (a) In the as-received state the scattering has arcing in the direction perpendicular to the extrusion direction. (b) When the specimen is strained parallel to the extrusion direction the arcing increases and the scattering peak becomes more elliptical. (c) When the specimen is strain perpendicular to the extrusion direction the intensity parallel to the extrusion direction increases but the scattering profile does not become symmetric.

and WAXS peaks similar to those observed by Halim et al., and an additional lower intensity WAXS peak at a higher q-value. Using different models for the possible crystalline structure of Nafion, they were able to deconvolute the amorphous and crystalline contributions to the lower WAXS peak, assign the third peak to a combined diffraction from intramolecular structures, and determine that the crystalline phase consists of PTFE (polytetrafluoroethylene) chains organized in orthorhombic unit cells. This assignment of the crystalline structure agrees with that of Porat et al. (1995) who determined the orthorhombic structure using transmission electron microscopy and transmission electron diffraction. No significant change in crystallinity with stretch was observed. Using the Hermans' orientation factor it was calculated that the ionomer peak, crystalline peak, and amorphous peak orient parallel to the draw direction, with the ionomer peak reaching its final oriented state at the lowest stretch. The intramolecular peak showed the opposite trend orienting perpendicular to the draw direction. From this study they propose a bundle-cluster model in which sections of the backbone are assumed to exist in small bundles that are randomly aligned with respect to other bundles; under small strains the bundles rotate so that they are aligned with each other; under large strain the bundles are all aligned and the aggregates are aligned within the bundles (Figure 52). Liu, Kyriakides et. al (2006) take this conceptual model further and

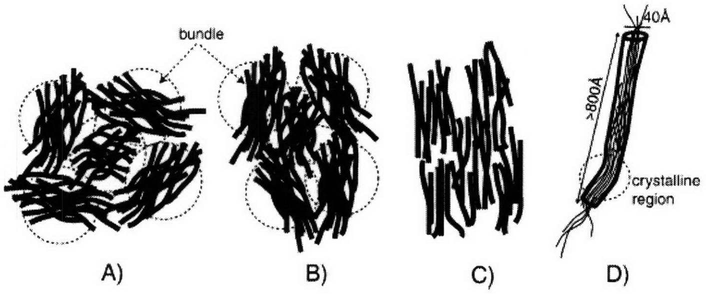

Figure 52: Sketch of the bundle-cluster model of Nafion under deformation from Heijden et. al. (2004) (A) Organization of bundles of aggregates made of more or less aligned and ordered polymeric chains surrounded with ionic groups and water molcules, (B) the bundles rotate to align with the direction of applied strain, (C) at high strains the aggregates are oriented within each bundle (D) a magnification of a single bundle.

suggest that the rate dependence of the mechanical behavior is related to the degree of alignment the bundles are able to achieve before they begin to disentangle (i.e. the orientation within each bundle at high strain).

Page et. al. (2006) conducted a study of the thermal relaxation of oriented Nafion. Ion exchanged Nafion (tetramethyl(TMA^+), tetrabutylammonium(TBA^+)) were uniaxially drawn to a stretch of 3 and then heated past the transition temperature of the clusters while SAXS was conducted. The results for TBA^+ (figure 53) reveal that in the highly oriented state the clusters have a fibrillar morphology as seen in the equatorial streaking at low q values. As the temperature is increased the ionomer peak gradually returns to its non-deformed state; it does not become fully isotropic again until it is at a temperature well over the backbone transition temperature. The specimen was then allowed to cool back to $100°C$ at which point it retained its isotropic configuration but had stronger scattering consistent with the reforming of distinct clusters.

While the above studies taken together start to give a fair picture of the structure of Nafion, none of them examine either the time or force dependency of the structural changes. This SAXS and WAXS study focuses on the orientation of the microstructural features with uniaxial extension and its relation to the stress supported by the membrane.

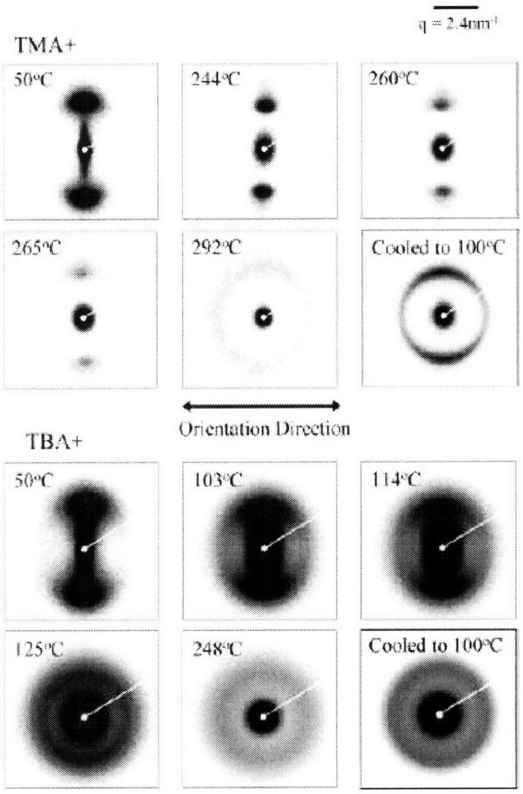

Figure 53: SAXS patterns of oriented TMA^+ and TBA^+ form Nafion during heating process and after cooling to $100°C$ from Page et. al. (2006).

3.2 Experimental Method

SAXS and WAXS experiments were conducted at the Argonne National Laboratory. Commercial NRE212 films (dispersion cast, Dupont, Ion Power Inc) were used for the experimental characterization of Nafion. The material was cut into tensile specimens using a dogbone shaped die with gauge length of $9.54mm$ and gauge width $3.14mm$. The nominal thickness is $54\mu m$. The thickness of each specimen was determined from the average of three measurements taken along the gauge length with a Mitutoyo micrometer. The films were stored in a desiccant chamber prior to testing.

Scattering data was collected while the specimen was subjected to uniaxial loading. All tests were conducted at a nominal strain rate of $0.005/s$. This value was chosen to allow collection of a sufficient scattering intensity without a significant change in strain. The same video extensometer as used for the tensile tests was used the track the local strain in the region through which the xray beam passed. The experimental configuration is shown along with a schematic representation in figure 54 a and b below. SAXS data was collected for q-values ranging from $0.007\AA^{-1}$ to $0.17\AA^{-1}$. WAXS data was collected for q-values ranging from $0.5\AA^{-1}$ to $4.5\AA^{-1}$.

3.3 Results and Discussion

The SAXS and WAXS intensity maps for an undeformed Nafion NRE212 film are shown in figure 55. The structure is initially isotropic in the imaged plane with three clear peaks; one in the SAXS and two in the WAXS. As discussed in the literature review above, the single SAXS peak is generally attributed to the ionic cluster phase formed by the sulfuric acid side chains. The two WAXS peaks are attributed to backbone structure. The lower angle WAXS peak (WAXSp1) is a combined amorphous and crystalline peak from intermolecular structures. The wider angle WAXS peak (WAXSp2) is a combination of intramolecular crystalline structures.

These peaks can be more easily analyzed by looking at an intensity profile. Three intensity profiles are derived from each intensity plot; equatorial (denoted as "Eq") is taken from the average of $+/-10^o$ from the axis perpendicular to the draw direction, meridional (denoted as "Me") is taken from the average of $+/-10^o$ from the axis parallel to the draw direction, and azimuthal (denoted as "Az") is taken from the average over all 360^o in the case of the SAXS data and 180^o

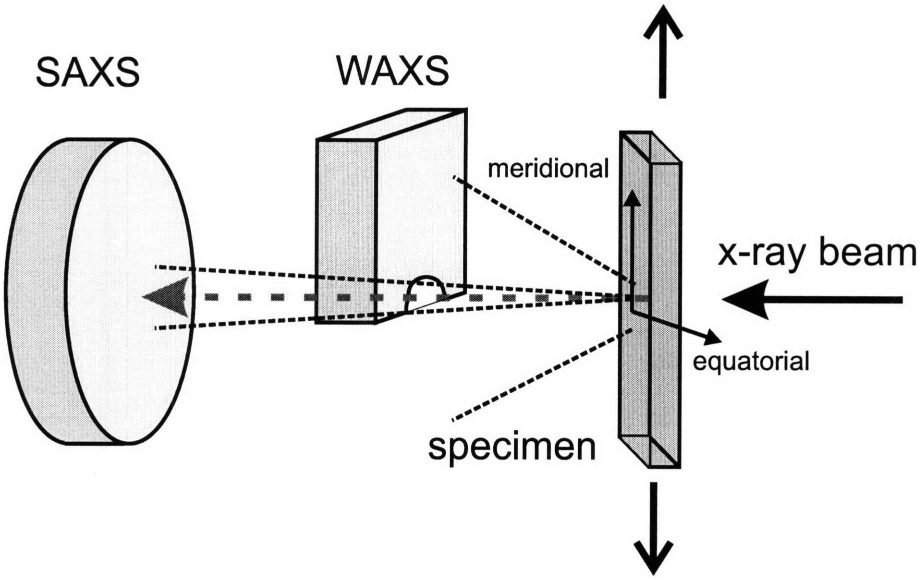

(a)

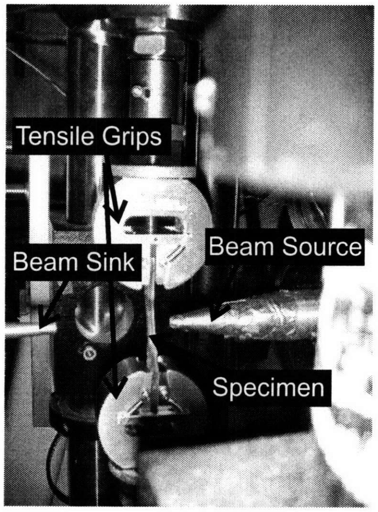

(b)

Figure 54: Experimental setup for simultaneous x-ray scattering and tensile tests.

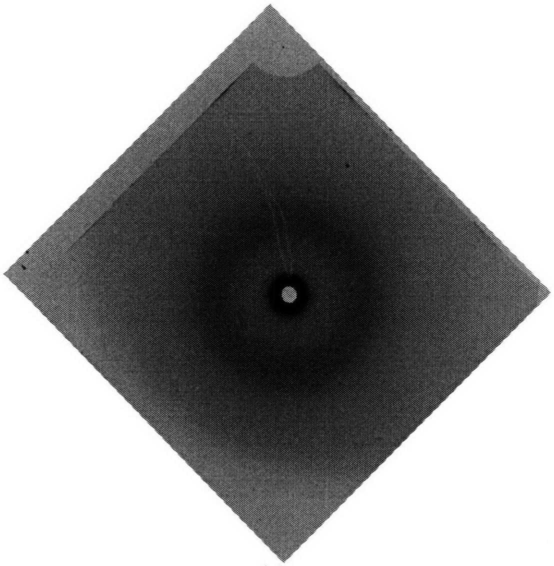

(a)

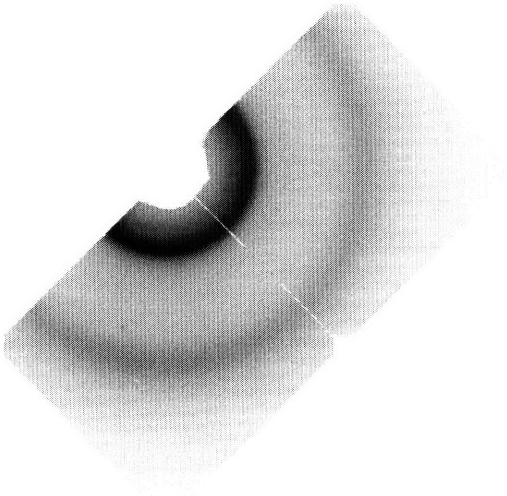

(b)

Figure 55: Xray scattering intensity profile for Nafion NRE212 in its undeformed state. (a) The SAXS profile is initially isotropic with a single peak. (b) The WAXS profile is initially isotropic with two peaks.

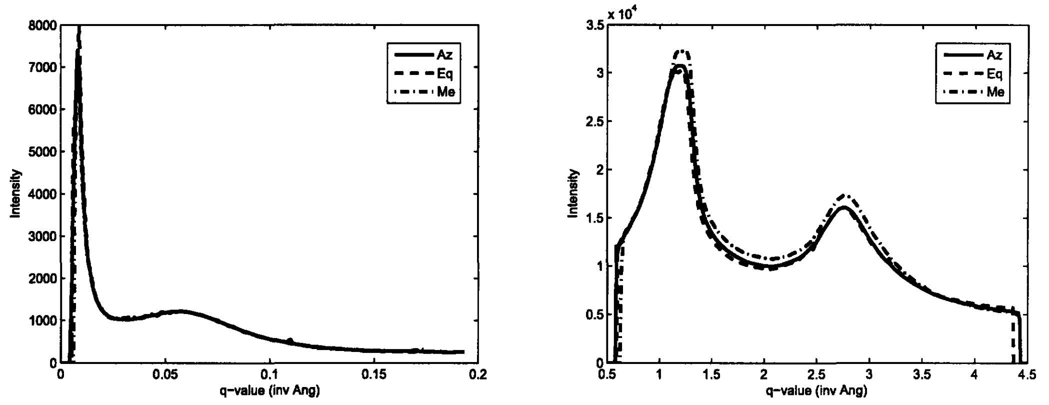

(a) (b)

Figure 56: The azimuthal, equatorial, and meridional intensity profiles for NRE212 in the undeformed state from (a) SAXS and (b) WAXS. Each of the peaks has the same intensity and location for azimuthal, equatorial, and meridional, indicating transverse isotropy.

in the case of the WAXS data. The SAXS and WAXS intensity profiles for the undeformed state are shown in figure 56.

Because of the initially isotropic state of the membrane, the equatorial, meridional, and azimuthal profiles show the same q-value and intensity level for all three peaks. The SAXS peak occurs at a q-value of $0.057\AA^{-1}$, the low angle WAXS peak occurs at a q-value of $3.07\AA^{-1}$, and the wide angle WAXS peak occurs at a q-value of $1.60\AA^{-1}$. There appears to be a slight anisotropy in the WAXS peaks with the meridional peaks having a slightly higher intensity than the equatorial peaks, but since the intensity increase is present in both peaks which ordinarily align in opposite manners, this difference is likely the result of a slight difference in the signal gain between the two sensors used to collect the wide angle scatter. These values are in line with those determined in experimental studies of extruded and recast Nafion. In extruded Nafion however, the material is anisotropic in its undeformed state. This difference is expected due to the different processing experienced by the two materials.

The three peaks evolve in terms of intensity, q-value, and angular distribution as the material is deformed in tension in the meridional direction. The SAXS peak changes to an elliptical conformation resulting in a large q-value in the equatorial direction and a smaller one in the meridional direction, the low angle WAXS peak increases in equatorial intensity, and the wide angle WAXS peak decreases in equatorial intensity as depicted in figure 57.

The azimuthal, equatorial, and meridional intensity profiles corrected for changes in specimen thickness are shown for five different strain levels in figure 58. From these plots it is easy to see the trends in each of the peaks as the specimen is uniaxially strained. The equatorial cut of the SAXS peak moves to a larger q-value and decreases in intensity while the meridional cut moves to a smaller q-value and increases in intensity. This is indicative of the change in the ionic cluster shape from circular to elliptical (with the major axis in the direction of applied strain for the cluster in real space). The equatorial cut of the low angle WAXS peak increases in intensity and shifts to a slightly larger q-value while the meridional cut decreases in intensity and moves to a lower q-value. The equatorial cut of the wide angle WAXS peak decreases in intensity while the meridional cut increases in intensity. These both indicate that the backbone bundles are rotating to align with the direction of applied strain and that the spacing between strands within the bundle is decreasing slightly.

In order to better understand the strain recovery and stress relaxation mechanisms of Nafion, xray scattering was conducted while the specimen was subjected to cyclic and stress relaxation loading profiles. Figures 60 and 61 show the evolution of the SAXS and WAXS intensity maps respectively as a specimen is drawn to a true strain of 0.6, unloaded, reloaded to true strain 0.6, and unloaded again. The corresponding true strain-time and true stress-time for this loading profile are shown in figure 59; the asterisks on the plots indicate the data points from which the intensity frames are taken.

In order to look at these changes more quantitatively, the peak location and intensity can be followed through time. The peak tracking for this large strain load, unload, reload, and unload is shown in figure 62 along with the true stress and true strain time evolution. When looking at this data it is important to note that the strain and diffraction data collected while the stress is zero is not reliable as the specimen is likely buckled. For a cycle of this large a strain, the meridional cluster peak moves to lower q-values (larger characteristic distance) until it merges with the non-diffracted beam. From this large a strain it barely recovers to a more isotropic configuration during unloading

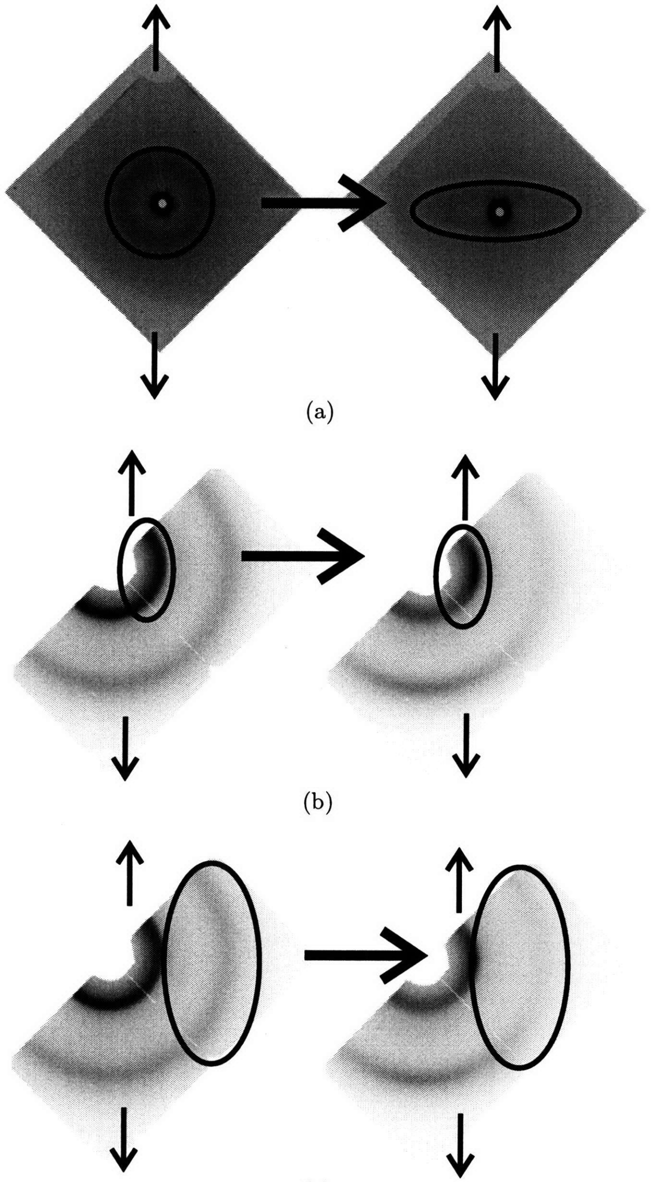

(a)

(b)

(c)

Figure 57: Basic features of the xray diffraction evolution with strain applied in the vertical direction: (a) the SAXS peak changes to an elliptical conformation resulting in a large q-value in the equatorial direction and a smaller one in the meridional direction; (b) the low angle WAXS peak increases in equatorial intensity; (c) the wide angle WAXS peak decreases in equatorial intensity.

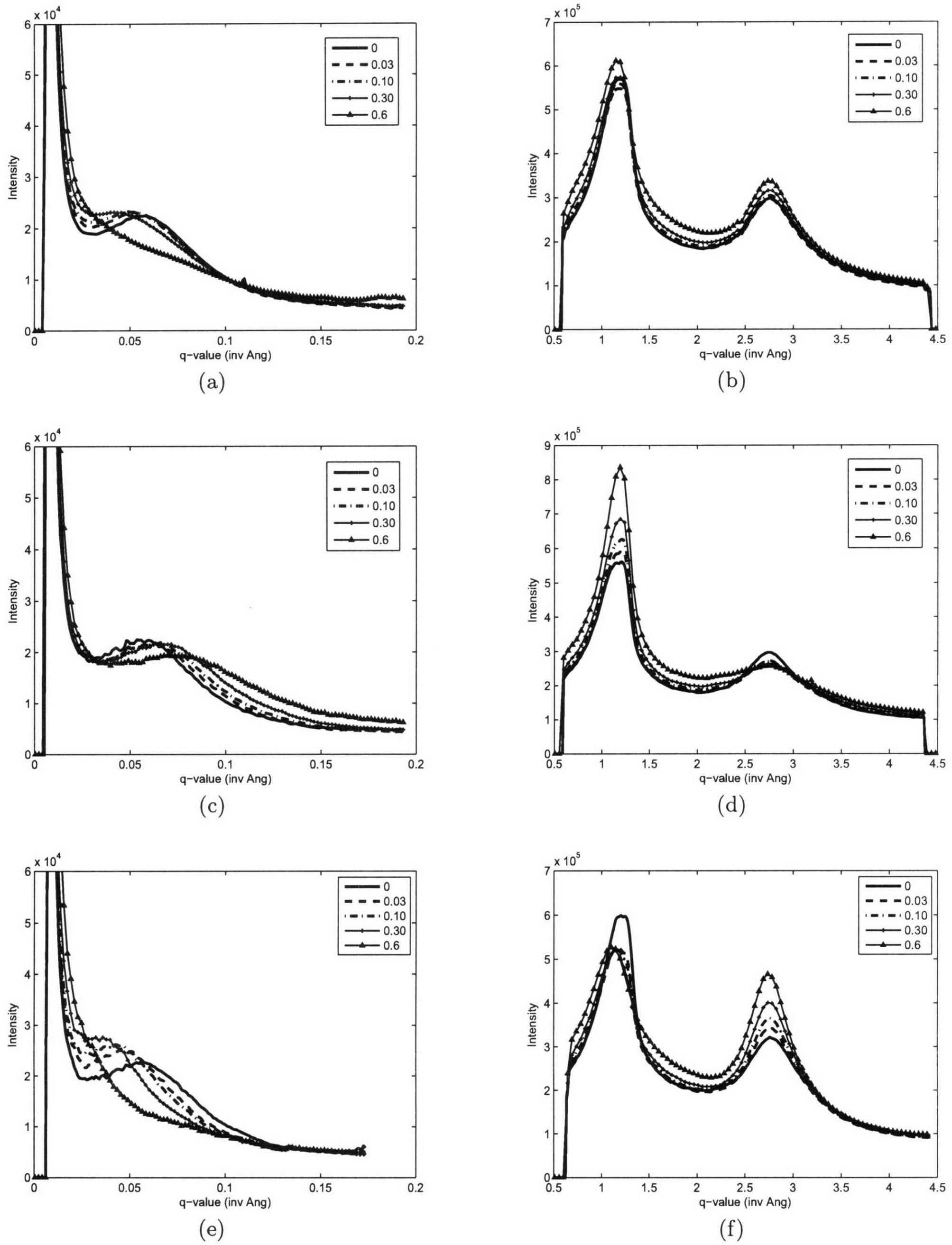

(a) (b) (c) (d) (e) (f)

Figure 58: Intensity versus q-value for five different strain levels(undeformed, elastic, at yield, post yield, large strain, see figure 19): (a) Azimuthal SAXS (b) Azimuthal WAXS (c) Equatorial SAXS (d) Equatorial WAXS (e) Meridional SAXS (f) Meridional WAXS .

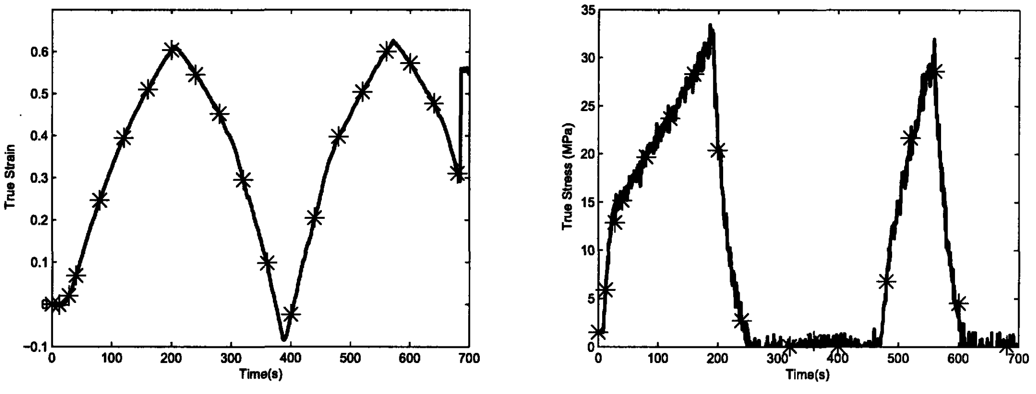

(a) (b)

Figure 59: True strain and true stress versus time for two uniaxial tensile load and unload cycles to a true strain of 0.6 at an engineering strain rate of $0.5/s$. The asterisks mark the locations at which the intensity maps of figures 60 and 61 are taken.

and it reaches the same location and intensity upon reloading. The WAXS peaks do not show any significant change in the peak location except for the low angle meridional peak which moves to a lower q-value with increasing strain and at any given strain during unloading and reloading returns to the q-value corresponding to that strain during initial loading. The equatorial cut for this peak shows the opposite trends but with much less overall movement. The intensity data for the WAXS peaks makes it clear that both the inter- and intra-molecular backbone alignment follow closely with strain for loading, unloading, and reloading.

Figures 64 and 65 show the evolution of the SAXS and WAXS intensity maps respectively for a loading profile in which the specimen was cycled to increasing strains. The corresponding true strain-time and true stress-time for this loading profile are shown in figure 63; the plus signs on the plots indicate the data points from which the intensity frames are taken. These intensity maps and the peak location and intensity tracking (Figure 66) show the same general trends as the simple extension and large cyclic tests, however, it can be seen that from low strain a significant amount of the isotropy in the SAXS peak is recovered.

Lastly, we can do the same analysis for stress relaxation tests. The strain-time, stress-time, and corresponding diffraction intensity maps are in figures 67 through 69. Each row of the intensity

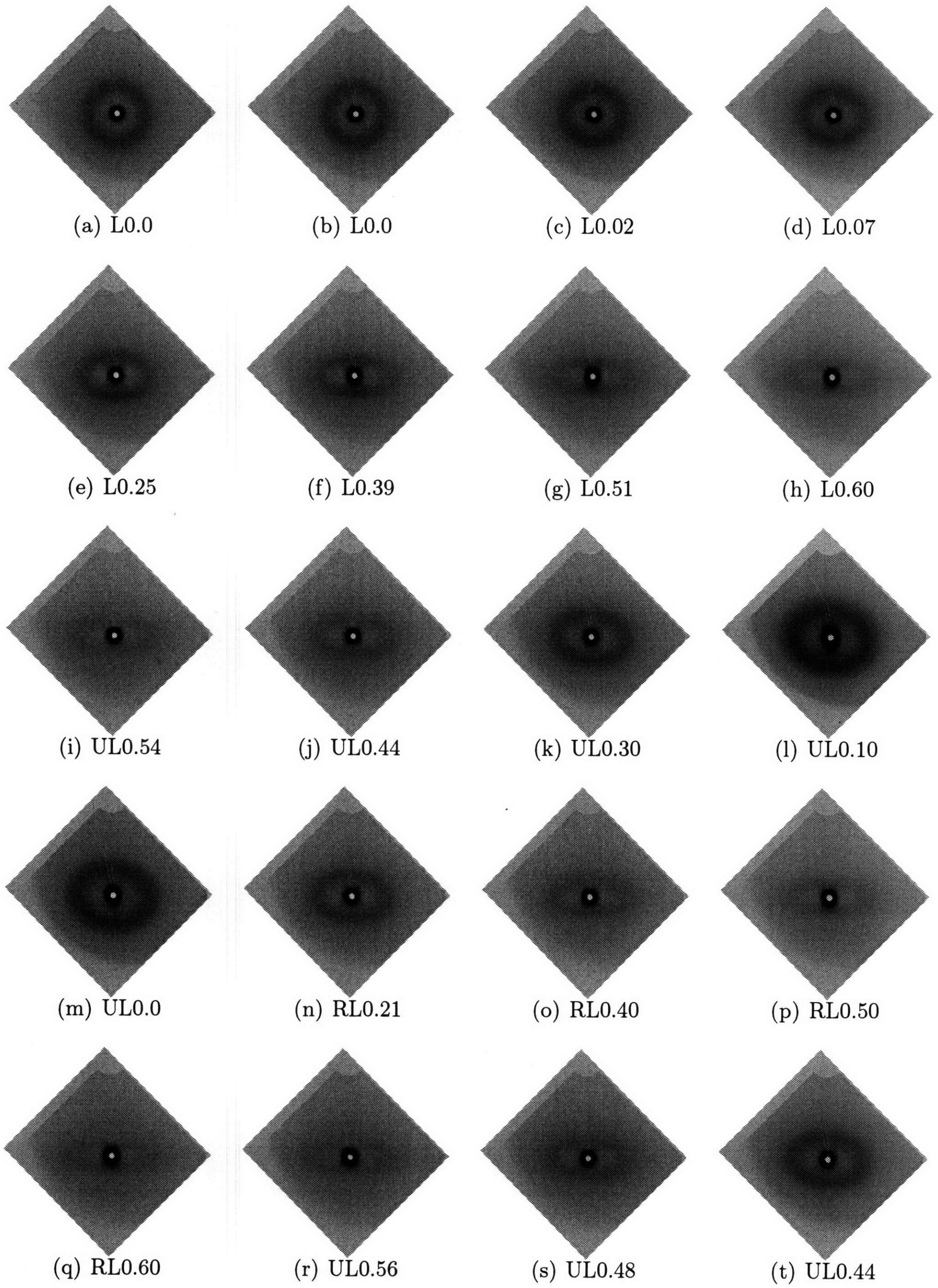

(a) L0.0 (b) L0.0 (c) L0.02 (d) L0.07

(e) L0.25 (f) L0.39 (g) L0.51 (h) L0.60

(i) UL0.54 (j) UL0.44 (k) UL0.30 (l) UL0.10

(m) UL0.0 (n) RL0.21 (o) RL0.40 (p) RL0.50

(q) RL0.60 (r) UL0.56 (s) UL0.48 (t) UL0.44

Figure 60: SAXS intensity map evolution for two uniaxial tensile load and unload cycles to a true strain of 0.6 at an engineering strain rate of $0.5/s$ (L=loading, UL=unloading, RL=reloading, number indicates tensile true strain).

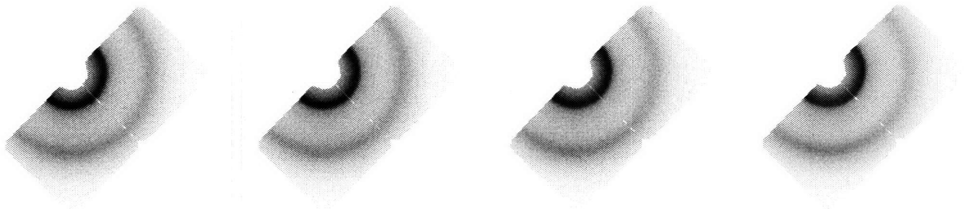

(a) L0.0 (b) L0.0 (c) L0.02 (d) L0.07

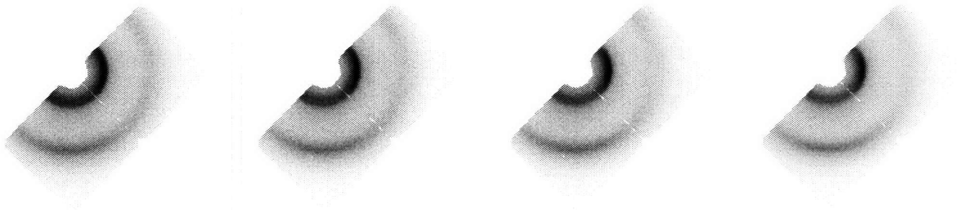

(e) L0.25 (f) L0.39 (g) L0.51 (h) L0.60

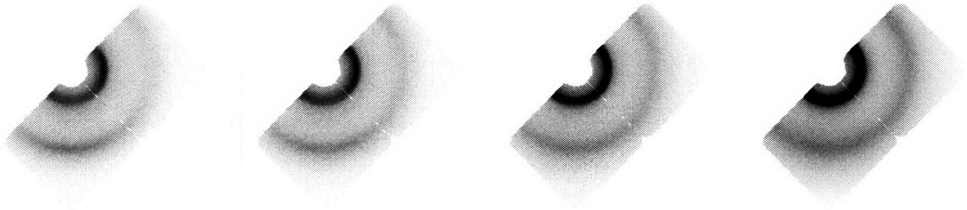

(i) UL0.54 (j) UL0.44 (k) UL0.30 (l) UL0.10

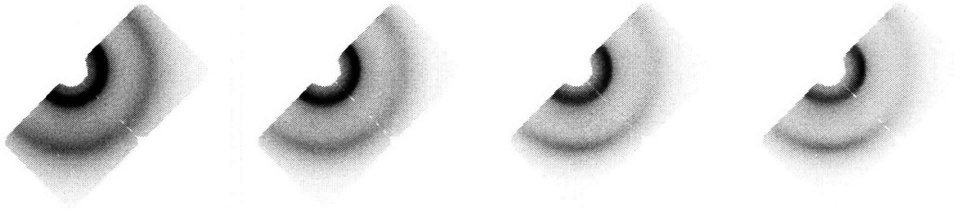

(m) UL0.0 (n) RL0.21 (o) RL0.40 (p) RL0.50

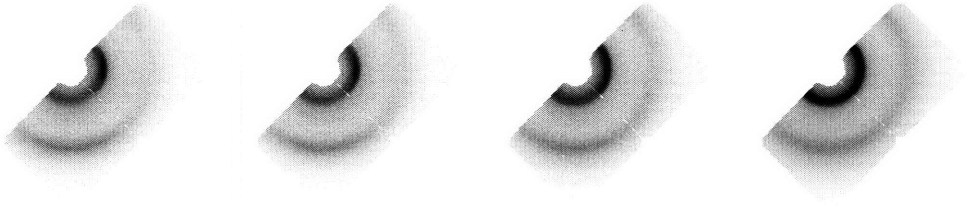

(q) RL0.60 (r) UL0.56 (s) UL0.48 (t) UL0.44

Figure 61: WAXS intensity map evolution for two uniaxial tensile load and unload cycles to a true strain of 0.6 at an engineering strain rate of $0.5/s$ (L=loading, UL=unloading, RL=reloading, number indicates tensile true strain).

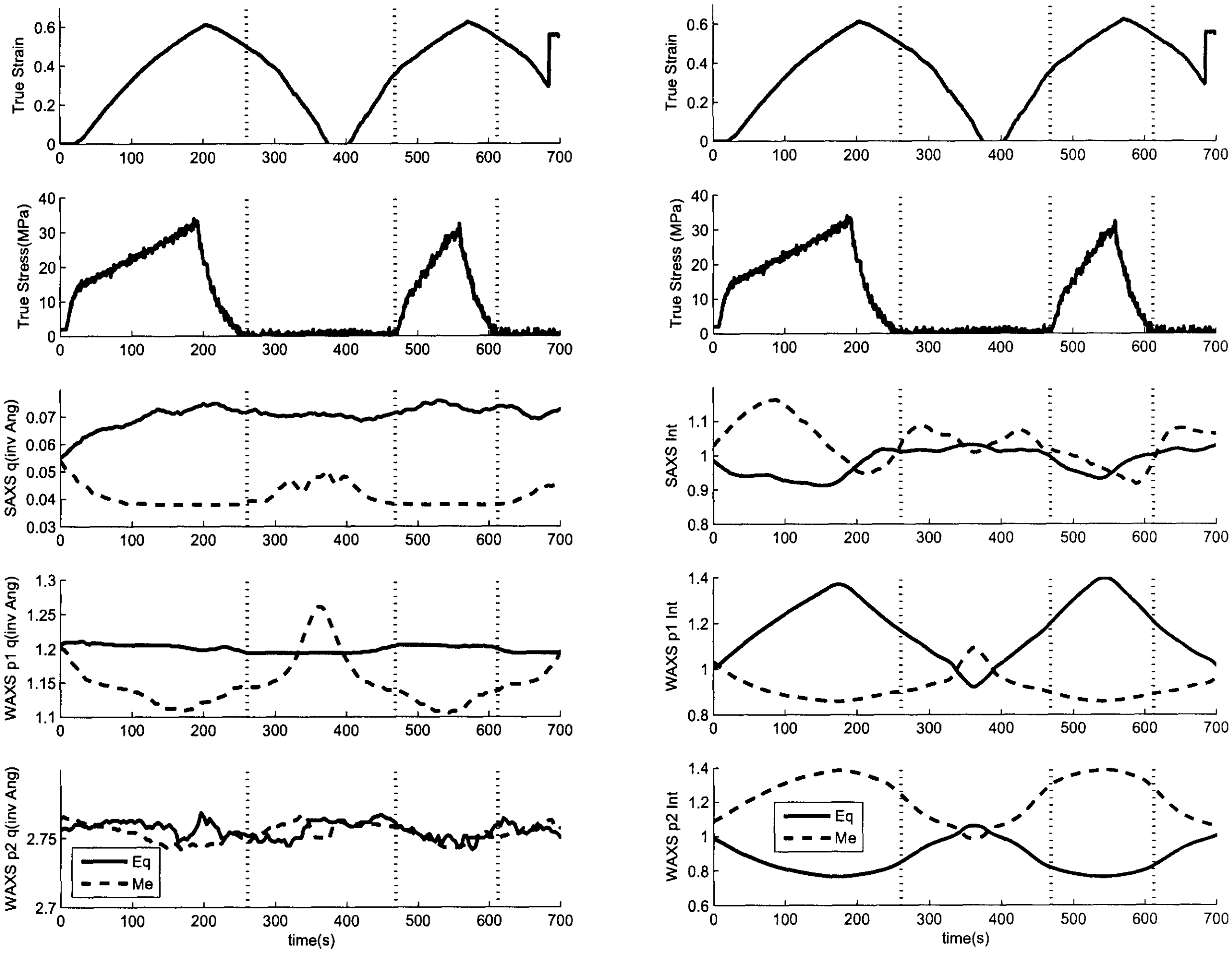

(a) (b)

Figure 62: Evolution of the xray diffraction peaks with time during two load and unload cycles to a true strain of 0.6 at an engineering strain rate of $0.5/s$; (a) peak location (b) peak intensity normalized by the azimuthal intensity.

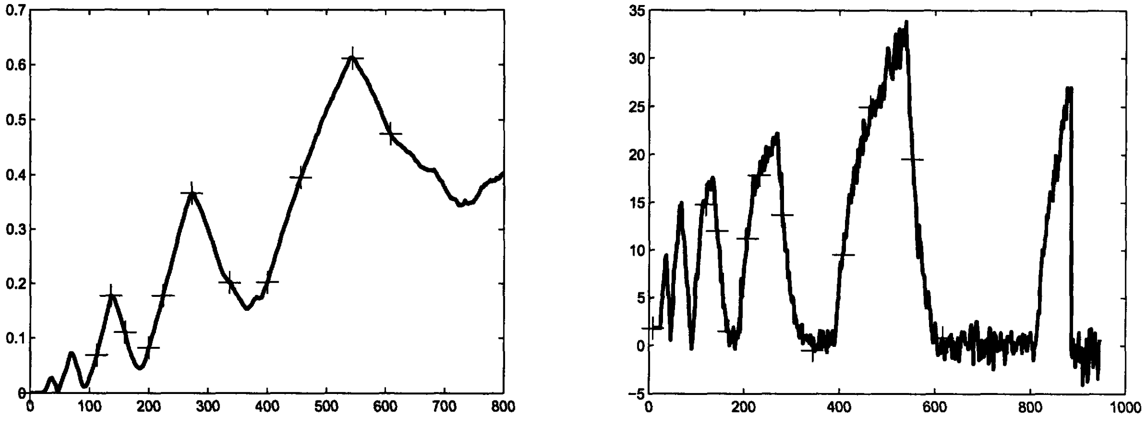

(a) (b)

Figure 63: True strain and true stress versus time for a specimen which is cycled to increasing strains at an engineering strain rate of $0.5/s$. The plus signs mark the locations at which the intensity maps of figures 64 and 65 are taken.

maps is from a specimen held at a constant strain over a period of 2 minutes. The changes during stress relaxation are too subtle to be noticeable directly from the intensity maps so we again look at the peak evolution (Figure 70). There is clearly no change in the intensity values of the WAXS peaks during the relaxation, but it appears there might be some relaxation in the cluster alignment. To further examine the SAXS relaxation we take a closer look at the stress relaxation that occurs at a strain of 0.36. Figure 71 shows the close relation between stress and the intensity of the meridional SAXS peak while the strain is held constant (both are normalized so that the magnitude varies from 0 to 1 while the strain is held constant). To verify that this is not just a relationship fabricated by the choice of method for analyzing the data, the same method is used for the equatorial cut of the WAXS peak (the low angle equatorial intensity is chosen because it has the same intensity trends as the SAXS meridional intensity) (Figure 72); there appears to be no correlation. The variation in the meridional SAXS intensity normalized by the azimuthal SAXS intensity from no strain to a strain of 0.36 is 0.131, for the equatorial WAXS normalized by the azimuthal WAXS intensity that number is 0.221 (roughly twice as large); the variation in the meridional SAXS intensity normalized by the SAXS azimuthal intensity while the strain as held at 0.36 is 0.0219, for the equatorial WAXS

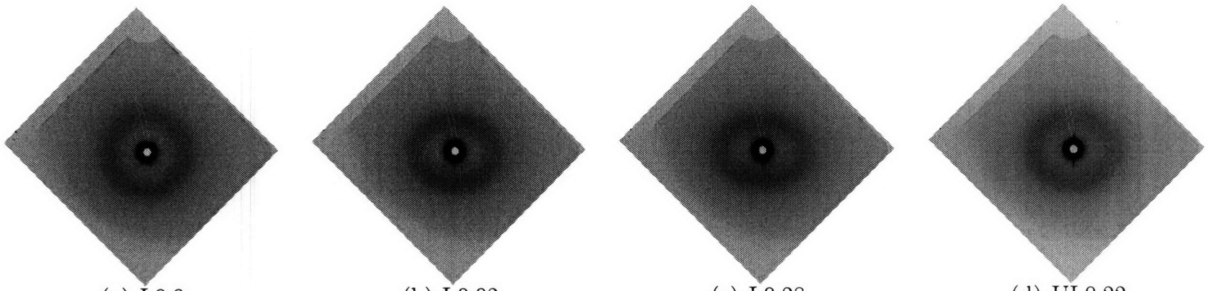

(a) L0.0 (b) L0.02 (c) L0.28 (d) UL0.22

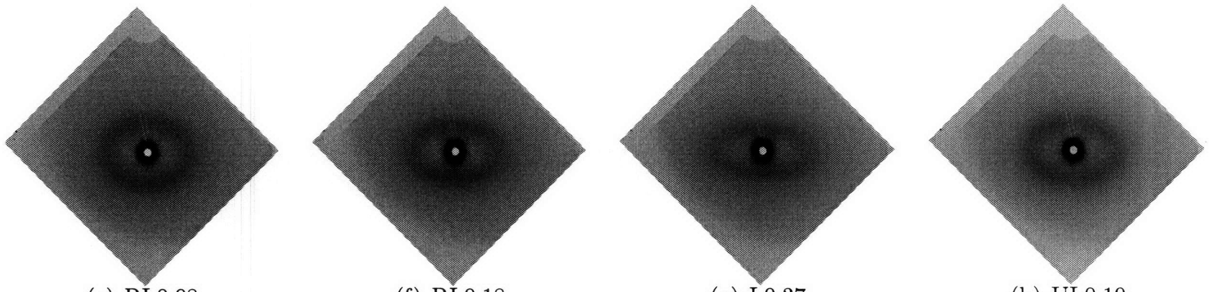

(e) RL0.08 (f) RL0.18 (g) L0.37 (h) UL0.19

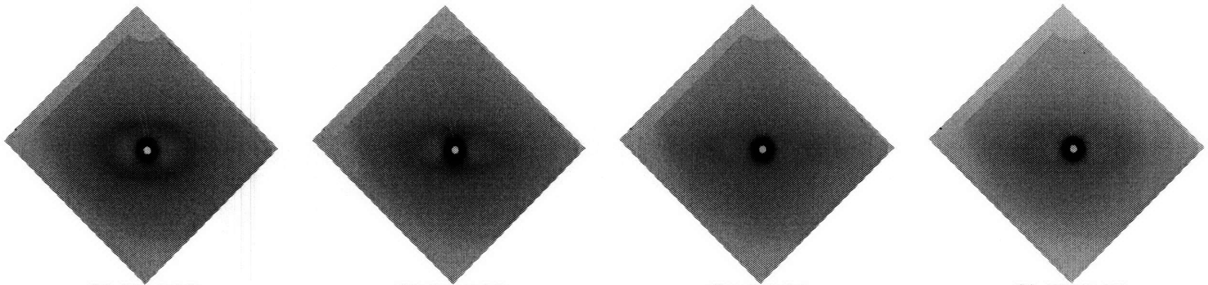

(i) RL0.20 (j) RL0.39 (k) L0.61 (l) UL0.47

Figure 64: SAXS intensity map evolution for a specimen which is cycled to increasing strains at an engineering strain rate of $0.5/s$ (L=loading, UL=unloading, RL=reloading, number indicates tensile true strain).

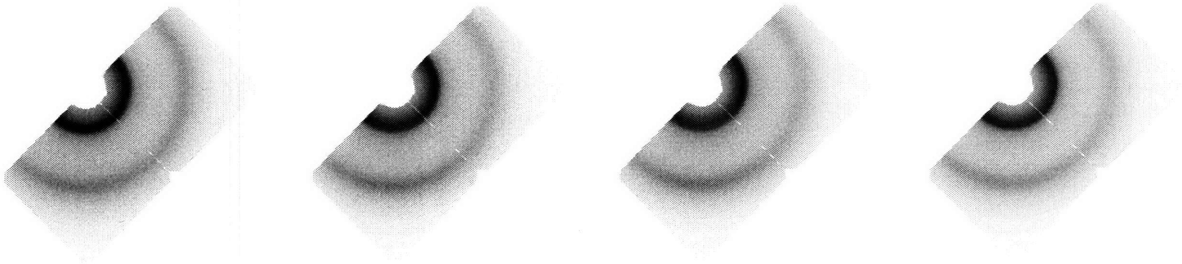

(a) L0.0 (b) L0.02 (c) L0.28 (d) UL0.22

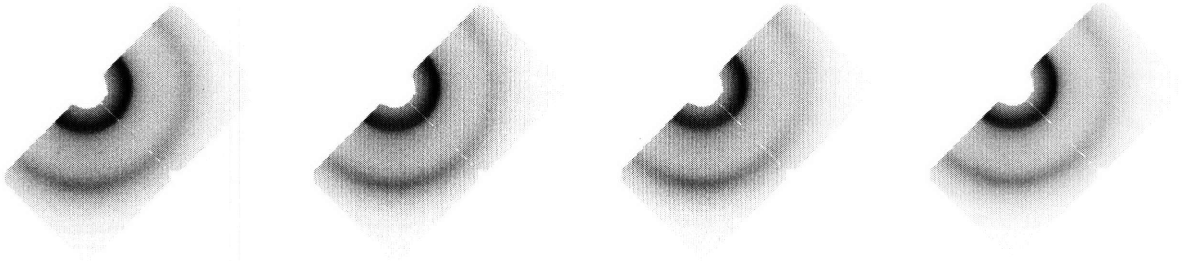

(e) RL0.08 (f) RL0.18 (g) L0.37 (h) UL0.19

(i) RL0.20 (j) RL0.39 (k) L0.61 (l) UL0.47

Figure 65: WAXS intensity map evolution for a specimen which is cycled to increasing strains at an engineering strain rate of $0.5/s$ (L=loading, UL=unloading, RL=reloading, number indicates tensile true strain).

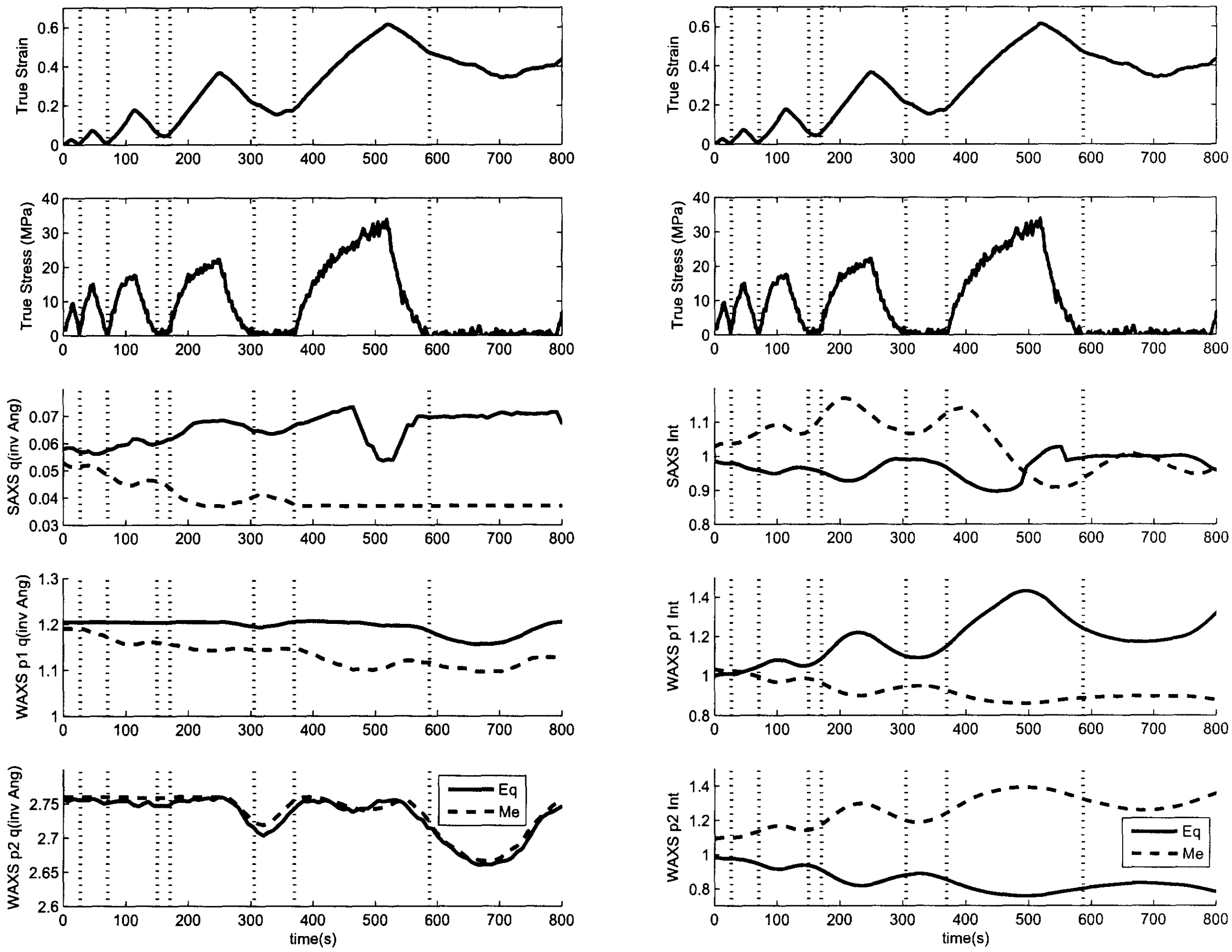

(a) (b)

Figure 66: Evolution of the xray diffraction peaks with time for a specimen which is cycled to increasing strains at an engineering strain rate of $0.5/s$; (a) peak location (b) peak intensity normalized by the azimuthal intensity.

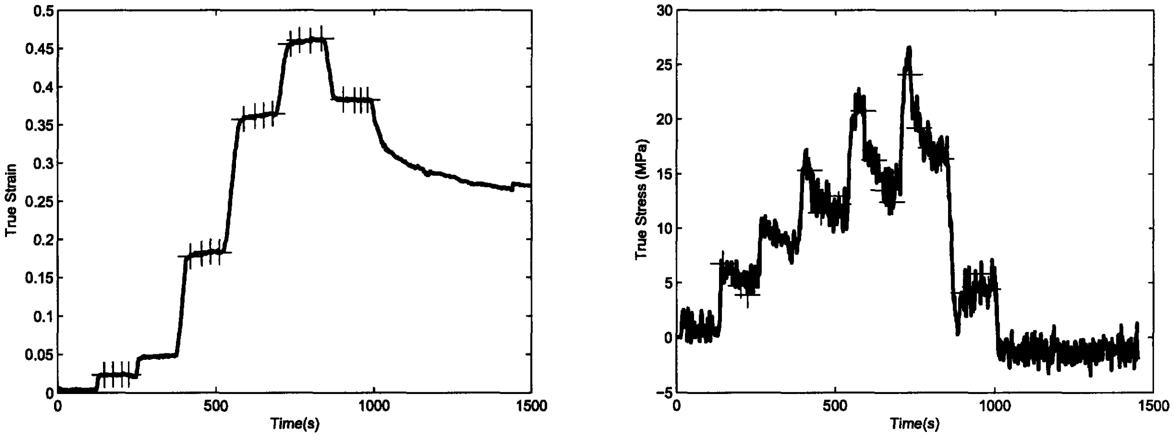

(a) (b)

Figure 67: True strain and true stress versus time for stress relaxation tests with loading at an engineering strain rate of $0.5/s$. The plus signs mark the locations at which the intensity maps of figures 68 and 69 are taken.

normalized by the WAXS azimuthal intensity that number is 0.0018 (an order of magnitude less). From this data it is clear that the ionic clusters lose orientation during a stress relaxation test, whereas the backbone bundles do not.

- Prior to Loading
  - strain is zero
  - stress is zero
  - ionic cluster SAXS peak is isotropic
  - low angle WAXS intermolecular backbone peak is isotropic
  - wide angle WAXS intramolecular backbone peak is isotropic
- During Loading
  - strain increases linearly
  - stress increases linearly at first and then exhibits a roll-over yield behavior followed by a modest non-linear strain hardening

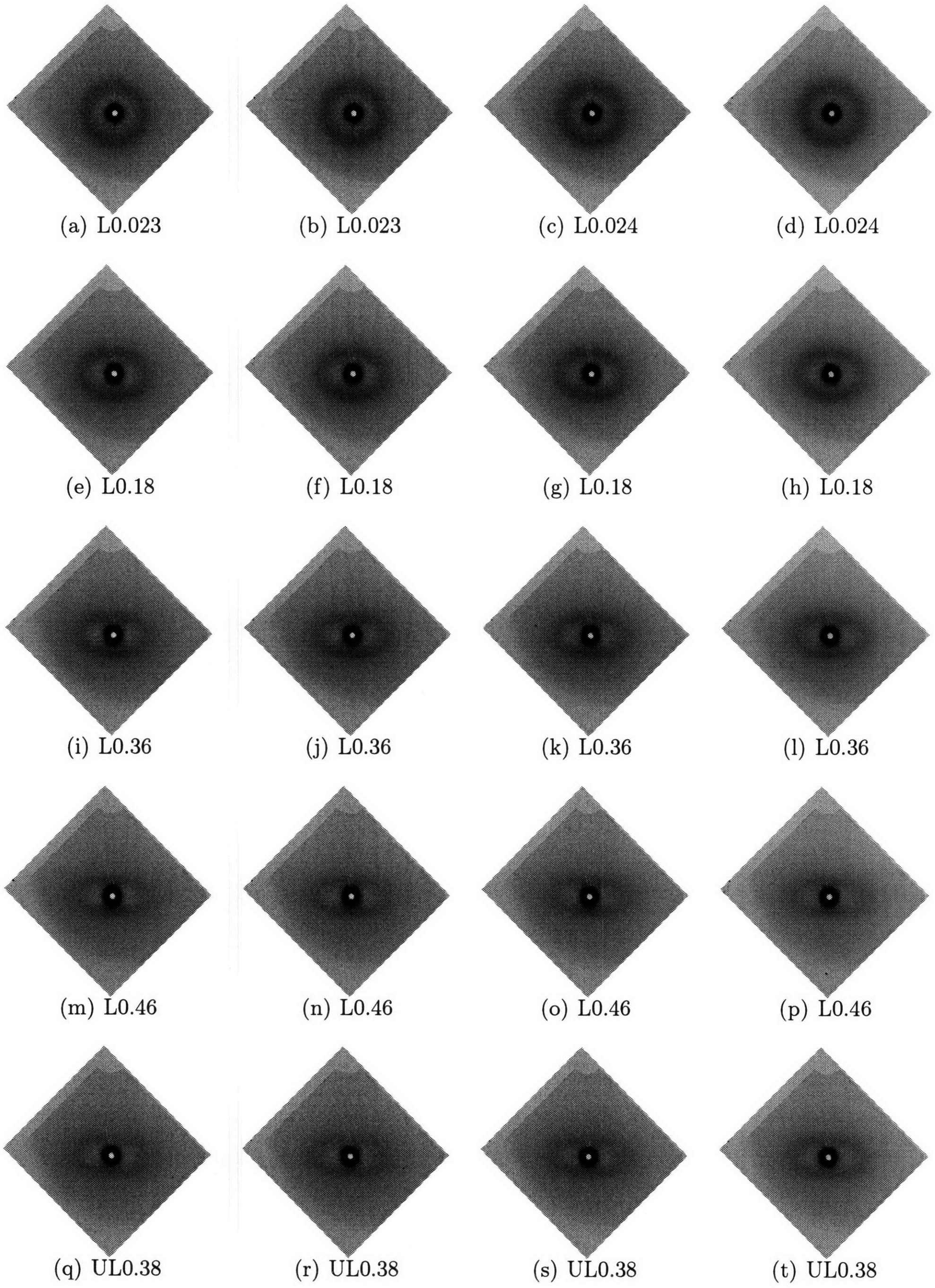

(a) L0.023 (b) L0.023 (c) L0.024 (d) L0.024

(e) L0.18 (f) L0.18 (g) L0.18 (h) L0.18

(i) L0.36 (j) L0.36 (k) L0.36 (l) L0.36

(m) L0.46 (n) L0.46 (o) L0.46 (p) L0.46

(q) UL0.38 (r) UL0.38 (s) UL0.38 (t) UL0.38

Figure 68: SAXS intensity map evolution for stress relaxation tests with loading at an engineering strain rate of $0.5/s$ (L=loading, UL=unloading, RL=reloading, number indicates tensile true strain).

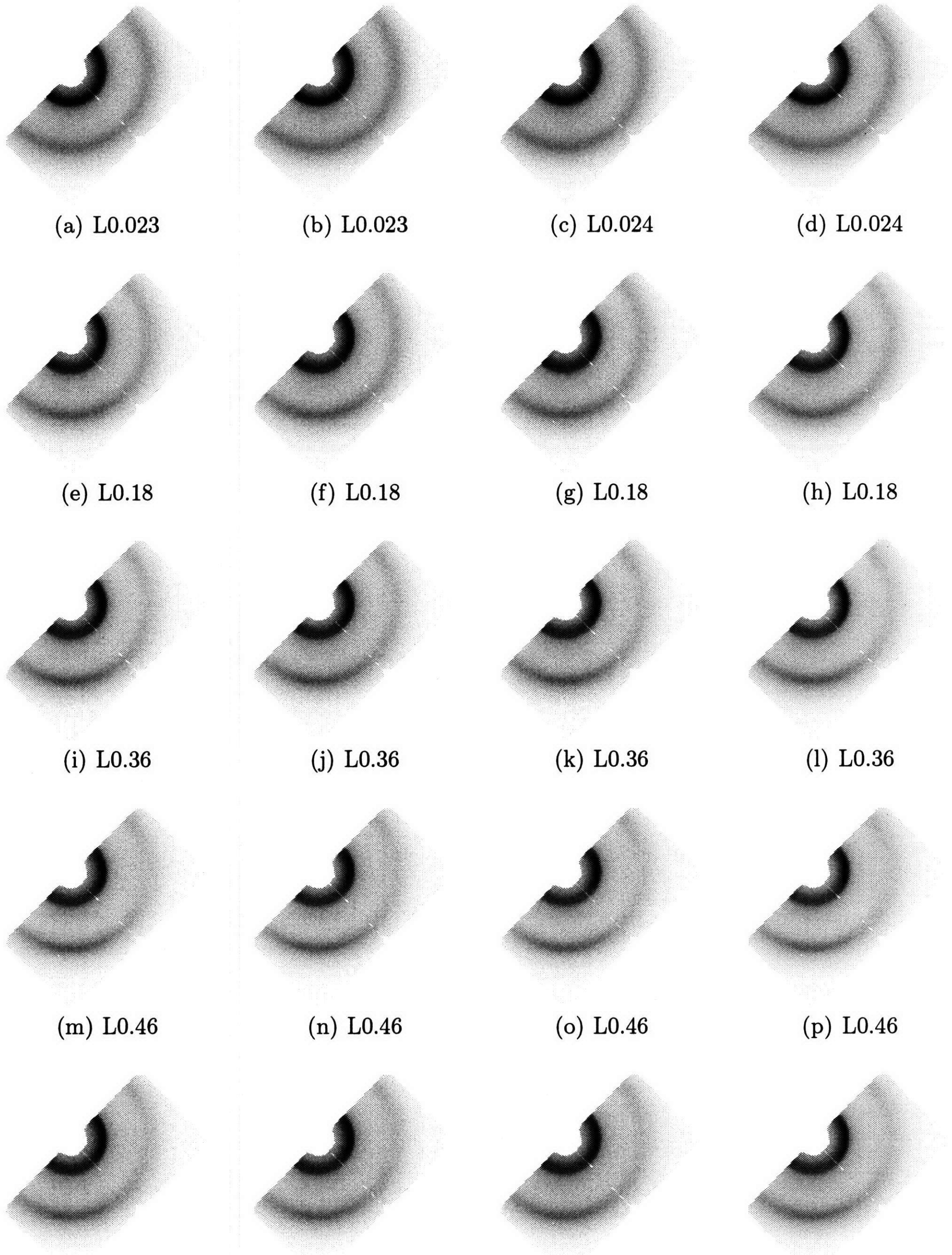

(a) L0.023
(b) L0.023
(c) L0.024
(d) L0.024
(e) L0.18
(f) L0.18
(g) L0.18
(h) L0.18
(i) L0.36
(j) L0.36
(k) L0.36
(l) L0.36
(m) L0.46
(n) L0.46
(o) L0.46
(p) L0.46
(q) UL0.38
(r) UL0.38
(s) UL0.38
(t) UL0.38

Figure 69: WAXS intensity map evolution for stress relaxation tests with loading at an engineering strain rate of $0.5/s$ (L=loading, UL=unloading, RL=reloading, number indicates tensile true strain).

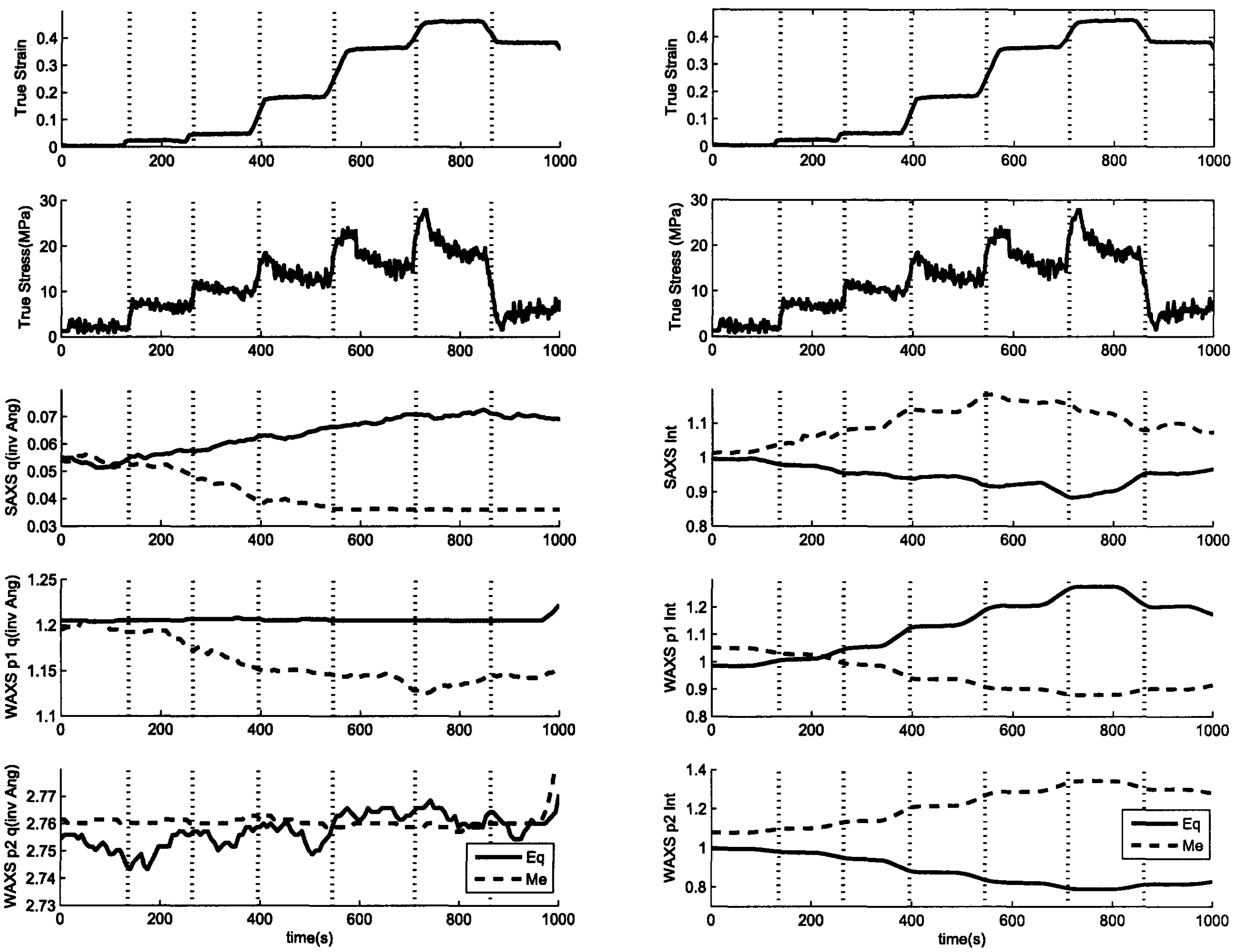

(a)

(b)

Figure 70: Evolution of the xray diffraction peaks with time during stress relaxation tests with loading at an engineering strain rate of $0.5/s$; (a) peak location (b) peak intensity normalized by the azimuthal intensity.

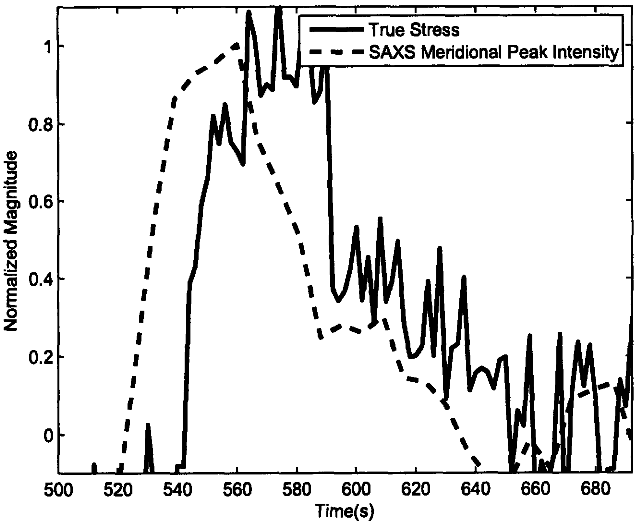

Figure 71: The comparison of the change in the SAXS meridional intensity and the true stress while the uniaxial tensile strain is held at 0.36 shows a good correlation between the two. Both quantities are normalized to vary between zero and one.

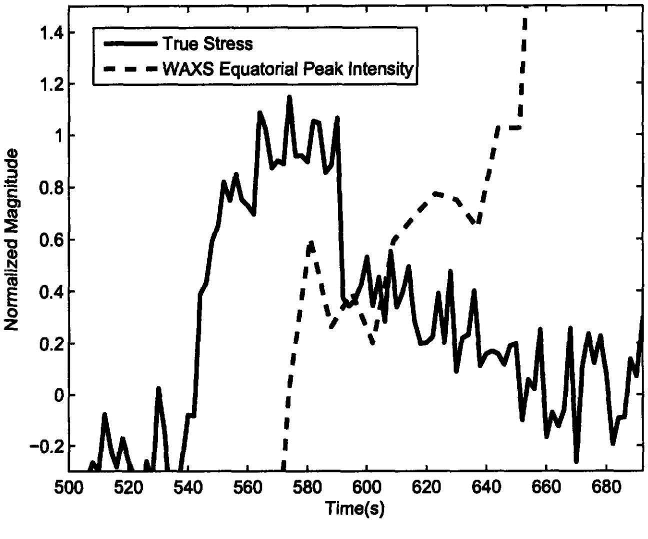

Figure 72: The comparison of the change in the WAXS low angle peak equatorial intensity and the true stress while the uniaxial tensile strain is held at 0.36 shows no correlation between the two. Both quantities are normalized to vary between zero and one.

  - ionic cluster SAXS peak becomes elliptical with major axis in the equatorial direction indicating a change in the cluster shape to elliptical with major axis parallel to the applied strain
  - low angle WAXS intermolecular backbone peak becomes more intense in the equatorial direction indicating alignment of the backbone bundles parallel to the applied strain
  - wide angle WAXS intramolecular backbone peak becomes more intense in the meridional direction indicating alignment of the backbone bundles parallel to the applied strain

- During Unloading
  - strain decreases linearly until the specimen buckles
  - stress decreases linearly at first and then exhibits a roll-over yield behavior until it reaches zero slightly before the specimen buckles
  - ionic cluster SAXS peak becomes less elliptical indicating a change in the cluster shape to less elliptical with major axis still parallel to the applied strain until the specimen buckles at which point the peak stops evolving
  - low angle WAXS intermolecular backbone peak becomes less intense in the equatorial direction indicating a reduction in the alignment of the backbone bundles parallel to the applied strain until the specimen buckles at which point the peak stops evolving
  - wide angle WAXS intramolecular backbone peak becomes less intense in the meridional direction indicating a decrease in the alignment of the backbone bundles parallel to the applied strain until the specimen buckles at which point the peak stops evolving

- While strain is held constant
  - strain remains constant
  - stress decreases exponentially
  - ionic cluster SAXS peak alignment decreases exponentially
  - low angle WAXS intermolecular backbone peak does not change

– wide angle WAXS intramolecular backbone peak does not change

This study has shown that while both the ionomer clusters and the backbone regions align with applied strain, they do so in different manners. The backbone alignment, as revealed by the two WAXS peaks, has a direct relation to strain. When the strain is increased, the alignment increases, when its held constant, the alignment remains, and when the strain is allowed to recover (as during cyclic tests) the backbone alignment recovers as much as the overall material strain does. The relationship between cluster deformation and strain is more complex. The clusters deform to an elliptical and eventually almost fibrillar morphology with applied strain, however, unlike the backbone, when the strain is held constant the clusters return to a more isotropic state. The magnitude of the recovery depends on the strain that was reached and seems to correlate closely with stress relaxation. The cluster morphology is not directly related to stress however, as it does not return to an isotropic state at zero stress upon unloading. This suggests that the clusters deform with the backbone at it aligns during applied strain, but that given time and a large enough applied stress the backbones will shear away from the clusters they are originally affiliated with and join up with other clusters instead. This allows the clusters to recover (and the stress along with it since not as much cluster deformation needs to be supported) while the backbone remains aligned. During unloading the clusters return to a more isotropic configuration, bring the backbone chains with them, however (except from very low strains), they do not have enough stored energy to return the backbone to an isotropic state and if backbone shearing has occurred there is no mechanism for that portion of backbone to recover. The entire material is therefore kinetically frozen in an anisotropic state with plastic deformation. This understanding will be used in the following chapter to develop both a conceptual and a mathematical material model.

4 Constitutive Model

4.1 Prior Nafion Models

Weber and Newman (2004) were the first to incorporate mechanical properties into a Nafion model for fuel cell applications. They created a one-dimensional model that includes conductivity, water transport, swelling, and stress-strain behavior of Nafion. Since the model is one-dimensional the mechanical behavior is captured simply by a bulk modulus, which itself is a function of temperature, water content, and equivalent weight with this functional dependence taken from a combination of Hsu and Gierke(1982) and Yeo and Eisenberg (1977) with the temperature dependence only valid for temperatures below the glass transition temperature. The stress is then calculated as the non-linear dilatational stress

$$\tau = -K ln(V_{con}/V_f) \tag{1}$$

$$K = \frac{Y}{3} = \frac{275}{3}\left(\frac{T_{ref}}{T}\right) exp\left[-0.1655\left(\frac{\hat{\lambda} M_o}{EW} + \frac{1200 - EW}{100}\right)\right] \tag{2}$$

where K is the bulk modulus, V_{con} is the volume of the membrane as constrained by the fuel cell environment and V_f is the volume the membrane would occupy if allowed to swell freely, Y is the elastic modulus, T_{ref} is the reference temperature, T is the absolute temperature, $\hat{\lambda}$ is the average water content, M_o is the molecular weight of water, and EW is the equivalent weight of the Nafion. The free swelling volume is based upon the assumption of additive molar volumes and is given by

$$V_f = V_o\left(1 + \frac{\hat{\lambda}_f \bar{V}_o}{\bar{V}_m}\right) \tag{3}$$

where $\bar{V}_o$ is the volume of the dry membrane, $\hat{\lambda}_f$ is the average water content in the free swelling membrane, and $\bar{V}_m$ is the partial molar volume of the membrane. The constrained volume is then:

$$V_{con} = V_o\left[1 + \frac{\hat{\lambda}_f \bar{V}_o}{\bar{V}_m}(1 - \chi)\right] \tag{4}$$

where χ is an input parameter representing the degree of constraint imposed by the boundary conditions.

The simulations conducted with this model revealed that swelling with constraints has a significant effect on the water content and transport properties of the membrane and that the stresses that develop in a membrane are significant and capable of deforming the gas diffusion layer bordering the membrane. This model is interesting as it takes into account coupled effects between conductivity, water distributions, and swelling, but from a mechanical behavior viewpoint it is rather simplistic. It is purely elastic and allows only for a volumetric deformation mode.

Tang, Santare et. al. (2006) assigned isotropic linear-elastic mechanical behavior as well as isotropic thermal and hydration expansion to the membrane. The elastic coefficient was taken to be independent of hydration and temperature. The hygro and thermal expansions were taken as linear and uncoupled, each with its own constant coefficient. This model was constructed two-dimensionally with a plane strain condition. It was then placed in a fuel cell repeat unit as shown in figure 73. The fuel cell segment was subjected to a single hygro-thermal cycle from $20°C$ and 35% relative humidity to $85°C$ and 100% relative humidity. From this study they concluded both that significant non-uniform stresses do arise from fuel cell constraints and that the magnitude and distribution of those stresses is highly dependent on the exact boundary conditions. In a follow-on study, Kusoglu et. al. (2006) expanded the model to include yielding by modeling it as elastic-perfectly-plastic as well as making the thermal and hydration dependencies more realistic. Both the elastic modulus and yield stress were given as functions of temperature and relative humidity based on experimental data from Tang, Karlsson et. al. (2006). The thermal and hygro-expansion remain uncoupled, with the thermal expansion coefficient taken as a constant and the hygro-expansion coefficient determined as a function of temperature and relative humidity. Inserting this new material model into the same simulation as in the first study, they found that significant residual stresses resulted after a single cycle both in-plane and out-of-plane and that shear stresses were negligible. While both these studies give some insight into how stresses might arise in a fuel cell environment, the material model is too simplistic to perform any realistic design studies and the choice of relative humidity as the governing parameter for the hydration dependent properties

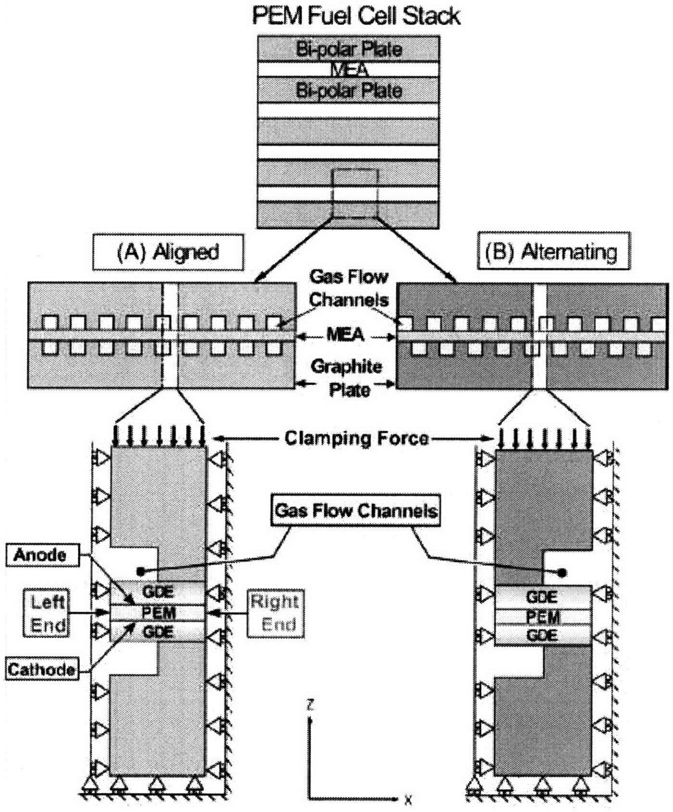

Figure 73: Repeat unit of fuel cell used in the simulations in Tang et. al. (May 2006) and Kusoglu et. al. (2006). The PEM is the Nafion membrane, the GDE is the combined gas diffusion layer and electrode, the MEA is the combination of the PEM and GDE. Aligned and alternating represent the two extremes for possible configurations of the anode and cathode side gas flow channels. In each case half a gas channel and half a confined area is taken as the repeat unit in the horizontal direction with the full MEA and half of a bipolar plate on each side taken as the repeat unit in the vertical direction.

of Nafion is questionable. It is the membrane water content and not the relative humidity of the environment which governs material behavior. Water content is only indirectly related to relative humidity with temperature, pressure, physical expansion constraints, the time of exposure to the environment, and the presence of liquid water all strongly affecting the correlation. As is evident from the experimental data in section 2.3.2 above, the true stress-true strain behavior is highly non-linear even at small strains and much of the deformation Kusoglu et. al. determined to be permanent might in fact be recovered by the highly non-linear visco-elastic behavior of Nafion.

Huang et. al. (2006) developed an elastic-plastic material model for the membrane electrode assembly (MEA) based on tensile tests conducted at room temperature and a range of relative humidities. The MEA studied consists of N111 (Nafion $25\mu m$ thick) with carbon supported platinum laced with recast Nafion resins as the electrolyte on each side. Isotropic expansion due to changes in relative humidity is included based upon values from literature (Morris 1993). While the authors acknowledge the importance of time dependent behavior, they do not include any in the MEA model. The elastic-plastic model is constrained by a rectangular edge seal and subjected to a humidity change from 75% to $0\%RH$ where a zero stress condition is assumed for $75\%RH$. They found that the strains were highest near the boundary with a peak strain of 2.675%. From their data this appears to be either within the linear-elastic region or just at the start of yielding. By its inclusion of the plastic regime with strain hardening, this model is in some ways more realistic than the two discussed above, however it does not have time or temperature dependency, and it makes the same assumption as the Tang, Santare et. al. and Kusoglu et. al. papers do in using relative humidity as the controlling parameter for hydration dependent behavior.

4.2 Summary of Important Mechanical Features

The model aims to capture the major features seen in the experimental data presented in Chapter 2 above using an understanding of the Nafion microstructure, particularly in light of the SAXS and WAXS analysis.

These features reiterated from chapter 2 are:

1) Initial linear elastic behavior, roll over yield, and strain hardening (Figure 74).

2) Strain rate dependence of yield stress (Figure 75).

3) Nonlinear elastic unloading and reloading (Figure 76).

4) Transition of stress relaxation behavior from the linear viscoelastic region through the yield and post-yield regions (Figure 77).

5) Dependence of all of the above on temperature and hydration (Figure 78).

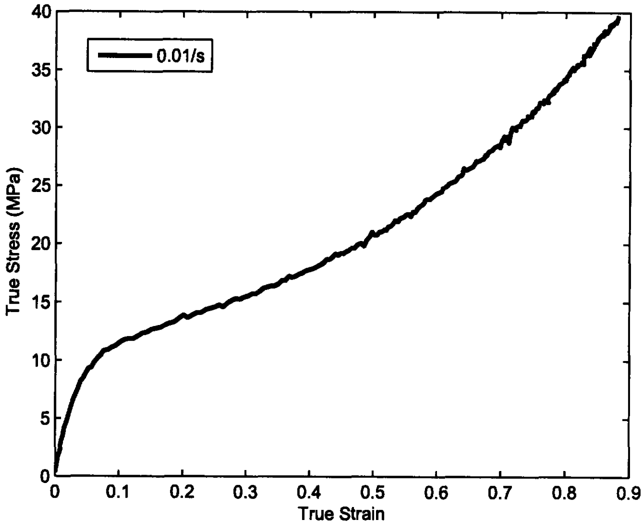

Figure 74: True stress-true strain behavior in uniaxial tension at 25°C and $.01/s$ showing an initial linear-elastic behavior followed by a rollover type yielding and strain hardening.

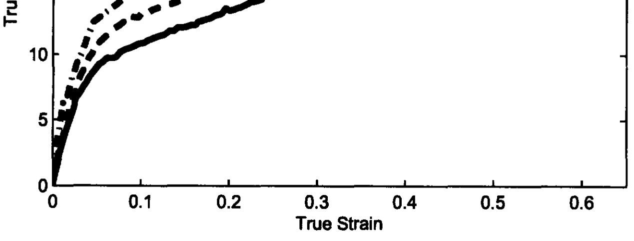

Figure 75: True stress-true strain behavior in uniaxial tension at multiple strain rates at 25°C showing the strain rate dependence of the yield stress.

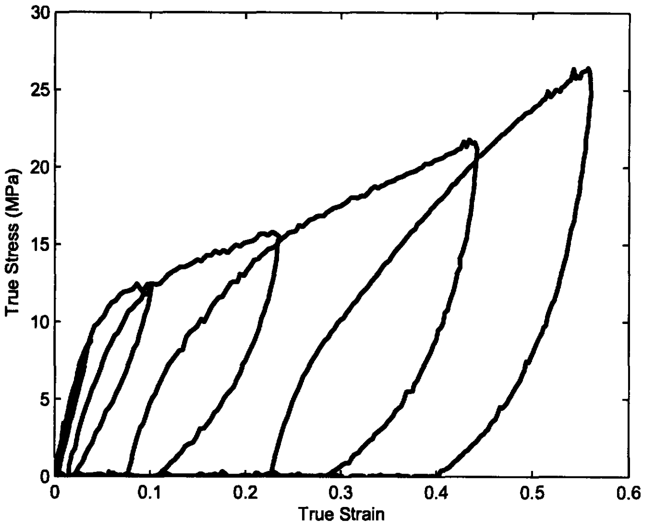

Figure 76: True stress-true strain behavior under uniaxial tensile cyclic loading conditions at $0.01/s$ and $25°C$ exhibiting nonlinear elastic unloading and reloading.

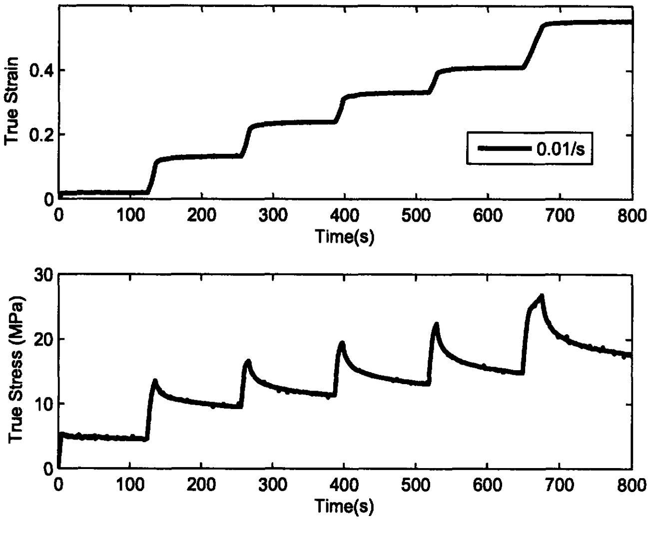

Figure 77: True strain-time and true stress-time for uniaxial tensile stress relaxation tests at increasing strain levels for loading rates of $0.01/s$ at $25°C$. The magnitude of the stress relaxation increases rapidly through yield and moderately as the strain is increased further.

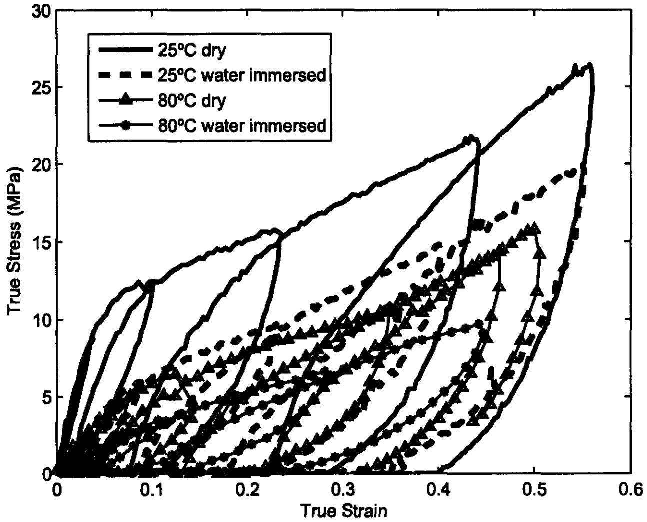

Figure 78: The effects of temperature and hydration on the true stress-true strain behavior under uniaxial tensile cyclic loading conditions at $0.01/s$.

4.3 Constitutive Model Development and Results

It is helpful when developing a microstructurally motivated constitutive model to have a conceptual model of the microstructure of the material and how the microstructure evolves with applied force or deformation. The model we propose builds upon the bundle-cluster model of Heijden et. al. (2004) elaborated on by Liu et. al. (2006). As discussed in chapter 3 above, Nafion is microphase separated into hydrophobic and hydrophilic domains. The hydrophobic domains are made of the relatively stiff PTFE backbone which is primarily amorphous but has crystalline domains distributed throughout (~ 5%). The hydrophilic domain consists of groups of sulfonic acid side chains which form into roughly cylindrical configurations and contain protons and varying amounts of water depending on the overall water content of the membrane. There are no chemical crosslinks between the different PTFE chains, so while the PTFE itself is stiff, it is physical entanglements and the ionic interactions between the side chains which determine the mechanical properties of the overall material. In the bundle-cluster model sections of the backbone are assumed to exist in small bundles that are randomly aligned with respect to other bundles; under small strains the bundles rotate so that they are aligned with each other; under large strain the bundles are all aligned and the aggregates are aligned within the bundles. The conceptual model proposed here (figure 79) agrees with the bundle-cluster model, however it emphasizes the role of the ionic clusters in controlling this deformation, particularly in controlling the recovery of the material after the load is removed. Prior to deformation the backbone is organized into bundles with amorphous regimes between them and the side chains are organized into ionomer clusters of circular cross section. When a small strain is applied the backbone bundles rotate about the clusters to accommodate the applied strain while the ionomer clusters are deformed to a slightly elliptical cross-section. As the strain is increased the clusters continue to become more elliptical until they reach an almost fibrillar morphology. When this occurs it becomes easier for the material to deform by shearing the backbone segments away from the clusters rather than for the clusters to deform further. If the material is unloaded before this shearing starts to occur it will have a significant amount of strain recovery as the ionomer clusters return to their initial configuration drawing the backbone segments back with them (although it will be kinetically frozen at a slightly elliptical rather than circular shape the degree of which depends on the strain that was applied). If the material is unloaded after a significant amount of backbone bundle shearing has occurred it will have significantly less strain recovery as there is no mechanism for the backbone segments to be drawn back to their original clusters.

4.3.1 Elastic-Plastic Model

As with any model, the goal is to capture the important behavioral features as simply as possible, so we first propose a linear-elastic viscoplastic model with network based strain hardening. A one dimensional rheological schematic of the proposed model is shown in figure 80. A fundamental assumption in the model structure is that the stress response of a material can be decomposed into multiple mechanisms. In this case two mechanisms are needed to model the material behavior: Mechanism A, depicted as a spring (linear) in series with a viscoplastic dashpot, represents the resistance to deformation due to the intermolecular interactions (i.e. clusters deforming and bundles rotating) while mechanism B, depicted as a spring (non-linear), represents the resistance due to the stretching and orientation of the molecular network.

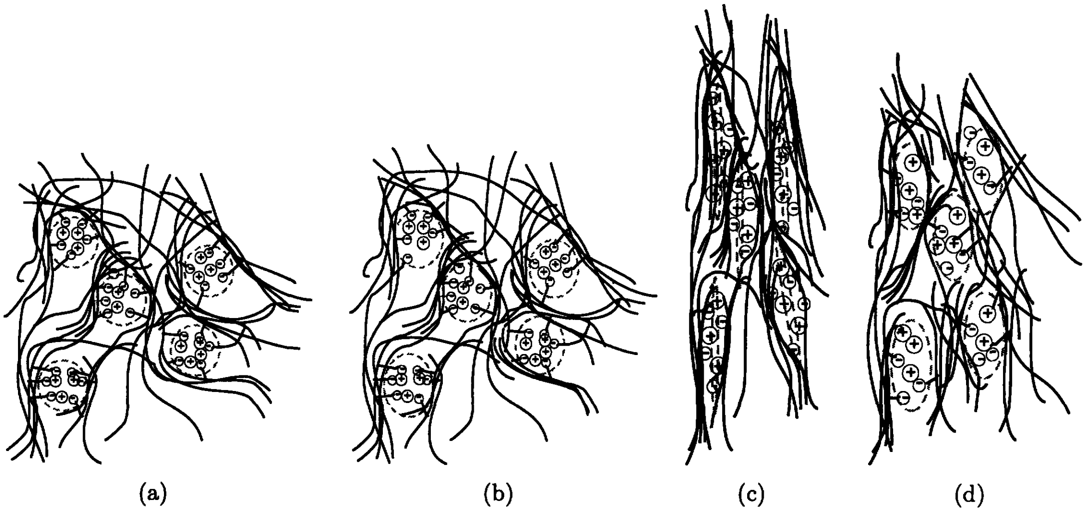
(a) (b) (c) (d)

Figure 79: Two dimensional conceptual model of how Nafion deforms in uniaxial tension. (a)Prior to deformation: The backbone is organized into bundles with amorphous regimes while the ionomer clusters have a circular cross section; (b)At small strain: The backbone bundles rotate to accommodate the applied strain while the ionomer clusters are deformed to a slightly elliptical cross-section; (c) At large strain: The bundles have aligned with the direction of applied strain and are shearing past each other and the clusters while the ionomer clusters have deformed to almost a fibrillar morphology; (d)After load is removed: The clusters recover partway to an elliptical cross section and the backbone bundles rotate back slightly to a more relaxed configuration, but the bundle fibers that have sheared past each other need not reaffiliate with their original clusters. The negative signs represent the negative charges at the end of the sulfonic side chains while the positive signs represent the hydrogen protons in the dry state and the hydrogen protons attached to water molecules in the hydrated state.

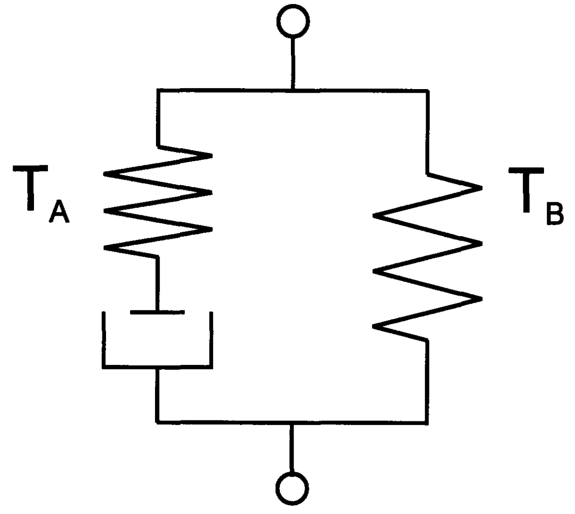

Figure 80: Schematic representation of the elastic-plastic model.

The total deformation gradient acts in full upon both of the main components of the model:

$$\mathbf{F} = \mathbf{F}_A = \mathbf{F}_B \tag{5}$$

where $\mathbf{F}_A$ is the deformation gradient for mechanism A, $\mathbf{F}_B$ is the deformation gradient for mechanism B, and the deformation gradient is defined as:

$$\mathbf{F} = \frac{\partial x}{\partial X} \tag{6}$$

The total stress acting on the system is equal to the sum of the stress contributions from the two mechanisms:

$$\mathbf{T} = \mathbf{T}_A + \mathbf{T}_B \tag{7}$$

The deformation gradient for mechanism A can be decomposed into its elastic and plastic contributions (Figure 81).

$$\mathbf{F}_A = \mathbf{F}^e_A \mathbf{F}^p_A \tag{8}$$

where $\mathbf{F}^e_A$ and $\mathbf{F}^p_A$ are the elastic and plastic deformation gradients for mechanism A.
The rate kinematics are described by the velocity gradient $\mathbf{L} \equiv \dot{\mathbf{F}}\mathbf{F}^{-1}$ which can be decomposed into its elastic and plastic components.

$$\mathbf{L}^e_A = \dot{\mathbf{F}}^e_A (\mathbf{F}^e_A)^{-1} \tag{9}$$

$$\mathbf{L}^p_A = \dot{\mathbf{F}}^p_A (\mathbf{F}^p_A)^{-1} \tag{10}$$

where $\mathbf{L}_A = \mathbf{L}^e_A + \tilde{\mathbf{L}}^p_A = \mathbf{L}^e_A + \mathbf{F}^e_A \mathbf{L}^p_A \, (\mathbf{F}^e_A)^{-1}$.
The plastic velocity gradient can be taken as the sum of the rate of stretching and the rate of spin.

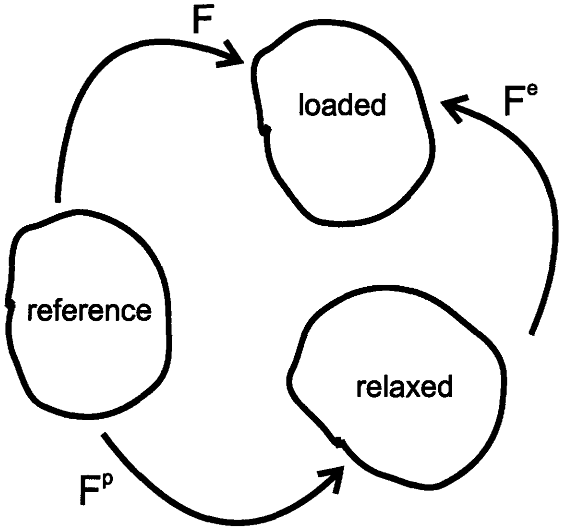

Figure 81: Schematic representation of elastic-viscoplastic framework.

$$\mathbf{L}^p = \mathbf{D}^p_A + \mathbf{W}^p_A \tag{11}$$

where $\mathbf{D}^p_A$ (symmetric tensor) is the rate of plastic stretching and $\mathbf{W}^p_A$ is the rate of plastic spin in the relaxed configuration.

$$\dot{\mathbf{F}}^p_A = \mathbf{L}^p_A \mathbf{F}^p_A \tag{12}$$

Plasticity has been experimentally shown in a wide range of materials to be a shear driven phenomenon. In general the scalar rate of plastic deformation is given by

$$\dot{\gamma}^P = \dot{\gamma}^o \exp\left[-\frac{\Delta G}{k_b \theta}\left(1 - \frac{\tau}{s + \alpha p}\right)\right] - \dot{\gamma}^o \exp\left[-\frac{\Delta G}{k_b \theta}\left(1 + \frac{\tau}{s + \alpha p}\right)\right] \tag{13}$$

where the first term is the forward process, the second term is the reverse process, $\dot{\gamma}^o$ is a material constant which captures the rate dependency, ΔG is an activation energy, k_b is Boltzmanns constant, θ is the absolute temperature, τ is the magnitude of the deviator of the stress tensor acting on the mechanism, s is the isotropic resistance to shear, α is the pressure coefficient, and p is the hydrostatic pressure. In polymers below the glass transition temperature the forward process dominates as the applied stress is large enough to drive the probability of the reverse process to essentially zero. While the characteristic moduli and flow stress of Nafion are significantly lower than that of most glassy polymers, it was found that the reverse process could still be neglected. Consequently only forward processes are taken into account.

The plastic stretching tensor in the loaded configuration is given as the product of the scalar rate of plastic deformation and a direction tensor:

$$\tilde{\mathbf{D}}^p_A = \dot{\gamma}^P_A \mathbf{N}^p_A \tag{14}$$

where the direction $\mathbf{N}^p_A$ is taken to be coaxial with the deviatoric portion of the mechanism A stress tensor $\mathbf{T}_A$.

$$\mathbf{N}^p_A = \frac{\mathbf{T}'_A}{|\mathbf{T}'_A|} \tag{15}$$

Without any loss of generality we take $\tilde{\mathbf{W}}^p_A = \mathbf{0}$. The magnitude of the plastic strain rate, $\dot{\gamma}^P_A$, is constitutively prescribed by

$$\dot{\gamma}^P_A = \dot{\gamma}^o \exp\left[-\frac{\Delta G}{k_b \theta}\left(1 - \frac{\tau_A}{s + \alpha p}\right)\right] \tag{16}$$

where $\dot{\gamma}^o$ is a material constant; ΔG is the activation energy; $\tau_A = \sqrt{\frac{1}{2}\mathbf{T}'_A\mathbf{T}'_A}$ is the equivalent shear stress; s is the isotropic resistance to plasticity; α is the pressure coefficient; and p is the pressure. This plastic stretching tensor can be convected back to the relaxed configuration by $\mathbf{L}^p_A = (\mathbf{F}^e_A)^{-1}\tilde{\mathbf{D}}^p_A\mathbf{F}^e_A$.

Now that a rule has been established for updating the plastic deformation gradient, the elastic deformation gradient can be obtained by equation 17.

$$\mathbf{F}^e_A = \mathbf{F}_A(\mathbf{F}^p_A)^{-1} \tag{17}$$

The second Piola-Kirchoff stress due to the intermolecular resistance is given by:

$$\mathbf{S}_A = (2\mu\mathbf{E}^{e\prime} + \kappa(\mathrm{tr}\mathbf{E}^e)\mathbf{I}) \tag{18}$$

where $\mathbf{S}_A$ is the second Piola-Kirchoff stress which is defined in the unloaded configuration and is work conjugate to the elastic Green-Lagrange strain; $\mathbf{I}$ is the second order identity matrix; μ is the shear modulus; κ is the bulk modulus; and $\mathbf{E}^e$ is the elastic Green-Lagrange strain. This strain measure is defined as:

$$\mathbf{E}^e = \frac{1}{2}\left({\mathbf{F}_A^e}^{\mathsf{T}}\mathbf{F}_A^e - \mathbf{I}\right) \tag{19}$$

The second Piola-Kirchoff stress can be convected to the loaded configuration by:

$$\mathbf{T}_A = \frac{1}{J}\mathbf{F}_A^e \mathbf{S}_A \mathbf{F}^{e\mathsf{T}} \tag{20}$$

where $\mathbf{T}_A$ is the Cauchy (true) stress and $J = det\mathbf{F}_A^e$ is the elastic volume change.

The stress due to the network resistance to deformation ($\mathbf{T}_B$) is derived from the entropic resistance to alignment of the molecular network by Arruda and Boyce (1993). It is prescribed by the Arruda-Boyce eight-chain rubber elasticity model as given in equation 21 below.

$$\mathbf{T}_B = \frac{1}{J}\mu_B \frac{\sqrt{N}}{\lambda_{chain}}\mathcal{L}^{-1}\left(\frac{\lambda_{chain}}{\sqrt{N}}\right)\mathbf{B}_B' \tag{21}$$

where $J = det\mathbf{F}_B$ is the volume change; μ_B is the rubbery shear modulus; $\sqrt{N}$ is the limiting chain extensibility; $\mathcal{L}$ is the Langevin function defined by $\mathcal{L}(\beta) \equiv \coth\beta - \frac{1}{\beta}$; $\lambda_{chain} = \sqrt{\frac{\mathrm{tr}\mathbf{B}}{3.0}}$ is the stretch on a chain in the eight-chain network; and $\mathbf{B}_B'$ is the deviatoric part of the left Cauchy-Green tensor ($\mathbf{B}_B = \mathbf{F}_B{\mathbf{F}_B}^{\mathsf{T}}$).

In order to fit this model 6 parameters are needed, each is taken from specific characteristics of the stress-strain behavior. The shear (μ) and bulk (κ) moduli of mechanism A are calculated from the initial linear elastic deformation of the specimen in uniaxial tension via the elastic modulus E and Poisson's ratio ν.

$$\mu = \frac{E}{2(1+\nu)} \tag{22}$$

Model Component	**Material Parameter**	**Value**
Elastic	μ	$3.33 \times 10^{8} Pa$
	κ	$1.11 \times 10^{8} Pa$
Plastic	$\dot{\gamma}^{o}$	$200 s^{-1}$
	ΔG	$9 \times 10^{-20} J$
	s	0.113μ
Network	μ_B	$1.95 \times 10^{6} Pa$
	$\sqrt{N}$	2.5

Table 2: Material properties for elastic-plastic model.

$$\kappa = \frac{E}{3\,(1 - 2\nu)} \tag{23}$$

The elastic modulus is the initial slope of the stress-strain curve. The Poisson's ratio, defined as:

$$\nu = -\frac{\epsilon_{tr}}{\epsilon_{ax}} \tag{24}$$

where ϵ_{tr} is the transverse strain and ϵ_{ax} is the axial strain, is determined from the video extensometer images.

The material constant which captures the rate dependency, $\dot{\gamma}^{o}$, and the activation energy, ΔG, are fit to the magnitude of the yield stress and its variation with strain rate. The isotropic resistance to plasticity s is arbitrarily assigned as a fraction on the shear modulus and is therefore not considered a fit parameter as the choice of that fraction is directly compensated by the value chosen for ΔG.

The rubbery shear modulus μ_B and the limiting chain extensibility $\sqrt{N}$ are fit from the post-yield portion of the uniaxial true stress-true strain curve. μ_B is determined from the initial slope of the post-yield strain hardening, whereas $\sqrt{N}$ is determined from the upturn of the true stress-true strain behavior at larger strains.

The values of each of the material properties are listed in table 2.

Figure 82 shows the success of this model in capturing the strain rate dependence of the uniaxial tensile stress-strain behavior.

The elastic-viscoplastic model is effective at capturing the basic features of the loading curve

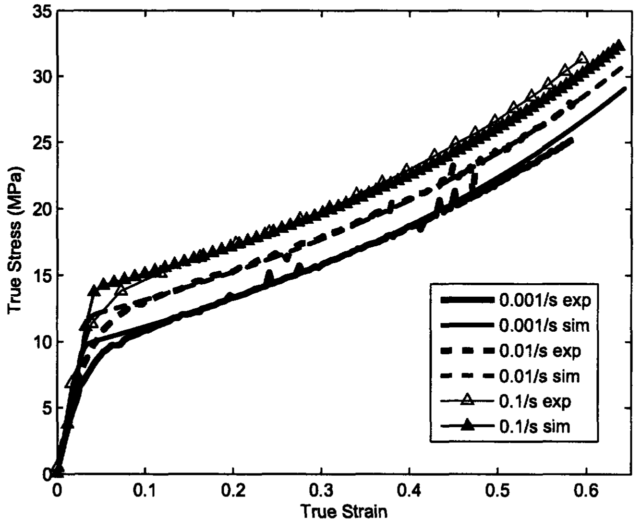

Figure 82: Strain rate dependence of true stress-true strain behavior in uniaxial tension: simulation vs experiment for the elastic-viscoplastic model.

and the strain rate dependence, however the only mention of either temperature or hydration is in the Arrhenius type dependence of the yield behavior. As is evident in figure 83 this is not enough to account for the changes in mechanical behavior dependence on temperature. While the Arrhenius type dependence is usually sufficient for the yield dependence below the glass transition temperature, it does not account for the significant structural rearrangements the material undergoes as it changes from a glassy (or in this case leathery) to rubbery behavior. As was shown in the DMA data in section 2.3.1, the glass transition for Nafion is quite broad beginning as low as $25°C$ and becoming steep around $70°C$. Further, nothing in the model so far accounts for changes in the shear modulus with temperature.

4.3.2 Elastic-Hygro-Thermo-Viscoplastic Model

In order to account for the mechanical behavioral dependence on temperature and water content both the shear modulus μ and the isotropic resistance to plastic deformation s must be described as functions of each. When the temperature is increased thermal fluctuations of the molecules increase resulting in a greater freedom of motion that presents itself as a decrease in the elastic modulus and yield stress. Hydration has a similar effect, in particular it should decrease the stress

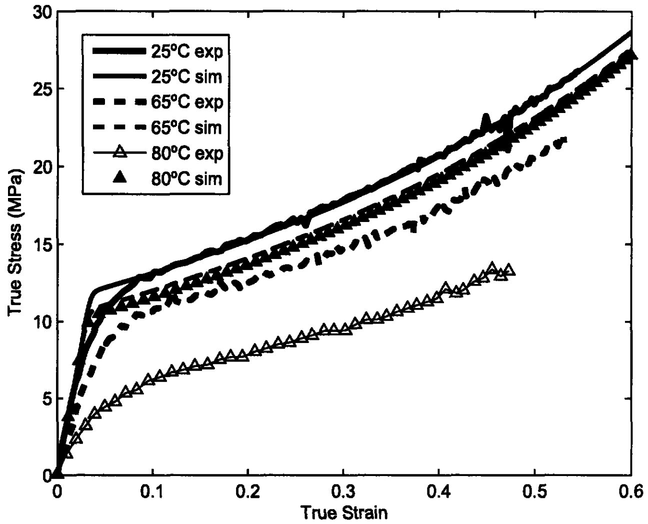

Figure 83: Temperature dependence of true stress-true strain behavior in uniaxial tension: simulation vs experiment for the elastic-viscoplastic model.

required to deform the ionic clusters where most of the water is retained. These two parameters are assigned the same functional dependence and are determined directly from the variation of the yield stress with temperature and water content. The hydration and thermal dependencies are taken to be uncoupled as justified by the experimental analysis, however it should be used with caution at temperatures approaching the glass transition temperature. The thermal (RF_θ) and hydration (RF_φ) functional dependencies are shown in equations 25 and 26 respectively.

$$RF_\theta = \left(-2.6718 \times 10^{-4}\right)\theta^2 + (.1636)\theta - 24.014 \tag{25}$$

$$RF_\varphi = 0.62\frac{1}{\exp\left[0.4\left(\varphi - 1\right)\right]} + 0.38 \tag{26}$$

where RF_θ is the thermal reduction factor, RF_φ is the hydration reduction factor, θ is the absolute temperature, and φ is a measure of the water content, defined as (1+swelling percentage relative to room temperature and relative humidity) for ease of use with the experimental data. The total reduction factor is taken as the product of the thermal and hygro reduction factors $RF = RF_\theta RF_\varphi$. The value of the shear modulus and isotropic resistance to plastic deformation at any hygro-thermal

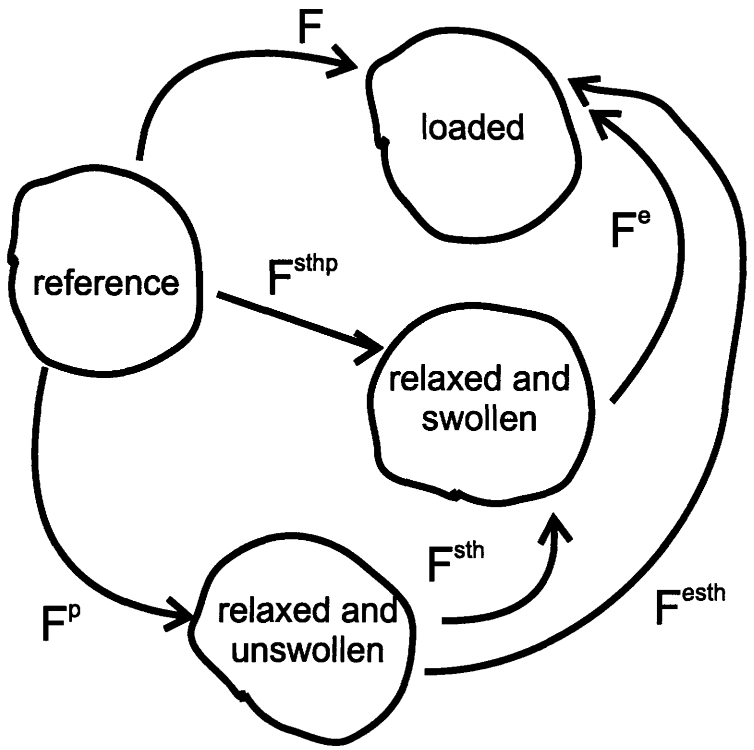

Figure 84: Schematic representation of hygro-thermo-elastic-viscoplastic framework.

state can then be found by equations 27 and 28 respectively.

$$\mu = \mu_o \hat{R} F(\theta, \varphi) \tag{27}$$

$$s = s_o \hat{R} F(\theta, \varphi) \tag{28}$$

While this is all that is needed to account for the change in the elastic modulus and yield stress observed when the temperature or water content is increased, it does not account for the volumetric expansion caused by either the temperature or hydration increase in the absence of any constraint. The incorporation of this effect follows Weber and Boyce (1989) and Mulliken (Phd Thesis) with the inclusion of hygro-swelling into the thermal expansion framework as shown in figure 84. The rheological picture for this is the same as in the elastic-plastic model, however the A-side dashpot now accounts for the hygro-thermal swelling in addition to the plastic deformation.

A path can be taken either from the reference configuration to the plastically deformed configuration, to the plastic and swollen configuration, to the deformed configuration, or directly from the reference configuration to the plastic and swollen configuration, to the deformed configuration. These deformations can therefore be multiplicatively decomposed via either path as expressed in equation 29.

$$\mathbf{F}_A = \mathbf{F}^e_A \mathbf{F}^{sth}_A \mathbf{F}^p_A = \mathbf{F}^e_A \mathbf{F}^{sthp}_A \tag{29}$$

where $\mathbf{F}^e_A$, $\mathbf{F}^{sth}_A$, $\mathbf{F}^p_A$, $\mathbf{F}^{sthp}_A$ are the elastic, hygro-thermal, plastic, and combined hygro-thermo-plastic deformation gradients respectively. It is assumed that all plastic deformation conserves volume, i.e. $det\mathbf{F}^p_A = 1$.

The rate kinematics are described by the velocity gradient $\mathbf{L} \equiv \dot{\mathbf{F}}\mathbf{F}^{-1}$ which can be decomposed into its elastic and inelastic components.

$$\mathbf{L}_A = \mathbf{L}^e_A + \mathbf{F}^e_A \left[\mathbf{L}^{sth}_A + \mathbf{F}^{sth}_A \mathbf{L}^p_A (\mathbf{F}^{sth}_A)^{-1}\right] (\mathbf{F}^e_A)^{-1} \tag{30}$$

where the elastic, hygro-thermal, and plastic velocity gradients are defined by equations 31, 32, and 33 respectively.

$$\mathbf{L}^e_A = \dot{\mathbf{F}}^e_A (\mathbf{F}^e_A)^{-1} \tag{31}$$

$$\mathbf{L}^{sth}_A = \dot{\mathbf{F}}^{sth}_A (\mathbf{F}^{sth}_A)^{-1} \tag{32}$$

$$\mathbf{L}^p_A = \dot{\mathbf{F}}^p_A (\mathbf{F}^p_A)^{-1} \tag{33}$$

The velocity gradient can also be decomposed as

$$\mathbf{L}_A = \mathbf{L}^e_A + \mathbf{F}^e_A \mathbf{L}^{sthp} (\mathbf{F}^e_A)^{-1} \tag{34}$$

where the definition of $\mathbf{L}_A^e$ remains the same and $\mathbf{L}^{sthp}$ is the combined hygro-thermo-plastic velocity gradient.

$$\mathbf{L}^{sthp} = \dot{\mathbf{F}}_A^{sthp} \left(\mathbf{F}_A^{sthp}\right)^{-1} = \mathbf{L}^{sth} + \mathbf{F}_A^{sth}\mathbf{L}_A^p \left(\mathbf{F}_A^{sth}\right)^{-1} \tag{35}$$

The hygro-thermo-plastic velocity gradient can be taken as the sum of the rate of stretching and the spin.

$$\mathbf{L}^{sthp} = \mathbf{D}_A^{sthp} + \mathbf{W}_A^{sthp} \tag{36}$$

where $\mathbf{D}_A^{sthp}$ (symmetric tensor) is the rate of hygro-thermo-plastic stretching and $\mathbf{W}_A^{sthp}$ is the hygro-thermo-plastic spin in the relaxed configuration. Without any loss of generality the hygro-thermo-plastic flow is taken to be irrotational, i.e. $\mathbf{W}_A^{sthp} = \mathbf{0}$. It then follows that

$$\dot{\mathbf{F}}_A^{sthp} = \mathbf{D}_A^{sthp}\mathbf{F}_A^{sthp} \tag{37}$$

In general the rate of hygro-thermo-plastic stretching is the sum of three contributions:

$$\mathbf{D}_A^{sthp} = \hat{\mathbf{D}}_A^p(\mathbf{T}_A, \theta, \mathbf{A}_i) + \hat{\mathbf{M}}_A(\theta, \mathbf{A}_i)\dot{\theta} + \hat{\mathbf{H}}_A(\varphi, \mathbf{A}_i)\dot{\varphi} \tag{38}$$

where $\mathbf{D}_A^p$, $\mathbf{M}_A$, and $\mathbf{H}_A$ capture the rate of plastic stretching, thermal stretching, and hygro stretching in the unloaded configuration, respectively, θ is the absolute temperature, φ is a measure of the water content, $\mathbf{T}_A$ is the driving stress, and $\mathbf{A}_i$ is a list of tensorial internal variables.

The rate of plastic stretching is itself the sum of two components:

$$\mathbf{D}^p = sym\left(\mathbf{F}_A^{sthp}\mathbf{L}^p(\mathbf{F}_A^{sthp})^{-1}\right) + sym\left(\frac{\partial\hat{\mathbf{F}}_A^{sthp}(\mathbf{T}_A, \theta, \varphi, \mathbf{A}_i)}{\partial\mathbf{A}_i}\mathbf{F}_A^{sthp}\right) \tag{39}$$

The first term is the symmetric part of the plastic gradient in the unloaded configuration, while the second term is the contribution of coupling accounting for any dependence of the hygro-thermal expansion on internal state (i.e. network orientation, dependence of hygro-expansion on temperature, dependence of thermal expansion on water content). The second and third terms in the rate of hygro-thermo-plastic stretching are the portions of the hygro-thermal velocity gradient which evolve with changing temperature and hydration respectively.

$$\hat{\mathbf{M}}_A\dot{\theta} = sym\left(\frac{\partial \mathbf{F}_A^{sthp}}{\partial \theta}\left(\mathbf{F}_A^{sthp}\right)^{-1}\right)\dot{\theta} \tag{40}$$

$$\hat{\mathbf{H}}_A\dot{\varphi} = sym\left(\frac{\partial \mathbf{F}_A^{sthp}}{\partial \varphi}\left(\mathbf{F}_A^{sthp}\right)^{-1}\right)\dot{\varphi} \tag{41}$$

In this model the hygro and thermal expansions were taken to be uncoupled with each other and with the deformation state. The coupling term in the plastic stretching tensor is dropped and it is defined identically to how it was defined in the elastic-plastic model.

$$\tilde{\mathbf{D}}_A^p = \dot{\gamma}_A^P \mathbf{N}_A^p \tag{42}$$

$$\mathbf{N}_A^p = \frac{\mathbf{T}'_A}{|\mathbf{T}'_A|} \tag{43}$$

$$\dot{\gamma}_A^P = \dot{\gamma}^o \exp\left[-\frac{\Delta G}{k_b\theta}\left(1 - \frac{\tau_A}{s + \alpha p}\right)\right] \tag{44}$$

Assuming a linear relation for both the thermal and hygro swelling, the rate of hygro-thermo-plastic stretching is then given as:

$$\mathbf{D}_A^{sthp} = \mathbf{F}_A^{e\,-1}\tilde{\mathbf{D}}_A^p\mathbf{F}_A^e + \alpha_\theta\frac{\partial \theta}{\partial t}\mathbf{I} + \beta_\varphi\frac{\partial \varphi}{\partial t}\mathbf{I} \tag{45}$$

where α_θ is the coefficient of thermal expansion and β_φ is the coefficient of hygro swelling.

Now that a rule has been established for updating the hygro-thermo-plastic deformation gradient the elastic deformation gradient can be obtained.

$$\mathbf{F}_A^e = \mathbf{F}_A(\mathbf{F}_A^{sthp})^{-1} \tag{46}$$

The second Piola-Kirchoff stress due to the intermolecular resistance, Cauchy stress due to the intermolecular resistance, and mechanical elastic Green-Lagrange strain are once again given by

$$\mathbf{S}_A = \left(2\mu\mathbf{E}^{e\prime} + \kappa(\mathrm{tr}\mathbf{E}^e)\mathbf{I}\right) \tag{47}$$

$$\mathbf{T}_A = \frac{1}{J}\mathbf{F}_A^e\mathbf{S}_A\mathbf{F}^{e\mathrm{T}} \tag{48}$$

$$\mathbf{E}^e = \frac{1}{2}\left(\mathbf{F}_A^{e\,\mathrm{T}}\mathbf{F}_A^e - \mathbf{I}\right) \tag{49}$$

where the mechanical elastic Green-Lagrange strain $\mathbf{E}^e$ appropriately no longer includes the hygro or thermally induced strains.

Hygro-thermal swelling also needs to be accounted for in the network mechanism. For the elastic-plastic model the network stress was defined as:

$$\mathbf{T}_B = \frac{1}{J}\mu_B\frac{\sqrt{N}}{\lambda_{chain}}\mathcal{L}^{-1}\frac{\lambda_{chain}}{\sqrt{N}}\mathbf{B}'_B \tag{50}$$

In a material which is initially at some reference temperature and water content for which the limiting chain extensibility $\sqrt{N}$ is determined, the chain stretch in the eight-chain network is defined as $\lambda_{chain} = \sqrt{\frac{\mathrm{tr}\mathbf{B}}{3.0}}$. However, this chain stretch will not account for a network which is initially swollen relative to the reference state. Therefore an effective chain stretch is used in place of the mechanical chain stretch where the effective chain stretch is given as the product of the stretch on the network from initial hygro swelling, initial thermal swelling, and the chain stretch as a function of the left Cauchy-Green tensor.

$$\lambda_{chainef} = \lambda_{chain}\lambda_{thermal}\lambda_{swelling} = \sqrt{\frac{\mathrm{tr}\mathbf{B}}{3.0}}\left(1+\alpha_\theta\left(\theta_{initial}-\theta_{ref}\right)\right)\left(1+\beta_\varphi\left(\varphi_{initial}-\varphi_{ref}\right)\right) \tag{51}$$

where the linear coefficients of thermal and hygro expansion (α_θ and β_φ) are defined to be the same as in the swelling calculation for the intermolecular mechanism.

Model Component	**Material Parameter**	**Value**
Elastic	μ	$3.33 \times 10^8 Pa$
	κ	$1.11 \times 10^8 Pa$
Plastic	$\dot{\gamma}^o$	$200 s^{-1}$
	ΔG	$9 \times 10^{-20} J$
	s	0.113μ
Network	μ_B	$1.95 \times 10^6 Pa$
	$\sqrt{N}$	2.5
Thermal	α_θ	$1.23 \times 10^{-4} K^{-1}$
Hygro	β_φ	$0.01\varphi^{-1}$

Table 3: Material properties for elastic-hygro-thermo-viscoplastic model.

Aside from the functional dependence of the the shear modulus and isotropic resistance to plasticity on temperature and hydration, two parameters are required to fit this model in addition to those needed for the elastic-plastic model: the thermal expansion coefficient and the hygro expansion coefficient. The former is taken from manufacturer information ($1.23 \times 10^{-4} K^{-1}$) while the latter is required by the definition of the water content as (1+swelling percentage relative to room temperature and relative humidity) to equal 0.01. The values of each of the material properties are listed in table 3.

The same experimental and simulation comparison that was made in figure 83 for the elastic-viscoplastic model is made for the elastic-hygro-thermo-viscoplastic model in figure 85. It can be seen that model is now effective at capturing the true stress-true strain dependence on temperature at low to moderate strains, however the simulation exhibits significantly more strain hardening at large strains than the experimental data as the temperature approaches the glass transition temperature. This same failure of the model is also evident in the stress relaxation behavior at elevated temperatures. As can be seen in figure 86, the model is able to capture stress relaxation at $25°C$ reasonably well for strains immediately post-yield and well into the strain hardening regime, however at $80°C$ the model greatly under predicts the magnitude of the stress relaxation for moderate strains.

The model is able to capture the effect of hydration (Figure 87) and the combined effect of temperature and hydration on the true stress-true strain behavior with the exception again of over predicting strain hardening at moderate strains and elevated temperatures which are all into the

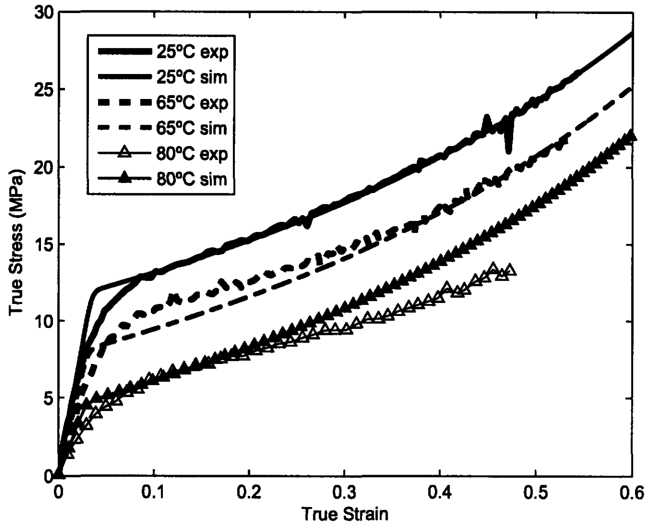

Figure 85: Thermal dependence of true stress-true strain behavior in uniaxial tension: simulation vs experiment for the elastic-hygro-thermo-plastic model.

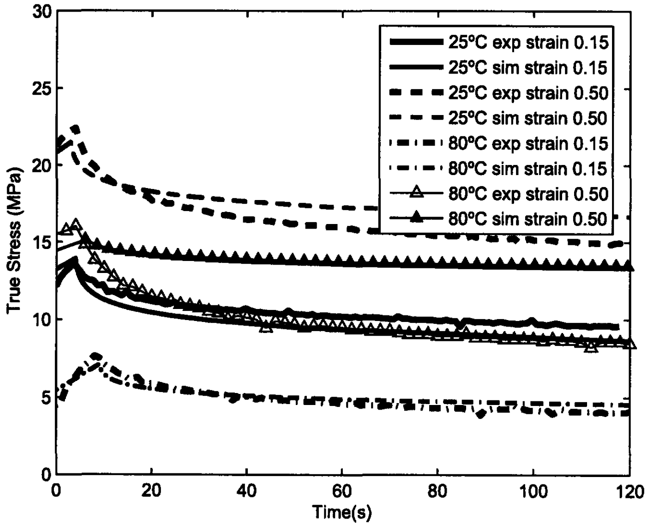

Figure 86: Thermal dependence of stress relaxation behavior in uniaxial tension: simulation vs experiment for the elastic-hygro-thermo-plastic model.

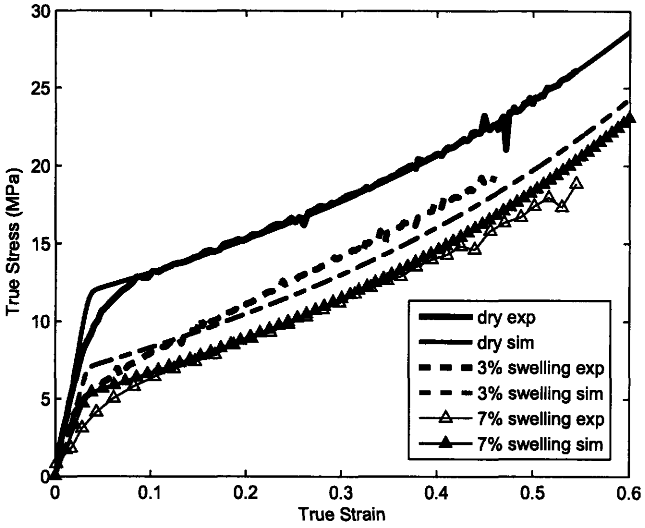

Figure 87: Hydration dependence of true stress-true strain behavior in uniaxial tension: simulation vs experiment for the elastic-hygro-thermo-plastic model.

leathery transition regime.

4.3.3 Model with Thermal Molecular Relaxation

The over prediction of strain hardening at elevated temperatures suggests the need for a thermally activated dissipative element in the network mechanism of the model. Reptation rather than shearing is the conceptual model for this dissipative element. Reptation is a process whereby polymer chains that are physically entangled rather than chemically cross-linked slip through one another decreasing the overall stress supported by the network. This mechanism was originally described mathematically in Doi and Edwards (1986) and applied to constitutive modeling by Bergström and Boyce (1998). If a free chain is within a network of chains it will deform affinely with that network as long as the deformation is performed at a high enough rate. Once the network is held at that deformation for an extended period of time, however, the free chain will gradually return to its elastically inactive state through Brownian motion. In a real network there do not have to be entire free chains, but free chain ends or segments can act to relieve the network stress in this same manner. The tube model, schematically depicted in figure 89, describes the dependence of creep rate on the average chain stretch. The chain segment is constrained to move only along

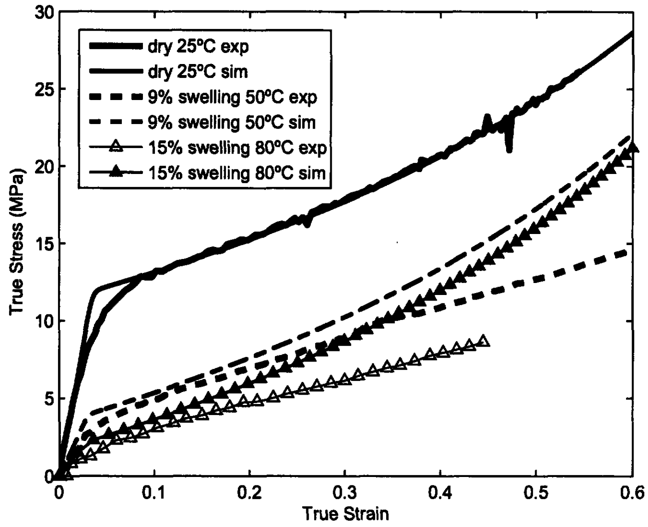

Figure 88: Combined hygro-thermal dependence of stress relaxation behavior in uniaxial tension: simulation vs experiment for the elastic-hygro-thermo-plastic model.

the tube, which it does by a combination of reptation motion and contour length fluctuations. A characteristic time for the chain to totally disengage from the tube can be calculated by dynamic analysis of the Rouse polymer model. This characteristic time is shown to be a function of the statistical nature of the network, the temperature, the friction constant, the number of polymer segments, and bond length. Reptation will therefore be a function of time, temperature, network orientation, and stress applied to the network, and have fitting parameters that are material specific. The orientation factor that has been chosen is the complement of the maximum angle in the eight-chain network. This parameter was shown by Dupaix and Boyce (2007) to accurately capture the network relaxation under multiple deformation modes.

The elastic-hygro-thermo-plastic model that includes thermal relaxation is shown rheologically in figure 90 where the network mechanism now consists of a non-linear spring and a thermally activated dissipative element.

Because there is now a dissipative element in the network, we have to redefine the network stress as a function only of the elastic part deformation gradient acting on mechanism B. The deformation gradient for the molecular network is decomposed into an elastic and a plastic contribution.

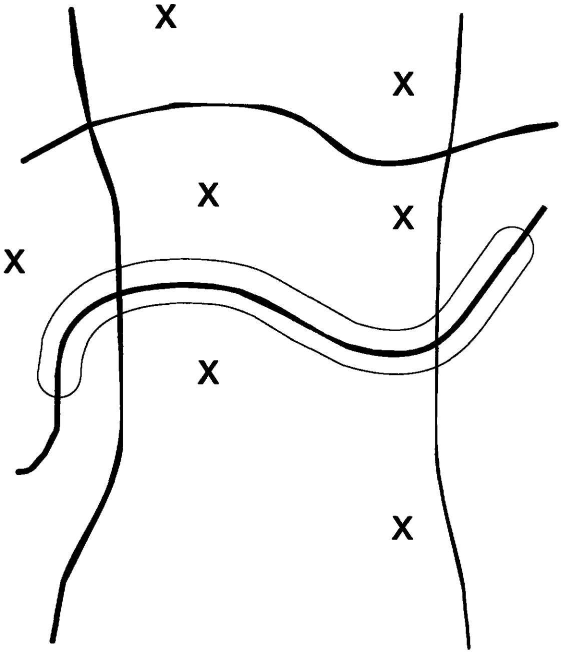

Figure 89: Doi and Edwards (1986) tube model for reptation of polymer chains in a network.

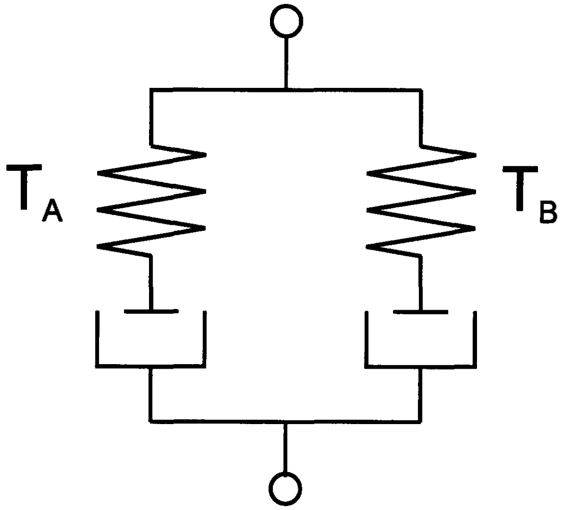

Figure 90: Schematic representation of the elastic-hygro-thermo-plastic model with thermally activated network relaxation.

$$\mathbf{F}_B = \mathbf{F}_B^e \mathbf{F}_B^p \tag{52}$$

where $\mathbf{F}_B^e$ is the elastic deformation gradient for mechanism B, and $\mathbf{F}_B^p$ is the plastic deformation gradient for mechanism B. The rate kinematics are described by the velocity gradient which can be decomposed into its elastic and plastic components.

$$\mathbf{L}_B = \dot{\mathbf{F}}\mathbf{F}^{-1} = \mathbf{L}_B^e + \mathbf{F}_B^e \mathbf{L}_B^p \mathbf{F}_A^{e\,-1} \tag{53}$$

The plastic velocity gradient can be given as

$$\mathbf{L}_B^p = \mathbf{D}_B^p + \mathbf{W}_B^p \tag{54}$$

where $\mathbf{D}_B^p$ (symmetric tensor) is the rate of plastic stretching in the relaxed configuration and $\mathbf{W}_B^p$ (skew tensor) is the plastic spin in the relaxed configuration. It then follows that

$$\dot{\mathbf{F}}_B^p = \mathbf{L}_B^p \mathbf{F}_B^p \tag{55}$$

providing an evolution equation for the plastic deformation gradient.

The rate of plastic stretching for the network in the loaded configuration is taken as the product of the scalar plastic strain rate $\dot{\gamma}_B^P$ and the direction tensor $\mathbf{N}_B^p$.

$$\tilde{\mathbf{D}}_B^p = \dot{\gamma}_B^P \mathbf{N}_B^p \tag{56}$$

The rate of plastic stretching for the network in the loaded configuration is then convected to the relaxed configuration ($\tilde{\mathbf{W}}_B^p = \mathbf{0}$).

$$\mathbf{L}_B^p = \mathbf{F}_B^{e\,-1} \tilde{\mathbf{D}}_B^p \mathbf{F}_B^e \tag{57}$$

The direction of plastic stretching is assumed to be coaxial with the deviatoric of the stress tensor acting on mechanism B.

$$\mathbf{N}^p_B = \frac{\mathbf{T}'_B}{|\mathbf{T}'_B|} \tag{58}$$

The magnitude of the plastic strain rate due to reptation is prescribed by

$$\dot{\gamma}^P_B = C\exp\left(-\frac{Q}{R\theta}\right)\left(\alpha_B\frac{\tau}{s}\right) \tag{59}$$

where C and $\frac{Q}{R}$ are material constants which capture the temperature dependence of reptation, and α_B is an orientation parameter equal to the complement of the maximum angle in the eight-chain system.

The elastic deformation gradient can then be obtained by:

$$\mathbf{F}^e_B = \mathbf{F}_B{\mathbf{F}^p_B}^{-1} \tag{60}$$

The stress due to the network resistance to deformation is again prescribed by the Arruda-Boyce eight-chain rubber elasticity model, only now $J = det\mathbf{F}^e_B$ is the *elastic* volume change; $\mathbf{B}'^e_B$ is the deviatoric part of the *elastic* left Cauchy-Green tensor ($\mathbf{B}^e_B = \mathbf{F}^e_B{\mathbf{F}^e_B}^{\mathsf{T}}$); and the mechanical chain stretch is defined in terms of the *elastic* left Cauchy-Green tensor ($\lambda_{chain} = \sqrt{\frac{\mathrm{tr}\mathbf{B}^e}{3.0}}$).

$$\mathbf{T}_B = \frac{1}{J}\mu_B\frac{\sqrt{N}}{\lambda_{chaintot}}\mathcal{L}^{-1}\frac{\lambda_{chaintot}}{\sqrt{N}}\mathbf{B}'^e_B \tag{61}$$

The effective chain stretch is defined as before as the product of the mechanical, thermal, and swelling chain stretches.

$$\lambda_{chainef} = \lambda_{chain}\lambda_{thermal}\lambda_{swelling} \tag{62}$$

There are no changes in the equations defining the intermolecular mechanism as a result of the addition of the dissipative element to the network mechanism.

Two additional parameters are required to fit this model: C and $\frac{Q}{R}$, the material constants which capture the temperature dependence of reptation. They are cooperatively determined from the shape of the true stress-true strain curve at large strains as the temperature and strain rate are

Model Component	**Material Parameter**	**Value**
Elastic	μ	$3.33 \times 10^8 Pa$
	κ	$1.11 \times 10^8 Pa$
Plastic	$\dot{\gamma}^o$	$200 s^{-1}$
	ΔG	$9 \times 10^{-20} J$
	s	0.113μ
Network	μ_B	$1.95 \times 10^6 Pa$
	$\sqrt{N}$	2.5
Molecular Relaxation	C	$5 \times 10^6 s^{-1}$
	$\frac{Q}{R}$	$7.2 \times 10^3 K$
	n	2.5
Thermal	α_θ	$1.23 \times 10^{-4} K^{-1}$
Hygro	β_φ	$0.01\varphi^{-1}$

Table 4: Fitting parameters for elastic-hygro-thermo-plastic model with thermally driven network relaxation.

varied. The values of each of the fitting parameters are listed in table 4.

The success of this model at capturing the reduction in strain hardening at elevated temperatures is shown in figures 91 and 92. The strain rate dependence is improved slightly as the slower rate tests are allowed more time for the network to relax at large strain (Figure 93). It also improves the accuracy of the stress-relaxation simulation (Figure 94).

One set of experimental data which we have not yet discussed with respect to the model is the cyclic data in which the material is uniaxially loaded and unloaded to increasing strains. A comparison between the model and experiments is shown in figure 95 below. When the material is unloaded from a strain of 0.2 there is a significant amount of recovery in the experimental data, however, the simulation unloads linearly, thereby exhibiting almost no recovery. The simulation also shows no recovery while the material is in a stress free state before it is reloaded, whereas the experiment shows significant recovery. The simulation fairs better when the material is loaded to a strain of 0.5. By this strain the network is making a significant contribution to the total stress, so it causes the simulation to unload non-linearly, but even here it under predicts the strain recovery at zero stress.

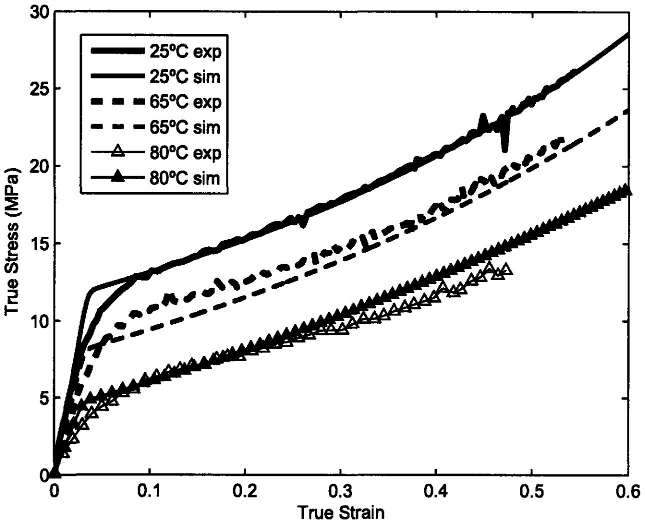

Figure 91: Thermal dependence of true stress-true strain behavior in uniaxial tension: simulation vs experiment for the elastic-hygro-thermo-plastic model with thermally activated network relaxation.

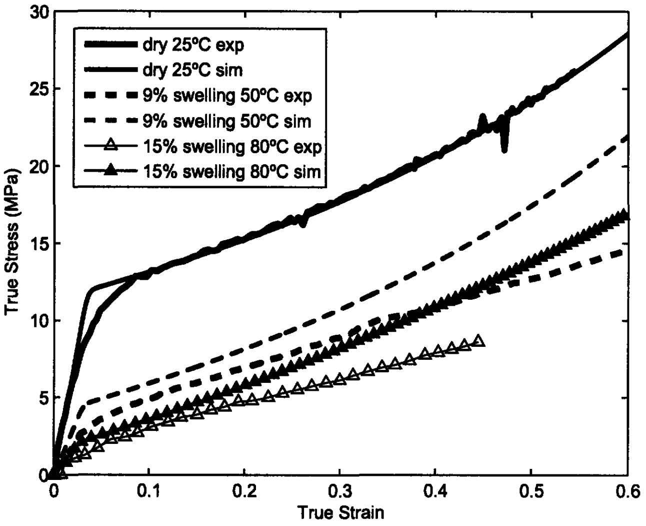

Figure 92: Combined hygro-thermal dependence of true stress-true strain behavior in uniaxial tension: simulation vs experiment for the elastic-hygro-thermo-plastic model with thermally activated network relaxation.

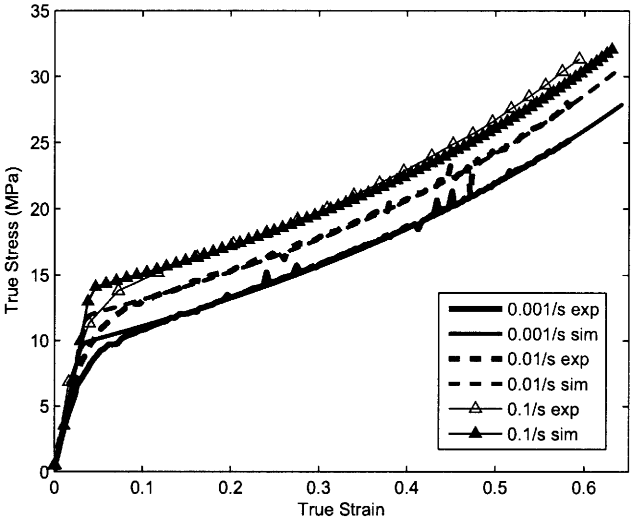

Figure 93: Strain rate dependence of true stress-true strain behavior in uniaxial tension: simulation vs experiment for the elastic-hygro-thermo-plastic model with thermally activated network relaxation.

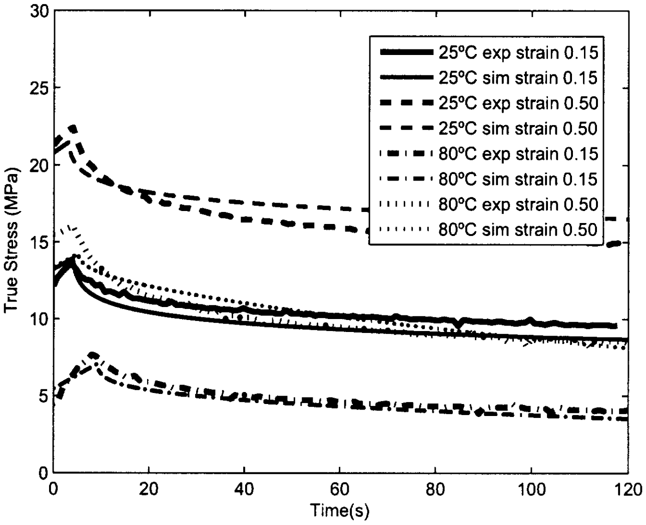

Figure 94: Thermal dependence of stress relaxation behavior in uniaxial tension: simulation vs experiment for the elastic-hygro-thermo-plastic model with thermally activated network relaxation.

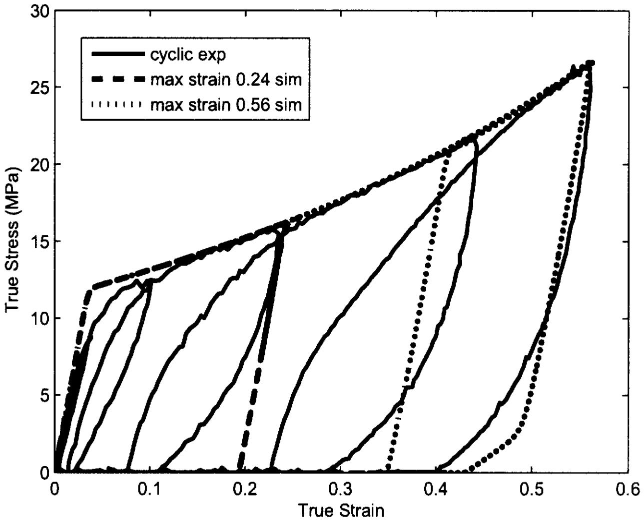

Figure 95: Nonlinear unloading and reloading true stress-true strain behavior under uniaxial tensile cyclic loading conditions: simulation vs experiment for the elastic-hygro-thermo-plastic model with thermally activated network relaxation .

4.3.4 Model with Back Stress

The large amount of non-linear strain recovery at small and moderate strains arises from the non-linear deformation of the ionic clusters. Since we have grouped the non-linear elastic behavior of the clusters with the linear elastic-plastic behavior of the backbone bundles, we must achieve this hysteretic non-linear recovery by undoing the plastic deformation that has occurred. We accomplish this by adding a back stress into the model as shown in figure 96. The forward viscoplastic dissipative element is still driven by the intermolecular force $\mathbf{T}_A$; the reverse viscoplastic dissipative element is driven by the difference between the intermolecular force $\mathbf{T}_A$ and the back stress $\mathbf{T}_C$.

The total stress acting on the system is still equal to the sum of the stress contributions from the intermolecular and network mechanisms.

$$\mathbf{T} = \mathbf{T}_A + \mathbf{T}_B \tag{63}$$

The plastic stretching in the loaded configuration is now given as the sum of the forward and reverse plastic processes:

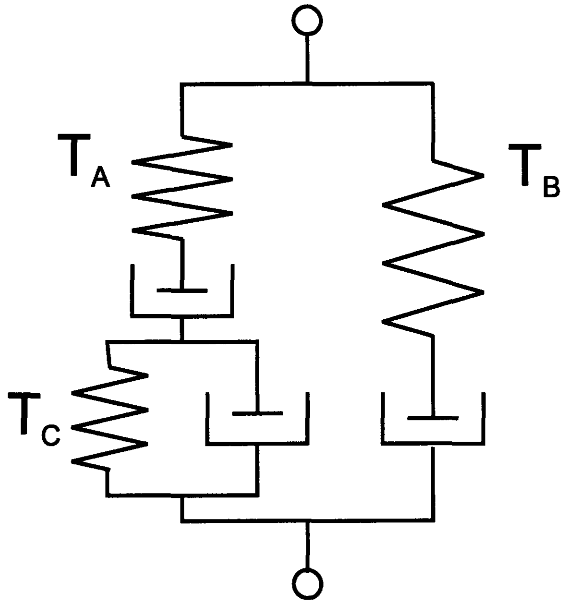

Figure 96: Schematic representation of the elastic-hygro-thermo-plastic model with thermally activated network relaxation and a back stress driving intermolecular recovery.

$$\tilde{\mathbf{D}}^p_A = \dot{\gamma}^P_{Af}\mathbf{N}^p_{Af} + \dot{\gamma}^P_{Ab}\mathbf{N}^p_{Ab} \tag{64}$$

where the direction $\mathbf{N}^p_{Af}$ and $\mathbf{N}^p_{Ab}$ are taken to be coaxial with the deviatoric portion of the forward and backward stress tensors respectively.

$$\mathbf{N}^p_{Af} = \frac{\mathbf{T}'_{Af}}{|\mathbf{T}'_{Af}|} \tag{65}$$

$$\mathbf{N}^p_{Ab} = \frac{\mathbf{T}'_{Ab}}{|\mathbf{T}'_{Ab}|} \tag{66}$$

where $\mathbf{T}_{Af}$ is the net forward driving stress defined by $\mathbf{T}_{Af} = \mathbf{T}_A$ and $\mathbf{T}_{Ab}$ is the net backward driving stress defined by $\mathbf{T}_{Ab} = \mathbf{T}_A - \mathbf{T}_C$ where $\mathbf{T}_C$ is the back stress.

The magnitude of the forward and backwards plastic strain rates $\dot{\gamma}^P_{Af}$ and $\dot{\gamma}^P_{Ab}$ are prescribed by

$$\dot{\gamma}^{P}_{Af} = \dot{\gamma}^{o} \exp\left[-\frac{\Delta G}{k_b \theta}\left(1 - \frac{\tau_{Af}}{s_f + \alpha p}\right)\right] \tag{67}$$

$$\dot{\gamma}^{P}_{Ab} = \dot{\gamma}^{o} \exp\left[-\frac{\Delta G}{k_b \theta}\left(1 - \frac{\tau_{Ab}}{s_b + \alpha p}\right)\right] \tag{68}$$

where $\dot{\gamma}^{o}$ is a material constant; ΔG is the activation energy; $\tau_{Ai} = \sqrt{\frac{1}{2}\mathbf{T}'_{Ai}\mathbf{T}'_{Ai}}$ is the equivalent shear stress; s_i is the shear resistance; α is the pressure coefficient; and p is the pressure (i=f,b).

The back stress must be constitutively prescribed. Here it was chosen to evolve with $\mathbf{T}_A$ and a network orientation factor during loading as given by equation 69, and to maintain its value during unloading. It evolves with the intermolecular stress $\mathbf{T}_A$ because the energy stored in the ionic clusters by that stress will be the same energy used to try to return to material to its original state, however as the orientation increases the backbone segments shear away for their original ion clusters thereby decreasing the stored energy (hence the proportionality to an orientation factor that decreases with increasing orientation).

$$\mathbf{T}_C = \mathbf{T}_A \left(\frac{\alpha_B}{\alpha_B^o}\right)^n \tag{69}$$

where α_B, the same orientation parameter as used for network reptation, is equal to the complement of the maximum angle in the eight-chain system, α_B^o is the value of α_B in the undeformed state, and n is a fitting parameter to account for the non-linear reduction in the back stress with increasing strain.

Nothing in the network mechanism is changed from the previous version of the model.

Two additional parameters are required to fit this model: the isotropic resistance to reverse plasticity s_b which is defined as a fraction of s_f and n. The values of each of the fitting parameters are listed in table 5.

The simulation is shown versus the experiment under cyclic loading conditions at a strain rate of $0.01/s$ in figure 97. With the back stress added, the model does a much better job of capturing the non-linear recovery at small to moderate strains as well as the additional strain recovery during the time period for which there is no applied stress. It does over predict the recovery for large

Model Component	**Material Parameter**	**Value**
Elastic	μ	$3.33 \times 10^8 Pa$
	κ	$1.11 \times 10^8 Pa$
Plastic	$\dot{\gamma}^o$	$200 s^{-1}$
	ΔG	$9 \times 10^{-20} J$
	s	0.113μ
	s_b	$0.84 s_f$
Network	μ_B	$1.95 \times 10^6 Pa$
	$\sqrt{N}$	2.5
Molecular Relaxation	C	$5 \times 10^6 s^{-1}$
	$\frac{Q}{R}$	$7.2 \times 10^3 K$
	n	2.5
Thermal	α_θ	$1.23 \times 10^{-4} K^{-1}$
Hygro	β_φ	$0.01 \varphi^{-1}$

Table 5: Fitting parameters for elastic-hygro-thermo-plastic model with network relaxation and a back stress driving intermolecular recovery.

strains, however this is the region that is of less interest for modeling of a fuel cell unit as strains in the unit are expected to be small, no more than 0.3 to 0.4 (an assumption that will be validated in chapter 5).

Unfortunately the model does not do a very good job at capturing the lack of strain rate dependence of the non-linear recovery as is evident in figure 98. In the experimental data the strain is roughly the same for all three states at the zero stress point for loading and again for reloading. The simulation slightly under predicts the strain recovery during unloading and predicts no recovery in the time between unloading and reloading for the fastest strain rate.

The addition of the back stress has no noticeable effect on the simulated stress relaxation behavior. This makes sense since the reverse plasticity only becomes significant when the back stress is larger than the intermolecular stress, and the intermolecular stress does not relax enough during a stress relaxation tests for this to occur (Figure 99).

4.3.5 Model with Evolving Isotropic Resistance to Plasticity

There is still one easily addressed feature which is clearly missing from this model that may be important to modeling the material behavior at small strains; that is the lack of rollover in the yield behavior (visible in every true stress-true strain curve shown so far). In order to capture the

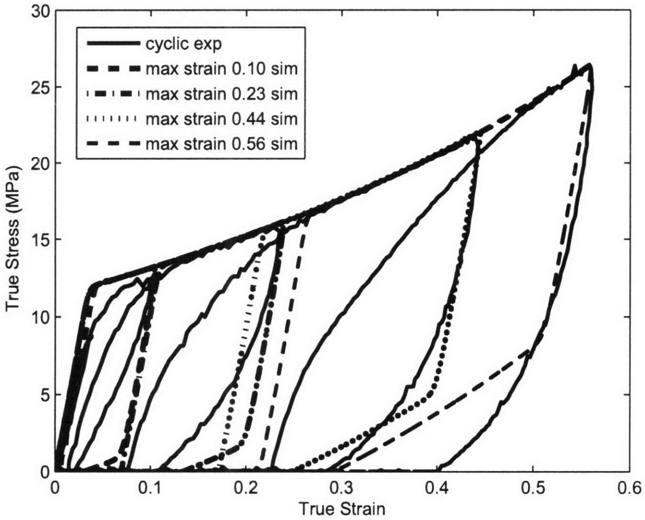

Figure 97: Nonlinear unloading and reloading true stress-true strain behavior under uniaxial tensile cyclic loading conditions: simulation vs experiment for the elastic-hygro-thermo-plastic model with network relaxation and a back stress driving intermolecular recovery.

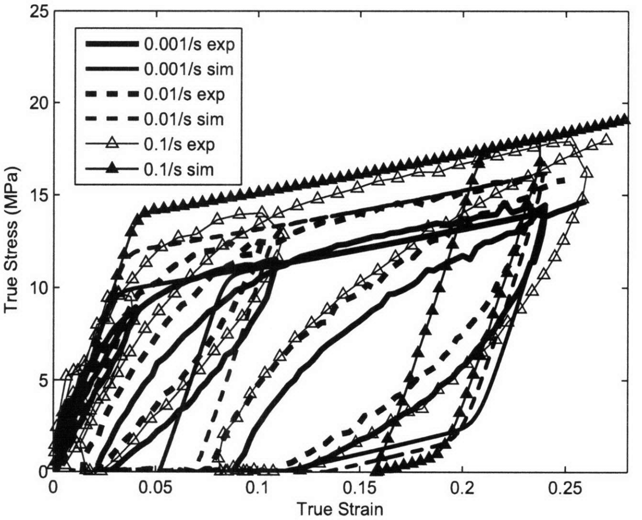

Figure 98: Strain rate dependence of nonlinear unloading and reloading true stress-true strain behavior under uniaxial tensile cyclic loading conditions: simulation vs experiment for the elastic-hygro-thermo-plastic model with network relaxation and a back stress driving intermolecular recovery.

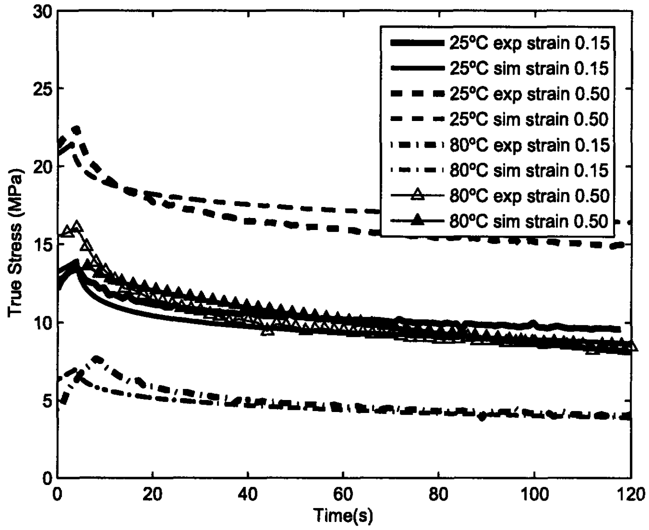

Figure 99: Thermal dependence of stress relaxation behavior in uniaxial tension: simulation vs experiment for the elastic-hygro-thermo-plastic model with network relaxation and a back stress driving intermolecular recovery.

rollover yielding behavior an evolving isotropic resistance to plasticity, or "s", is needed.

In Nafion there are two cooperative mechanisms which lead to the appearance of a roll-over yield behavior. The first is the non-linear elastic deformation of the ionic clusters as they are transformed from circular to elliptical cross-sections changing the energetic interactions among the negatively charge sulfuric ions. Superimposed on this is the yielding behavior of the backbone regions; in the undeformed state the backbone bundles are unaligned, they must overcome an energy barrier to shear and rotate against interactions with neighboring bundles and ionic domains to an alignment at which they become easier to align within each bundle. Of course not all the bundles align at the same applied stress. There is a spatial distribution in free volume and the strength of interactions with neighboring domains which corresponds to a distribution of sites that can be plastically deformed at a distribution of stresses. At a critical stress the site with the least resistance to shear will begin to deform plastically, however the rest of the material will continue to deform elastically. As more sites reach their respective critical stress states the macroscopic material behavior will roll over from elastic to plastic behavior. As was explained earlier, those two phenomena have been combined into a single "intermolecular" mechanism. Rheologically the

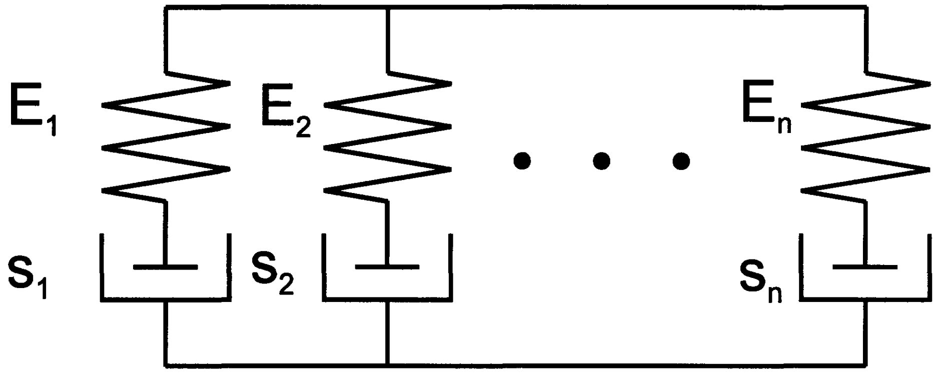

Figure 100: Rheological representation of a material with a distribution of shearing resistances.

Mechanism Number	**Elastic Modulus (Pa)**	$s(Pa)$
1	2.25×10^7	6.30×10^7
2	2.25×10^7	3.83×10^7
3	4.50×10^7	4.95×10^6
4	2.10×10^8	1.47×10^8
Evolving s		
	s_{min}	$8.88 \times 10^6 Pa$
	s_{max}	$1.22 \times 10^7 Pa$
	μ	80

Table 6: Parameters for multiple mechanism yielding comparison to evolving shear resistance yielding.

distributed shearing can be thought of as an infinite number of elastic-plastic mechanisms with distributed elastic moduli and shear resistances, acting in parallel (here, we approximate as "in parallel" but the structure is heterogenously distributed as shown in figure 100.

From a practical implementation standpoint, it is much simpler to model this effect as an evolution in s. The mathematical equivalence of these two approaches is shown in figure 101 below in which the stress-strain response of four elastic-plastic mechanisms with properties as listed in table 6 is compared with the stress-strain response of a single elastic-plastic mechanism with an "s" that evolves from a minimum to a maximum value with plastic deformation. The evolving "s" concept has the advantage that it can easily be combined with the apparent yielding associated with the non-linear elasticity of the clusters.

When the load is removed from the material the ionic clusters undergo a partial recovery,

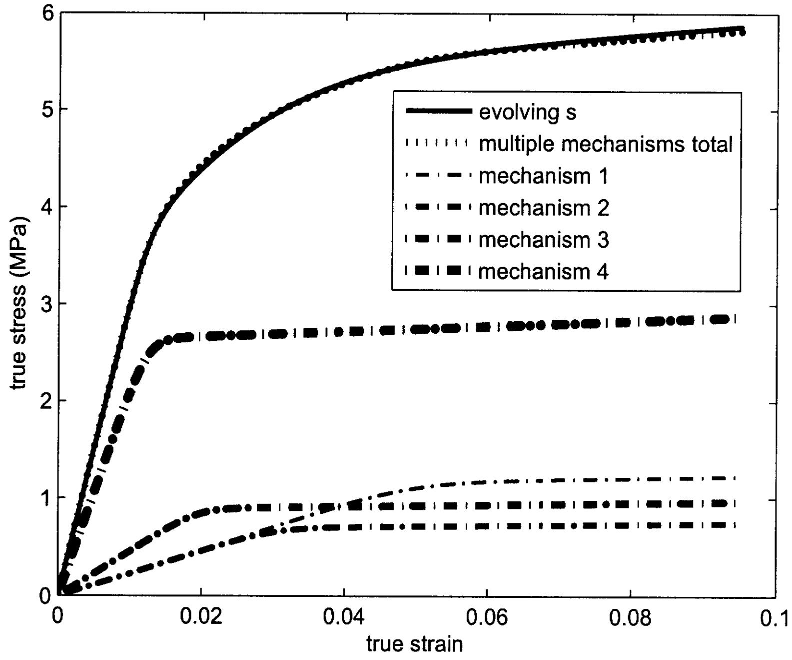

Figure 101: Comparison of tensile yielding behavior of a material with an evolving "s" versus one composed of four yielding mechanisms with distributed "s" values acting in parallel.

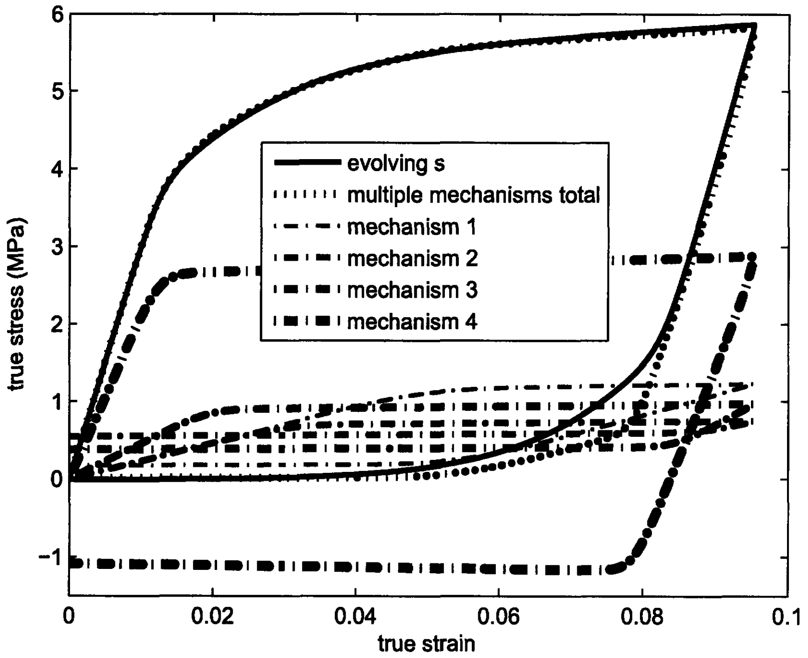

Figure 102: Comparison of tensile unloading behavior of a material with an evolving "s" versus one composed of four yielding mechanisms with distributed "s" values acting in parallel all of which have applied back stresses.

the degree of which depends on the maximum strain that was reached. The recovering clusters drag the backbone bundles that are associated with them back to a less oriented state, however, just like for loading, there is a non-spatially uniform energy barrier associated with this backbone motion. Similarly to the forward "s", the backwards resistance can be modeled as evolving from a minimum to a maximum with plastic recovery. This is compared to the response of a material with four yielding mechanisms with back stresses as shown in figure 102. While the unloading curves do not match exactly they show the same general behavior. The unloading and reloading mechanisms are not identical to the initial loading mechanism (as evidenced by the difference in the shape of each in the stress-strain curve), but they are similar enough that they can be modeled by the same governing equations.

All of the kinematic and constitutive equations remain the same, however now the forward and reverse isotropic resistances to plasticity evolve. The evolution equations are as follows:

During loading:

$$\dot{s}_f = \mu_{sf}(s_{fmax} - s_f)\dot{\gamma}_f^P \tag{70}$$

$$\dot{s}_b = \mu_{sb}(s_{bmin} - s_b)\dot{\gamma}_f^P \tag{71}$$

During unloading:

$$\dot{s}_f = \mu_{sf}(s_{fmin} - s_f)\dot{\gamma}_b^P \tag{72}$$

$$\dot{s}_b = \mu_{sb}(s_{bmax} - s_b)\dot{\gamma}_b^P \tag{73}$$

where s_{imax} is the maximum shear resistance value of component i and s_{imin} is the minimum shear resistance value of component i $(i = f, b)$. $\dot{s}_{fo}$ and $\dot{s}_{bo}$ the initial values of the shear resistances are set equal to the minimum value and defined as a fraction of the shear modulus.

Two additional parameters are needed to fit the rollover yield. They are the minimum/initial value of the isotropic resistance to forward plastic deformation s_{fmin}, and μ_{sf} the coefficient which controls the rate of change of the isotropic resistance to forward plastic deformation; these parameters are determined by stress at which the rollover yield begins and the shape of the rollover yield respectively. The maximum value of the isotropic resistance to forward plastic deformation s_{fmax} is set to the previous non-evolving value of s_f; s_{bmax} and s_{bmin} are defined as the same fraction of s_{fmax} and s_{fmin} respectively, as s_b was in the previous model; the rate of change of the isotropic resistance to backward plastic deformation is assumed to equal the rate of change of the isotropic resistance to forward plastic deformation (i.e. μ_{sb}=μ_{sf}). The values of each of the fitting parameters are listed in table 7.

It can be seen that the model now captures the rollover type yield behavior for different strain rates, temperature, and hydrations (Figures 103-106). It does develop an artificially large reduction in strain hardening at strains over roughly 0.4 depending on the specific loading conditions. This arises from the form of the equation used for the back stress and the small value of the isotropic

Model Component	**Material Parameter**	**Value**
Elastic	μ	$3.33 \times 10^8 Pa$
	κ	$1.11 \times 10^8 Pa$
Plastic	$\dot{\gamma}^o$	$200 s^{-1}$
	ΔG	$9 \times 10^{-20} J$
	s_{fmin}	0.08μ
	s_{fmax}	0.113μ
	$s_{bmin,max}$	$0.86 s_{fmin,max}$
	μ_{si}	80
Network	μ_B	$1.95 \times 10^6 Pa$
	$\sqrt{N}$	2.5
Molecular Relaxation	C	$5 \times 10^6 s^{-1}$
	$\frac{Q}{R}$	$7.2 \times 10^3 K$
	n	2.5
Thermal	α_θ	$1.23 \times 10^{-4} K^{-1}$
Hygro	β_φ	$0.01 \varphi^{-1}$

Table 7: Fitting parameters for elastic-hygro-thermo-plastic model with network relaxation, a back stress driving intermolecular recovery, and evolving forward and reverse resistances to plasticity.

resistance to reverse plasticity relative to the isotropic resistance to forward plasticity. Since this is a problem only at large strains, it was chosen to leave it rather than add more parameters to the model.

As can be seen in figures 103-111 all the features that have been identified as important for the membrane in a fuel cell environment are captured by the model. These include the strain rate dependence of yield; the gradual transition from linear-elastic to viscoplastic deformation; the dependence of the elastic modulus, yield stress, post-yield behavior, and stress relaxation on temperature and hydration (Figures 104 - 106 and 110-111); the non-linear viscoplastic recovery during cyclic loading (Figures 107 ,108) ; and the evolution of the stress relaxation behavior as strain is increased (Figures 109 - 111). There does appear to be too much rate dependency of moderate strain viscoelastic recovery during cyclic loading, this arises because at faster rates the back stress does not have enough time to drive strain recovery before reloading beings. The model also fails to capture the increase in stress relaxation as the strain increases from moderate to large strains. In the following chapter each of the above versions of the model will be evaluated in a simulated fuel cell.

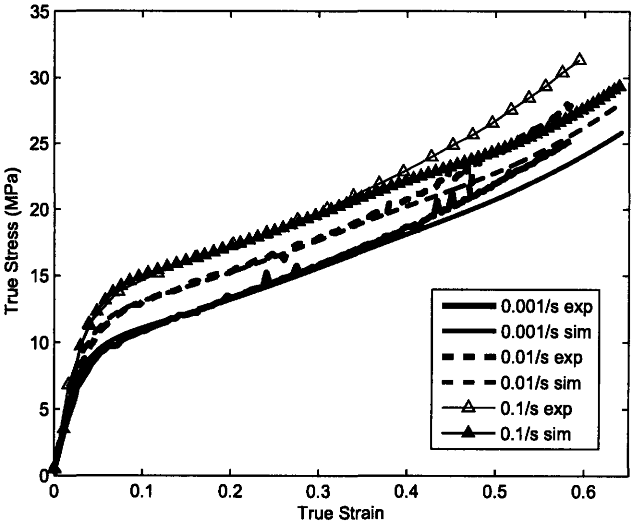

Figure 103: Strain rate dependence of true stress-true strain behavior in uniaxial tension: simulation vs experiment for the elastic-hygro-thermo-plastic model with network relaxation, a back stress driving intermolecular recovery, and evolving forward and reverse resistances to plasticity.

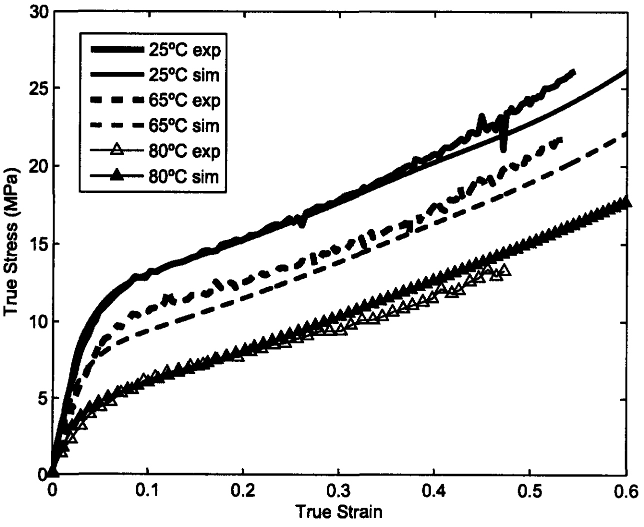

Figure 104: Thermal dependence of true stress-true strain behavior in uniaxial tension: simulation vs experiment for the elastic-hygro-thermo-plastic model with network relaxation, a back stress driving intermolecular recovery, and evolving forward and reverse resistances to plasticity.

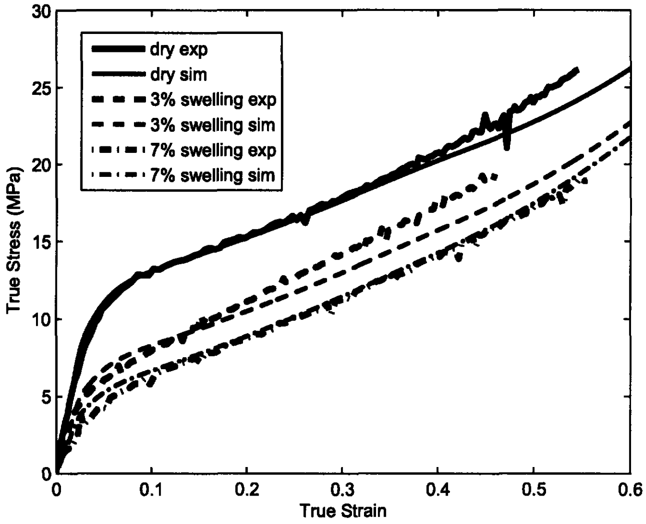

Figure 105: Hydration dependence of true stress-true strain behavior in uniaxial tension: simulation vs experiment for the elastic-hygro-thermo-plastic model with network relaxation, a back stress driving intermolecular recovery, and evolving forward and reverse resistances to plasticity.

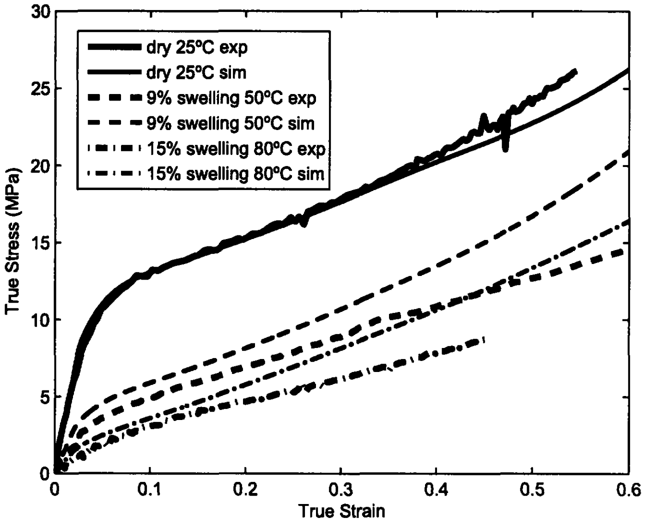

Figure 106: Combined thermal and hydration dependence of true stress-true strain behavior in uniaxial tension: simulation vs experiment for the elastic-hygro-thermo-plastic model with network relaxation, a back stress driving intermolecular recovery, and evolving forward and reverse resistances to plasticity.

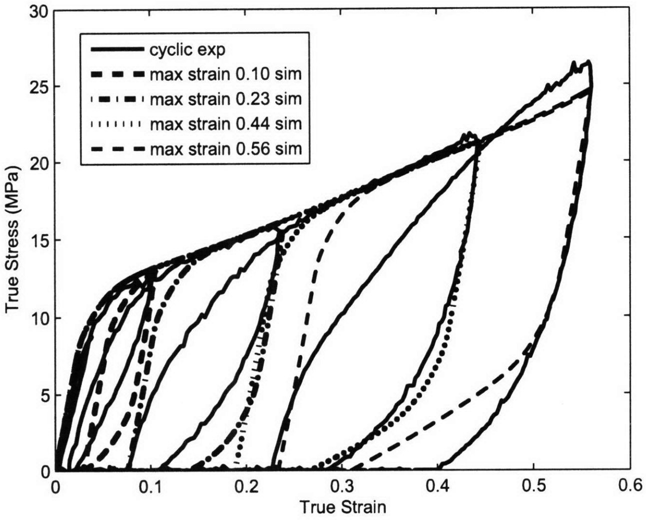

Figure 107: Nonlinear unloading and reloading true stress-true strain behavior under uniaxial tensile cyclic loading conditions: simulation vs experiment for the elastic-hygro-thermo-plastic model with network relaxation, a back stress driving intermolecular recovery, and evolving forward and reverse resistances to plasticity.

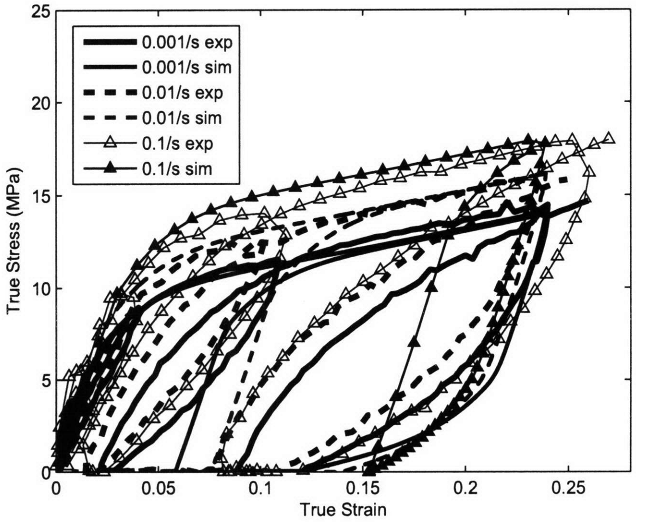

Figure 108: Rate dependence of the nonlinear unloading and reloading true stress-true strain behavior under uniaxial tensile cyclic loading conditions: simulation vs experiment for the elastic-hygro-thermo-plastic model with network relaxation, a back stress driving intermolecular recovery, and evolving forward and reverse resistances to plasticity.

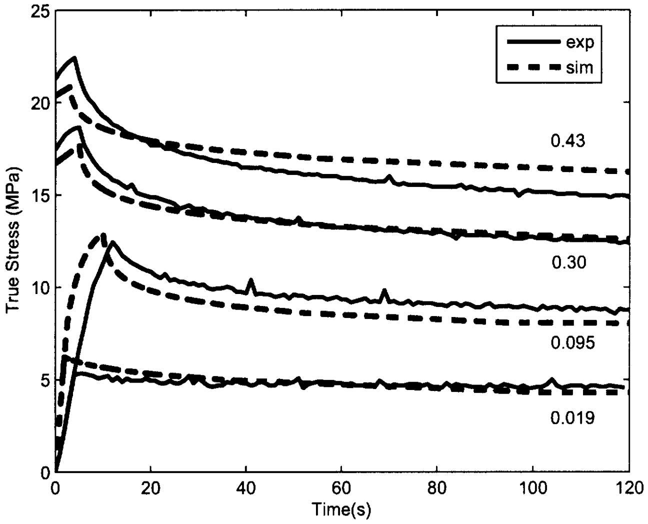

Figure 109: Strain dependence of stress relaxation behavior in uniaxial tension at 25^oC: simulation vs experiment for the elastic-hygro-thermo-plastic model with network relaxation, a back stress driving intermolecular recovery, and evolving forward and reverse resistances to plasticity.

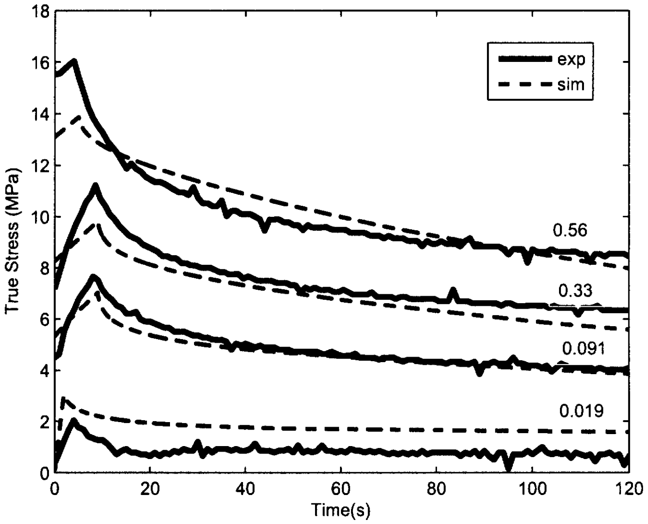

Figure 110: Strain dependence of stress relaxation behavior in uniaxial tension at 80^oC: simulation vs experiment for the elastic-hygro-thermo-plastic model with network relaxation, a back stress driving intermolecular recovery, and evolving forward and reverse resistances to plasticity.

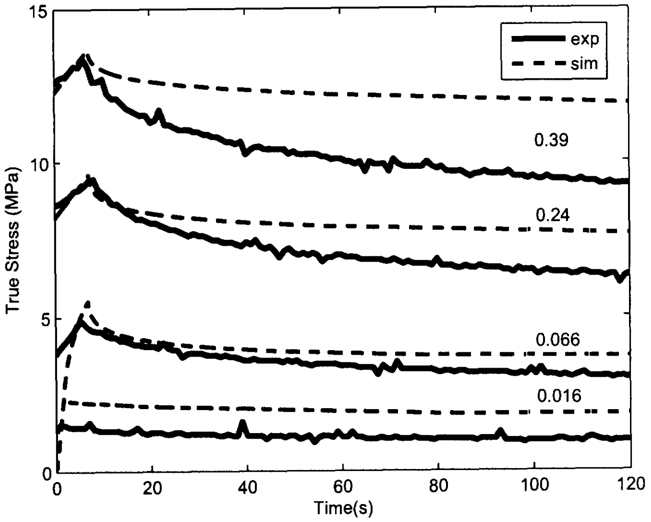

Figure 111: Strain dependence of stress relaxation behavior in uniaxial tension while immersed in water at 25^oC: simulation vs experiment for the elastic-hygro-thermo-plastic model with network relaxation, a back stress driving intermolecular recovery, and evolving forward and reverse resistances to plasticity.

4.3.6 Model Summary

$$\mathbf{F} = \mathbf{F}_A = \mathbf{F}_B$$

$$\mathbf{T} = \mathbf{T}_A + \mathbf{T}_B$$

Mechanism A:

$$\mathbf{F}_A = \mathbf{F}^e_A \mathbf{F}^{sthp}_A$$

$$\mathbf{L}_A = \dot{\mathbf{F}}_A (\mathbf{F}_A)^{-1}$$

$$\mathbf{L}_A = \mathbf{L}^e_A + \mathbf{F}^e_A \mathbf{L}^{sthp} (\mathbf{F}^e_A)^{-1}$$

$$\mathbf{L}^{sthp} = \dot{\mathbf{F}}^{sthp}_A \left(\mathbf{F}^{sthp}_A\right)^{-1} = \mathbf{L}^{sth} + \mathbf{F}^{sth}_A \mathbf{L}^p_A \left(\mathbf{F}^{sth}_A\right)^{-1}$$

$$\mathbf{L}^{sthp} = \mathbf{D}^{sthp}_A + \mathbf{W}^{sthp}_A$$

$$\dot{\mathbf{F}}^{sthp}_A = \mathbf{L}^{sthp}_A \mathbf{F}^{sthp}_A$$

$$\mathbf{L}^{sthp}_A = \mathbf{F}^{e}_A{}^{-1} \tilde{\mathbf{D}}^p \mathbf{F}^e_A + \alpha_\theta \tfrac{\partial \theta}{\partial t} \mathbf{I} + \beta_\varphi \tfrac{\partial \varphi}{\partial t} \mathbf{I}$$

$$\tilde{\mathbf{D}}^p_A = \dot{\gamma}^P_{Af} \mathbf{N}^p_{Af} + \dot{\gamma}^P_{Ab} \mathbf{N}^p_{Ab}$$

$$\mathbf{N}^p_{Af} = \frac{\mathbf{T}'_{Af}}{|\mathbf{T}'_{Af}|}$$

$$\mathbf{N}^{p}_{Ab} = \frac{\mathbf{T}'_{Ab}}{\left|\mathbf{T}'_{Ab}\right|}$$

$$\dot{\gamma}^{P}_{Af} = \dot{\gamma}^{o} \exp\left[-\tfrac{\Delta G}{k_b \theta}\left(1 - \tfrac{\tau_{Af}}{s_f + \alpha p}\right)\right]$$

$$\dot{\gamma}^{P}_{Ab} = \dot{\gamma}^{o} \exp\left[-\tfrac{\Delta G}{k_b \theta}\left(1 - \tfrac{\tau_{Ab}}{s_b + \alpha p}\right)\right]$$

$$\mathbf{S}_A = (2\mu \mathbf{E}^{e\prime} + \kappa(\mathrm{tr}\mathbf{E}^{e})\mathbf{I})$$

$$\mathbf{T}_A = \tfrac{1}{J}\mathbf{F}^{e}_{A}\mathbf{S}_A\mathbf{F}^{e\top}$$

$$\mathbf{T}_C = \mathbf{T}_A\left(\tfrac{\alpha_B}{\alpha^{o}_{B}}\right)^{n}$$

$$\mathbf{E}^{e} = \tfrac{1}{2}\left(\mathbf{F}^{e\,\top}_{A}\mathbf{F}^{e}_{A} - \mathbf{I}\right)$$

Mechanism B:

$$\mathbf{F}_B = \mathbf{F}^{e}_{B}\mathbf{F}^{p}_{B}$$

$$\mathbf{L}_B = \dot{\mathbf{F}}_B(\mathbf{F}_B)^{-1}$$

$$\dot{\mathbf{F}}^{p}_{B} = \mathbf{D}^{p}_{B}\mathbf{F}^{p}_{B}$$

$$\tilde{\mathbf{D}}^{p}_{B} = \dot{\gamma}^{P}_{B}\mathbf{N}^{p}_{B}$$

$$\mathbf{L}^{p}_{B} = \mathbf{F}^{e\,-1}_{B}\tilde{\mathbf{D}}^{p}_{B}\mathbf{F}^{e}_{B}$$

$$\dot{\gamma}^{P}_{B} = C \exp\left(-\tfrac{Q}{R\theta}\right)\left(\alpha_B \tfrac{\tau}{s}\right)$$

$$\mathbf{N}^{p}_{B} = \frac{\mathbf{T}'_{B}}{|\mathbf{T}'_{B}|}$$

$$\mathbf{T}_B = \tfrac{1}{J}\mu_B \tfrac{\sqrt{N}}{\lambda_{chaintot}}\mathcal{L}^{-1}\tfrac{\lambda_{chaintot}}{\sqrt{N}}\mathbf{B}'^{e}_{B}$$

$$\mathbf{B}^{e}_{B} = \mathbf{F}^{e}_{B}\mathbf{F}^{e\,\top}_{B}$$

$$\lambda_{chainef} = \lambda_{chain}\lambda_{thermal}\lambda_{swelling} = \sqrt{\tfrac{\mathrm{tr}\mathbf{B}^{e}}{3.0}}\left(1 + \alpha_\theta\left(\theta_{initial} - \theta_{ref}\right)\right)\left(1 + \beta_\varphi\left(\varphi_{initial} - \varphi_{ref}\right)\right)$$

$$\lambda_{chain} = \sqrt{\tfrac{\mathrm{tr}\mathbf{B}^{e}}{3.0}}$$

Kinematic assumptions:

$$\tilde{\mathbf{W}}^{sthp}_{A} = \mathbf{0}$$

$$\tilde{\mathbf{W}}^{p}_{B} = \mathbf{0}$$

Material Properties:

$\mu(\Theta, \varphi)$;$\kappa(\Theta, \varphi)$

μ_B; $\sqrt{N}$

$\dot{\gamma}^{o}$; ΔG

α; μ_s

s_{fmin}; s_{fmax}; c_2

s_{bmin}; s_{bmax}; c_3

c_1; n

α_θ; β_φ

As is evident in figures 103 through 111, the model is successful in capturing the highly non-linear elastic-hygro-thermo-viscoplastic mechanical behavior of Nafion. In the following chapter the model is applied in a simulated fuel cell environment and subjected to hygro-thermal cycling. The results will be used to evaluate whether the hypothesis that permanent deformation arises due to the mechanical effects of hygro-thermal cycling in the constrained fuel cell environment. The simulation will also be used to evaluate whether the fully developed model is needed or if a simpler version will suffice.

5 Model Application

5.1 Simulation Methods

As a first go at applying the material model developed above to a "real" fuel cell setup we decided to take the fuel cell unit identified by the Karlsson research group (Tang, Santare et. al. 2006 and Kusolgu et. al. 2006). This configuration is shown again in figure 112. A fuel cell stack consists of bipolar plates alternating with membrane electrode assemblies (MEA). The bipolar plates have channels machined into them for the distribution of the hydrogen and oxygen to the anode and cathode respectively and also serve to collect current from the MEA between them. The plates are $11mm$ thick with grooves that are $1mm$ in both depth and width. Graphite ($E = 10GPA$, $\nu = 0.25$) was chosen as the bipolar plate material for this simulation, although steel is another common option. The MEA consists of the polymer electrolyte membrane (PEM), in this case Nafion, with a thin platinum based catalyst layer on each side, and gas diffusion layers (GDL) bonded to the outside of the catalyst layers. The Nafion was taken to be $20\mu m$ thick and the catalyst layer was grouped with the GDL to form a gas diffusion electrode (GDE) $100\mu m$ thick. The GDE taken to have GDL properties, specifically it is given the mechanical properties of Toray TGPH-60 carbon paper ($E = 20MPa$, $\nu = 0.25$) (Gasteiger and Mathias (2003)).

The simulation was run for the the final version of the model as well as for the simplest version of the model that includes hydration and thermal effects (elastic-hygro-thermo-viscoplastic). They were each run for both the aligned and unaligned cases as these were shown by Karlsson's group to have significantly different behavior. The boundary conditions are as follows:

1) The top of the top bipolar plate and the bottom of the bottom bipolar plate are constrained in the vertical direction.

2) Friction free contact is defined between the bipolar plates and the gas diffusion layers.

3) The membrane is bonded to the gas diffusion layers (i.e. the nodes on the membrane are tied to those at the same location on the GDE).

4) The left sides of all components are fixed in the horizontal direction.

5) The right sides of all components are fixed to move together in the horizontal direction.

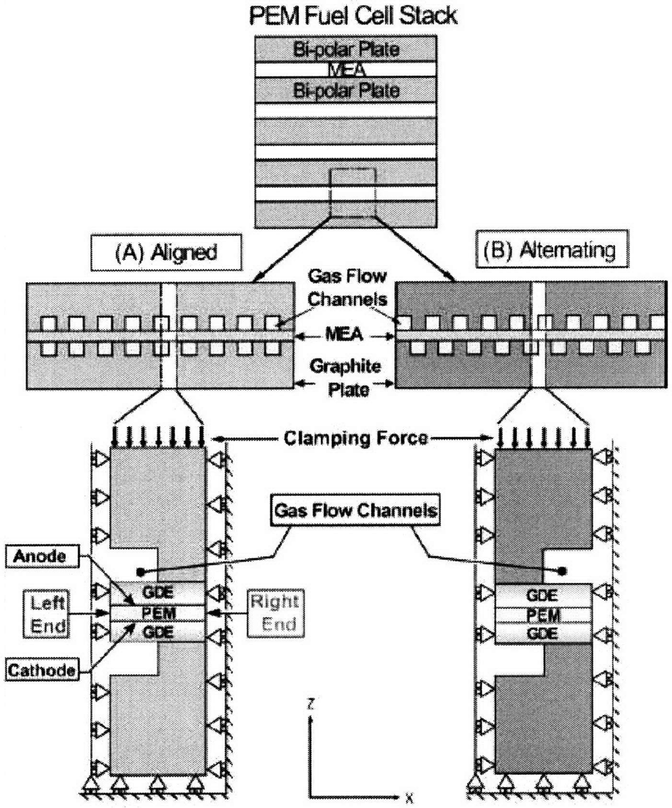

Figure 112: Repeat unit of fuel cell used in the simulations in Tang et. al. (May 2006) and Kusoglu et. al. (2006). The PEM is the Nafion membrane, the GDE is the combined gas diffusion layer and electrode, the MEA is the combination of the PEM and GDE. Aligned and alternating represent the two extremes for possible configurations of the anode and cathode side gas flow channels. In each case half a gas channel and half a confined area is taken as the repeat unit in the horizontal direction with the full MEA and half of a bipolar plate on each side taken as the repeat unit in the vertical direction.

6) All components are in contact but stress free at the start of the simulation.

The simulation was implemented in ABAQUS 6.7 explicit using CPE4R type elements (plane strain four node reduced integration).

The meshes that were used for the aligned and alternating configurations are shown in figures 113 and 114 respectively.

The hygro-thermal loading profile consists of eight steps:

1) Temperature and hydration within the membrane is increased from 25^oC and the reference dry state (taken at room temperature and humidity but actually containing some water molecules) to 80^oC and fully hydrated (15% hygro-swelling) over a period of 10 seconds.

2) The conditions are held constant for 10 seconds.

3) Temperature and hydration within the membrane are decreased back to 25^oC and "dry" over a period of 10 seconds.

4) The conditions are held constant for 10 seconds.

5-8) Steps one through four are repeated.

This loading sequence was chosen in order to explore what level of stress is reached in a fuel cell during startup, how much of that relaxes over time, what the shape and magnitude of the maximum membrane deformation is, what the deformation and stress is after shutdown, how much recovery/relaxation occurs over time, and how does each of these change upon the second cycle. Ideally this sort of startup-shutdown cycle would be simulated many more times and the times for each step would be varied parametrically, since this would be computationally expensive these particular conditions were chosen as a starting point. The temperatures and hydration levels are realistic for a fuel cell system, but the times are arbitrarily chosen.

5.2 Simulation Results

First we check our assumption that the deformation will be in the low to moderate strain level. Figure 115 shows the maximum in-plane strain for the first cycle loaded state for both the alter-

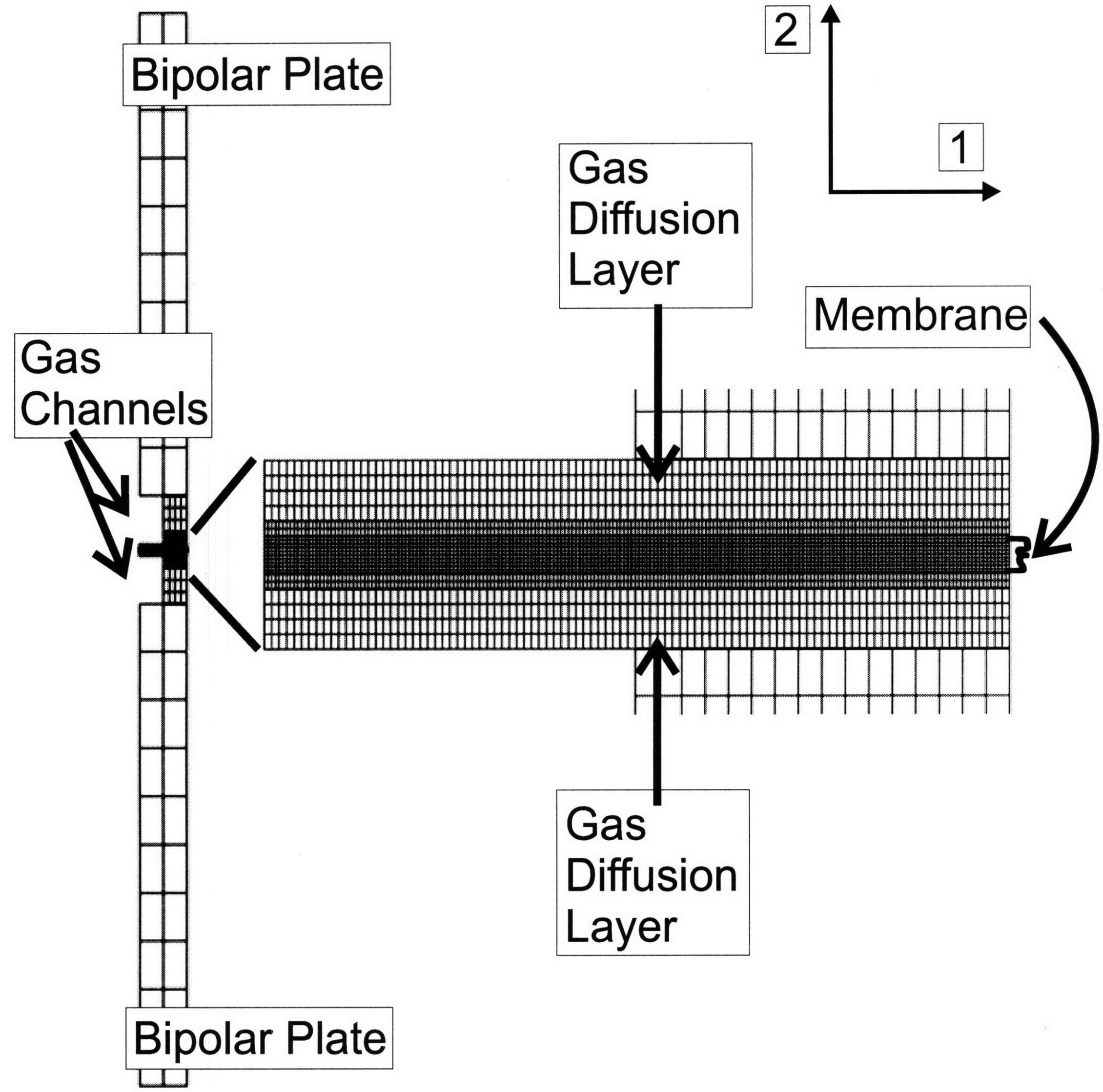

Figure 113: Mesh used for fuel cell unit simulation with aligned gas channels in the unloaded configuration.

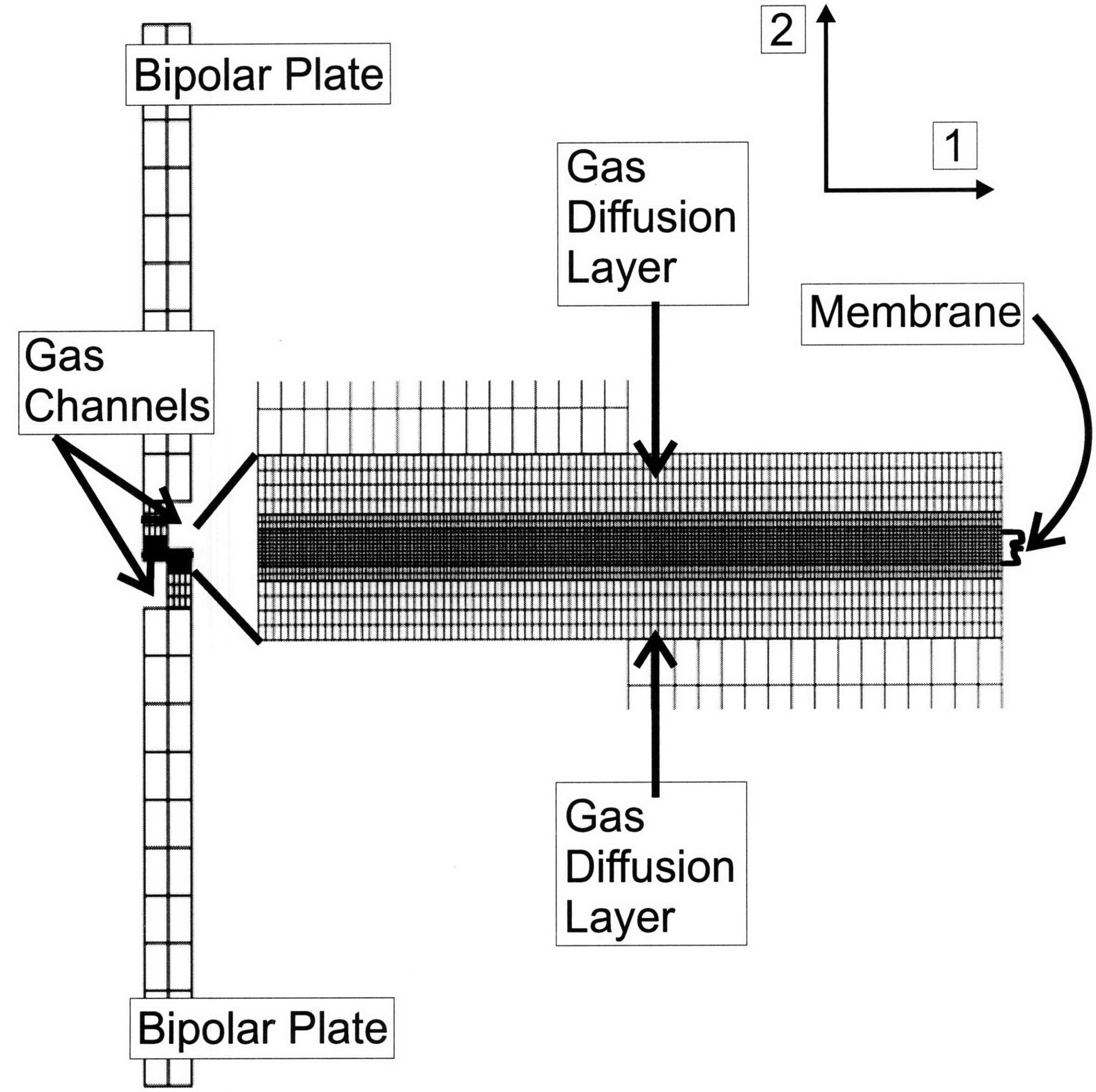

Figure 114: Mesh used for fuel cell unit simulation with alternating gas channels in the unloaded configuration.

(a) Alternating (b) Aligned

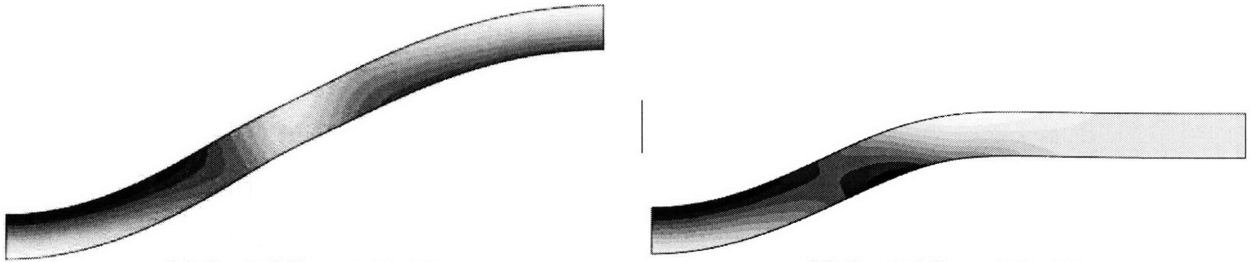

(c) $\theta = 80^oC$,$\varphi = 16$,t=10s (d) $\theta = 80^oC$,$\varphi = 16$,t=10s

Figure 115: Maximum principal strain throughout the hygro-thermal cycling for the alternating and aligned configurations.

nating and aligned gas channel configurations, this is the maximum strain state. The maximum strain reached is less than 0.5, approximately 0.15 of which is hygro-thermal swelling strain. This is pushing the limit of the model, but since this is the maximum value, the small to moderate strain assumption is taken as valid.

The Mises stress contours (which also show the deformation) for the full model in both alternating and aligned configurations are shown to give an overall assessment of the stresses present in each case (Figures 116 and 117). From these contour plots it is immediately obvious that there is a significant amount of non-uniform deformation and that the alignment (or lack there of) of the gas channels is important in determining the specifics of this deformation. Interestingly enough the peak stress is reached when the material in unloaded; this stress of $12MPa$ for both configurations is right around the yield stress at room temperature and humidity. Both the stress and deformation in the unloaded state increase upon the second cycle. There is also some visible stress relaxation during the time periods for which the loading conditions are held constant, however in each of those time periods the relaxation is small relative to the total stress. The aligned configuration has slightly higher stresses than the alternating configuration, particularly in the loaded state. In the unloaded configuration the aligned does not have the stress concentration at the center of the membrane that the alternating does. The membrane in the aligned configuration is less deformed in the unloaded state (this will be examined more closely in figure 123).

The Mises stress does not tell the whole story. Figures 118 and 119 compare the horizontal($\mathbf{T}_{11}$) , vertical($\mathbf{T}_{22}$), and in-plane shear ($\mathbf{T}_{12}$) stress components. The horizontal stress is the dominant stress in both the loaded state in which it is compressive and the unloaded state in which it is tensile. The horizontal stress in the aligned configuration is similar to the alternating while loaded, but is roughly two thirds the magnitude of the alternating horizontal stress when unloaded (note the difference in the contour ranges). These stresses are of roughly the same order, so the loaded compressive stress will be more likely to cause plastic deformation as the characteristic moduli are reduced at elevated temperature and water content. The vertical stress is primarily compressive in both loading and unloading and is in general close to an order of magnitude less than the horizontal stress as it has a greater freedom of motion of expand. In the aligned configuration the vertical stress is negligible on the non-constrained side. The in-plane shear stress is of the same order as the vertical stress; for the alternating configuration it is concentrated at the center at which the gas channel switches from being below to above it (looking left to right); for the aligned configuration there is a gentler gradient.

Since there is significant deformation it can be somewhat misleading to draw conclusions from the horizontal and vertical stresses since these are not aligned with the axes of the membrane. Figures 120 and 121 show the maximum principal stresses for the alternating and aligned configurations respectively. The maximum stress in the loaded state is tensile, the maximum stress in the unloaded state is compressive and is greater than the loaded state for both the alternating and aligned configurations.

The plastic deformation gradient when the membrane has been unloaded is shown for each cycle both immediately and after relaxation for the horizontal and vertical direction (Figures 122, 123). Plastic deformation is significant in both the horizontal and vertical directions but the vertical component is significantly larger, particularly in the positive direction. There is also an accumulation of plastic deformation in the second cycle versus the first as was inferred earlier from

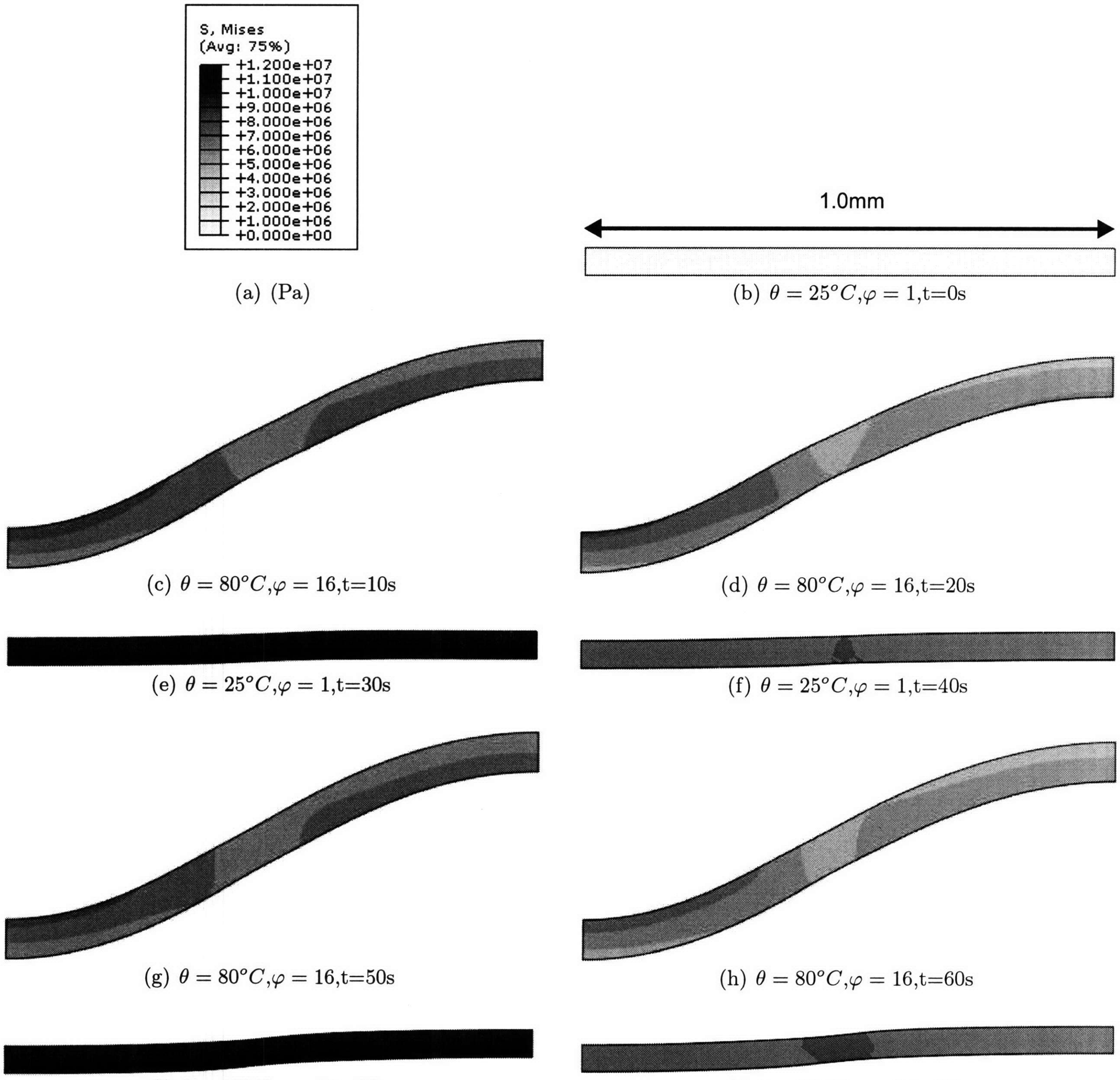

(a) (Pa)

(b) $\theta = 25^oC$,$\varphi = 1$,t=0s

(c) $\theta = 80^oC$,$\varphi = 16$,t=10s

(d) $\theta = 80^oC$,$\varphi = 16$,t=20s

(e) $\theta = 25^oC$,$\varphi = 1$,t=30s

(f) $\theta = 25^oC$,$\varphi = 1$,t=40s

(g) $\theta = 80^oC$,$\varphi = 16$,t=50s

(h) $\theta = 80^oC$,$\varphi = 16$,t=60s

(i) $\theta = 25^oC$,$\varphi = 1$,t=70s

(j) $\theta = 25^oC$,$\varphi = 1$,t=80s

Figure 116: Evolution of the deformation and Mises stress in the alternating configuration through time with the applied hygro-thermal cycling.

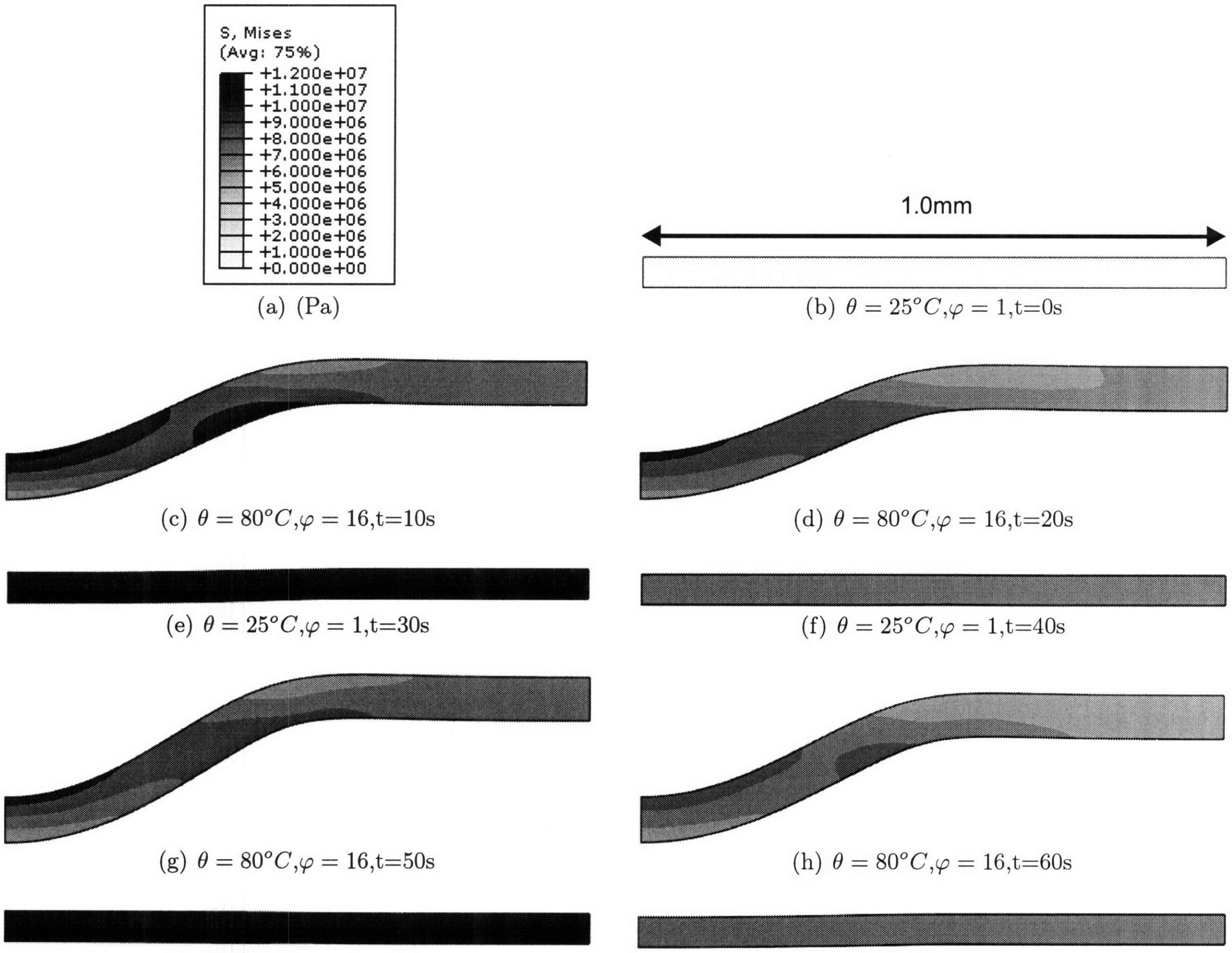

(a) (Pa)

(b) $\theta = 25^oC$,$\varphi = 1$,t=0s

(c) $\theta = 80^oC$,$\varphi = 16$,t=10s

(d) $\theta = 80^oC$,$\varphi = 16$,t=20s

(e) $\theta = 25^oC$,$\varphi = 1$,t=30s

(f) $\theta = 25^oC$,$\varphi = 1$,t=40s

(g) $\theta = 80^oC$,$\varphi = 16$,t=50s

(h) $\theta = 80^oC$,$\varphi = 16$,t=60s

(i) $\theta = 25^oC$,$\varphi = 1$,t=70s

(j) $\theta = 25^oC$,$\varphi = 1$,t=80s

Figure 117: Evolution of the deformation and Mises stress in the aligned configuration through time with the applied hygro-thermal cycling.

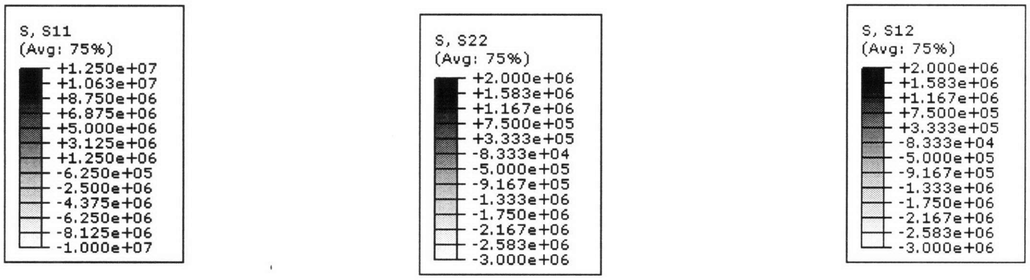

(a) $\mathbf{T}_{11}$ (Pa)

(b) $\mathbf{T}_{22}$ (Pa)

(c) $\mathbf{T}_{12}$ (Pa)

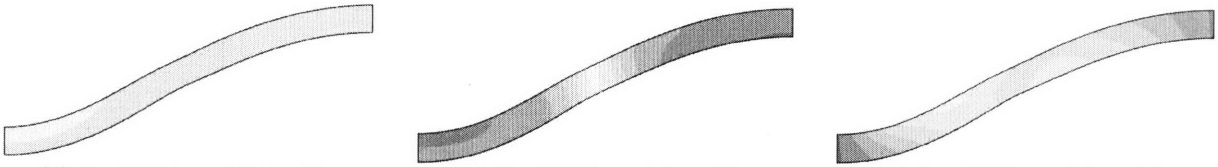

(d) $\theta = 80^{o}C$,$\varphi = 16$,$t = 20s$

(e) $\theta = 80^{o}C$,$\varphi = 16$,$t = 20s$

(f) $\theta = 80^{o}C$,$\varphi = 16$,$t = 20s$

(g) $\theta = 25^{o}C$,$\varphi = 1$,$t = 40s$

(h) $\theta = 25^{o}C$,$\varphi = 1$,$t = 40s$

(i) $\theta = 25^{o}C$,$\varphi = 1$,$t = 40s$

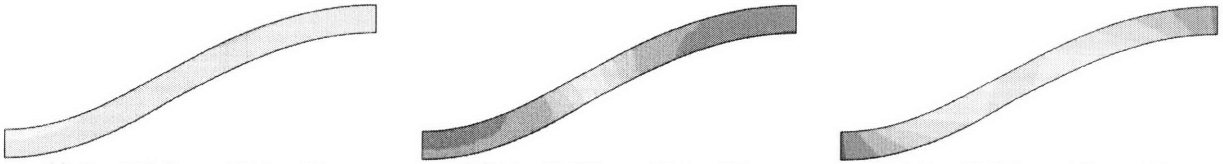

(j) $\theta = 80^{o}C$,$\varphi = 16$,$t = 60s$

(k) $\theta = 80^{o}C$,$\varphi = 16$,$t = 60s$

(l) $\theta = 80^{o}C$,$\varphi = 16$,$t = 60s$

(m) $\theta = 25^{o}C$,$\varphi = 1$,$t = 80s$

(n) $\theta = 25^{o}C$,$\varphi = 1$,$t = 80s$

(o) $\theta = 25^{o}C$,$\varphi = 1$,$t = 80s$

Figure 118: Comparison of the horizontal ($\mathbf{T}_{11}$), vertical ($\mathbf{T}_{22}$), and in-plane shear ($\mathbf{T}_{12}$) stress in the alternating configuration through time with the applied hygro-thermal cycling.

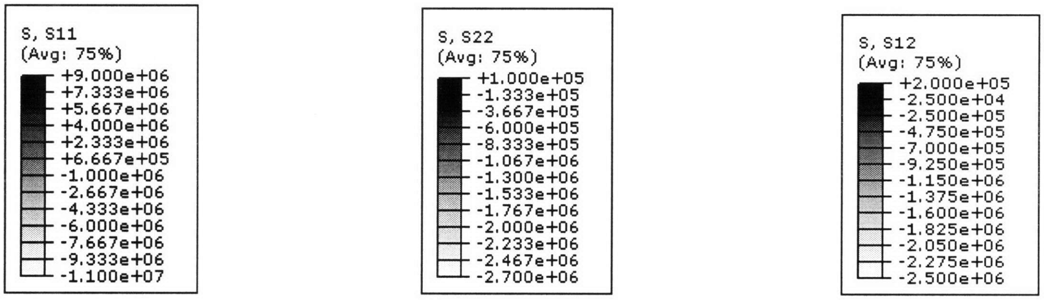

(a) $\mathbf{T}_{11}$ (Pa) (b) $\mathbf{T}_{22}$ (Pa) (c) $\mathbf{T}_{12}$ (Pa)

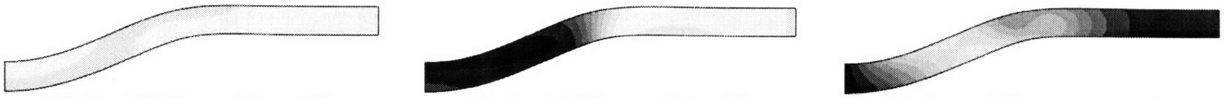

(d) $\theta = 80^oC$,$\varphi = 16$,$t = 20s$ (e) $\theta = 80^oC$,$\varphi = 16$,$t = 20s$ (f) $\theta = 80^oC$,$\varphi = 16$,$t = 20s$

(g) $\theta = 25^oC$,$\varphi = 1$,$t = 40s$ (h) $\theta = 25^oC$,$\varphi = 1$,$t = 40s$ (i) $\theta = 25^oC$,$\varphi = 1$,$t = 40s$

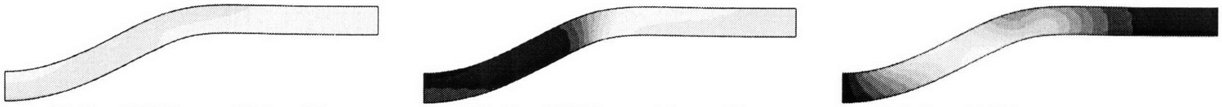

(j) $\theta = 80^oC$,$\varphi = 16$,$t = 60s$ (k) $\theta = 80^oC$,$\varphi = 16$,$t = 60s$ (l) $\theta = 80^oC$,$\varphi = 16$,$t = 60s$

(m) $\theta = 25^oC$,$\varphi = 1$,$t = 80s$ (n) $\theta = 25^oC$,$\varphi = 1$,$t = 80s$ (o) $\theta = 25^oC$,$\varphi = 1$,$t = 80s$

Figure 119: Comparison of the horizontal ($\mathbf{T}_{11}$), vertical ($\mathbf{T}_{22}$), and in-plane shear ($\mathbf{T}_{12}$) stress in the aligned configuration through time with the applied hygro-thermal cycling.

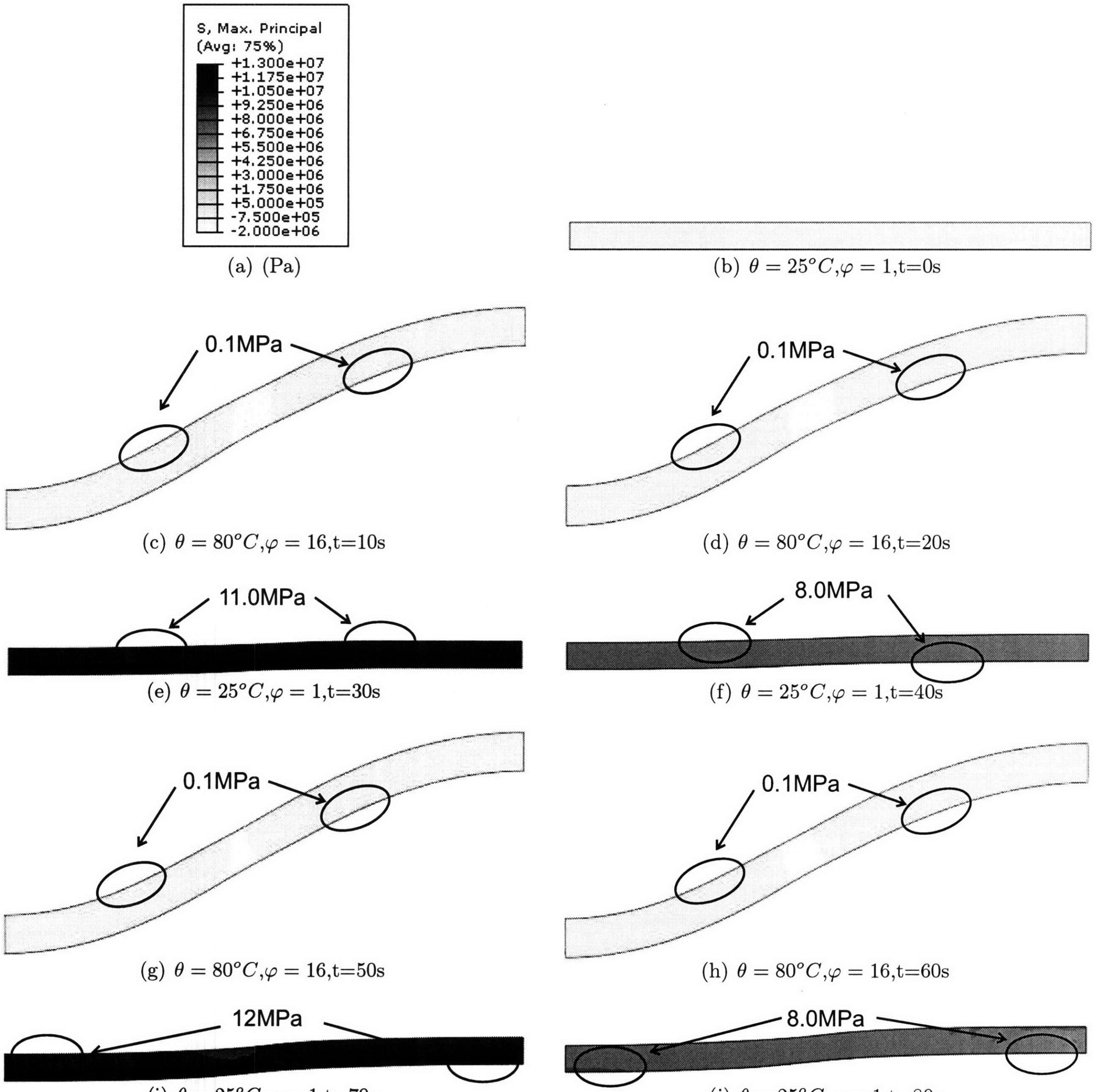

(a) (Pa)

(b) $\theta = 25^oC$,$\varphi = 1$,t=0s

(c) $\theta = 80^oC$,$\varphi = 16$,t=10s

(d) $\theta = 80^oC$,$\varphi = 16$,t=20s

(e) $\theta = 25^oC$,$\varphi = 1$,t=30s

(f) $\theta = 25^oC$,$\varphi = 1$,t=40s

(g) $\theta = 80^oC$,$\varphi = 16$,t=50s

(h) $\theta = 80^oC$,$\varphi = 16$,t=60s

(i) $\theta = 25^oC$,$\varphi = 1$,t=70s

(j) $\theta = 25^oC$,$\varphi = 1$,t=80s

Figure 120: Evolution of the maximum principal stress in the alternating configuration through time with the applied hygro-thermal cycling.

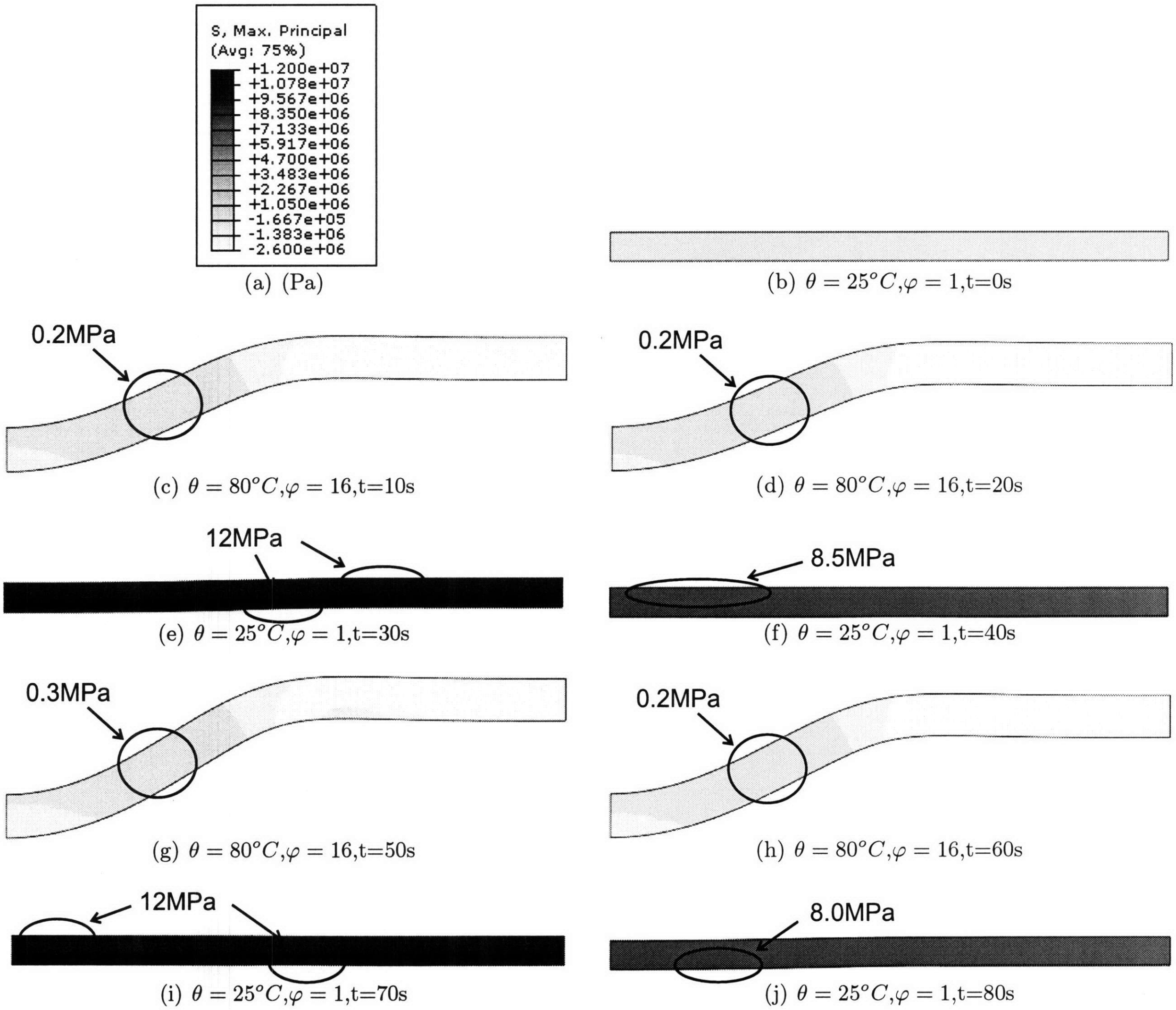

(a) (Pa)

(b) $\theta = 25^oC, \varphi = 1$,t=0s

(c) $\theta = 80^oC, \varphi = 16$,t=10s

(d) $\theta = 80^oC, \varphi = 16$,t=20s

(e) $\theta = 25^oC, \varphi = 1$,t=30s

(f) $\theta = 25^oC, \varphi = 1$,t=40s

(g) $\theta = 80^oC, \varphi = 16$,t=50s

(h) $\theta = 80^oC, \varphi = 16$,t=60s

(i) $\theta = 25^oC, \varphi = 1$,t=70s

(j) $\theta = 25^oC, \varphi = 1$,t=80s

Figure 121: Evolution of the maximum principal stress in the aligned configuration through time with the applied hygro-thermal cycling.

the stress contours. When comparing the plastic deformation between the alternating and aligned cases, it is again apparent that the alternating has a concentrated zone of deformation at the center that is not present in the aligned case. This manifests itself as a local expansive deformation in the horizontal direction and compressive deformation in the vertical direction. While the alternating deformation is symmetric about the center point as expected, the aligned deformation is significantly different on the side vertically constrained by the bipolar plate versus the side that is not vertically constrained by the bipolar plate (also as expected). The vertical plastic deformation is expansive on both sides with much larger deformation on the less constrained side. The horizontal plastic deformation is compressive on the side that is not restricted by the bipolar plate and expansive on the side that is restricted by the bipolar plate. This makes sense as the open side was allowed to expand more in the vertical direction than in the horizontal direction, so that when the hygro-thermal swelling is isotropically removed the resulting horizontal plastic deformation is compressive.

Negative hydrostatic pressure can result in cohesive failure, meaning it can lead to initiation of a cavitation event. We therefore plot the hydrostatic pressure in the unloaded state for both the alternating and aligned configurations (Figure 124). The alternating and aligned configurations have similar values for hydrostatic pressure with the aligned being slightly more negative. Figure 125 shows the hydrostatic pressure in the loaded states to be compressive everywhere. Hence, it is the cyclic plasticity which leads to a residual stress state upon unloading that results in the significant hydrostatic tension (negative pressure) of figure 124.

For the alternating configuration the effect of a stiffer gas diffusion layer is explored. An elastic modulus of four times the value is used. The stiffer GDL results in much less deformation during loading, slightly smaller plastic strains after unloading, a slightly more even distribution between horizontal and vertical stresses, and significantly larger stresses while loaded, but fairly a similar stresses when unloaded(Figures 128, 129).

A comparison of the elastic-hygro-thermal-viscoplastic model and the full model under the previously described boundary conditions reveals no qualitative difference and very little quantitative difference. Figures 130, 131 and 132 compare the Mises stress and the plastic deformation of the elastic-hygro-thermal-viscoplastic model with those of the full model. The partial model exhibits

(a) $\mathbf{F}^p_{11}$ (b) $\mathbf{F}^p_{22}$

(c) $\theta = 25°C, \varphi = 1, t = 30s$ (d) $\theta = 25°C, \varphi = 1, t = 30s$

(e) $\theta = 25°C, \varphi = 1, t = 40s$ (f) $\theta = 25°C, \varphi = 1, t = 40s$

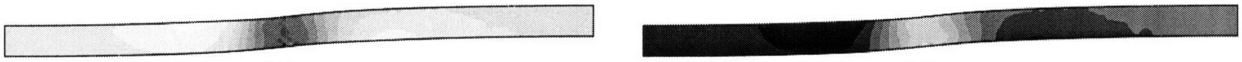

(g) $\theta = 25°C, \varphi = 1, t = 70s$ (h) $\theta = 25°C, \varphi = 1, t = 70s$

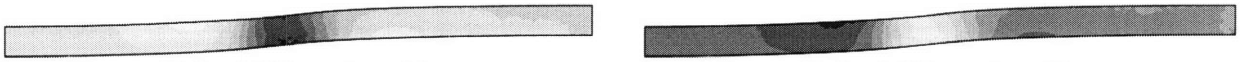

(i) $\theta = 25°C, \varphi = 1, t = 80s$ (j) $\theta = 25°C, \varphi = 1, t = 80s$

Figure 122: Comparison of the horizontal and vertical plastic deformation ($\mathbf{F}^p_{11}$ and $\mathbf{F}^p_{22}$) in the alternating configuration through time with the applied hygro-thermal cycling.

(a) $\mathbf{F}^p_{11}$ (b) $\mathbf{F}^p_{22}$

(c) $\theta = 25^oC$,$\varphi = 1$,$t = 30s$ (d) $\theta = 25^oC$,$\varphi = 1$,$t = 30s$

(e) $\theta = 25^oC$,$\varphi = 1$,$t = 40s$ (f) $\theta = 25^oC$,$\varphi = 1$,$t = 40s$

(g) $\theta = 25^oC$,$\varphi = 1$,$t = 70s$ (h) $\theta = 25^oC$,$\varphi = 1$,$t = 70s$

(i) $\theta = 25^oC$,$\varphi = 1$,$t = 80s$ (j) $\theta = 25^oC$,$\varphi = 1$,$t = 80s$

Figure 123: Comparison of the horizontal and vertical plastic deformation ($\mathbf{F}^p_{11}$ and $\mathbf{F}^p_{22}$) in the aligned configuration through time with the applied hygro-thermal cycling.

(a) Alternating (Pa)

(b) Aligned (Pa)

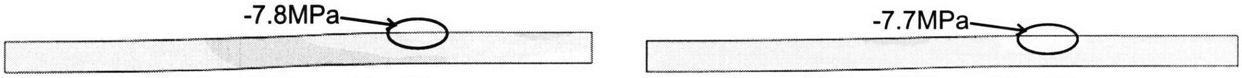

(c) $\theta = 25^oC$,$\varphi = 1$,$t = 30s$

(d) $\theta = 25^oC$,$\varphi = 1$,$t = 30s$

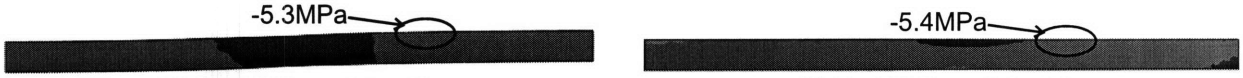

(e) $\theta = 25^oC$,$\varphi = 1$,$t = 40s$

(f) $\theta = 25^oC$,$\varphi = 1$,$t = 40s$

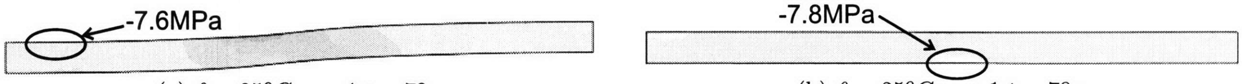

(g) $\theta = 25^oC$,$\varphi = 1$,$t = 70s$

(h) $\theta = 25^oC$,$\varphi = 1$,$t = 70s$

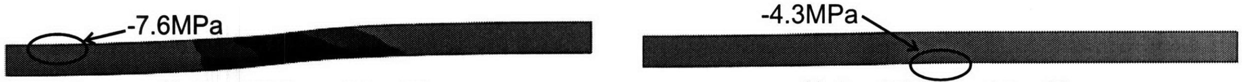

(i) $\theta = 25^oC$,$\varphi = 1$,$t = 80s$

(j) $\theta = 25^oC$,$\varphi = 1$,$t = 80s$

Figure 124: Comparison of hydrostatic pressure in the unloaded states for both the aligned and alternating configurations.

(a) Alternating (Pa) (b) Aligned (Pa)

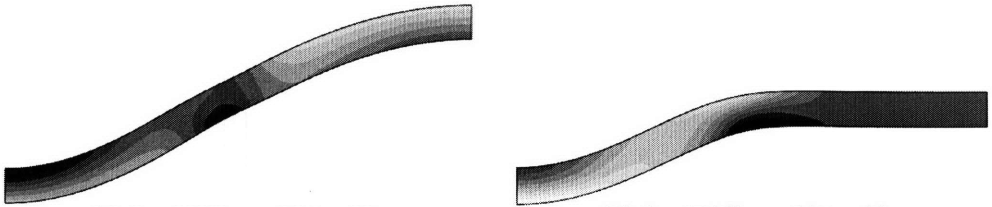

(c) $\theta = 80^oC$,$\varphi = 16$,$t = 10s$ (d) $\theta = 80^oC$,$\varphi = 16$,$t = 10s$

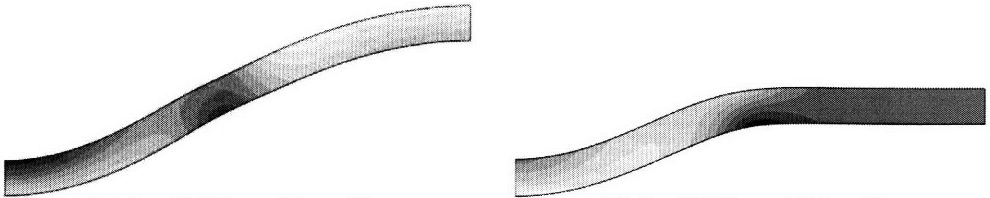

(e) $\theta = 80^oC$,$\varphi = 16$,$t = 20s$ (f) $\theta = 80^oC$,$\varphi = 16$,$t = 20s$

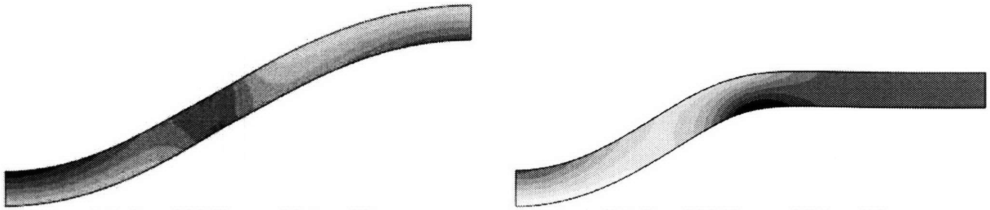

(g) $\theta = 80^oC$,$\varphi = 16$,$t = 50s$ (h) $\theta = 80^oC$,$\varphi = 16$,$t = 50s$

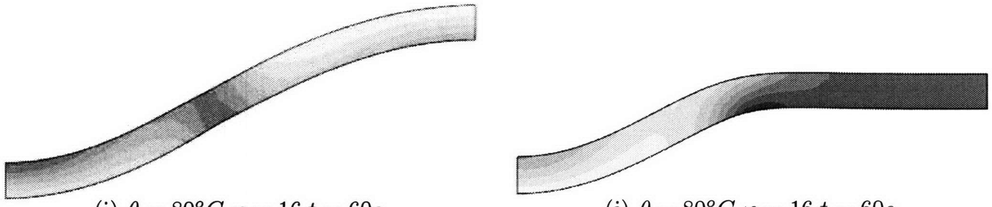

(i) $\theta = 80^oC$,$\varphi = 16$,$t = 60s$ (j) $\theta = 80^oC$,$\varphi = 16$,$t = 60s$

Figure 125: Comparison of hydrostatic pressure in the loaded states for both the aligned and alternating configurations.

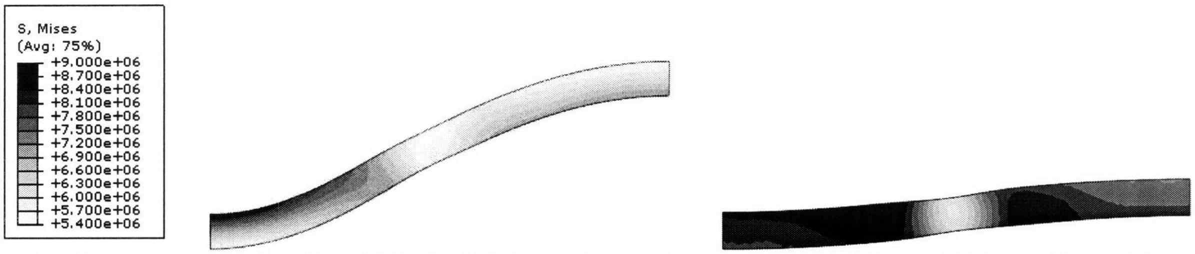

(a) (Pa) (b) Compliant GDL $\theta = 80^oC$,$\varphi = 16$,$t = 20s$ (c) Stiff GDL $\theta = 80^oC$,$\varphi = 16$,$t = 20s$

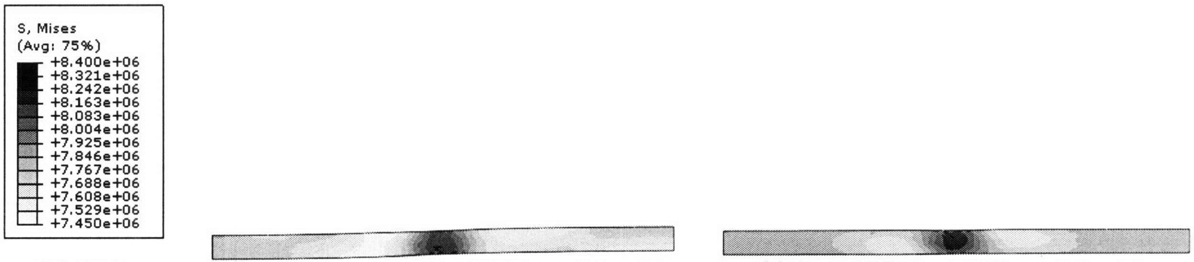

(d) (Pa) (e) Compliant GDL $\theta = 25^oC$,$\varphi = 1$,$t = 40s$ (f) Stiff GDL $\theta = 25^oC$,$\varphi = 1$,$t = 40s$

Figure 126: Comparison of the Mises stress for a compliant versus a stiff GDL in the alternating gas channels configuration.

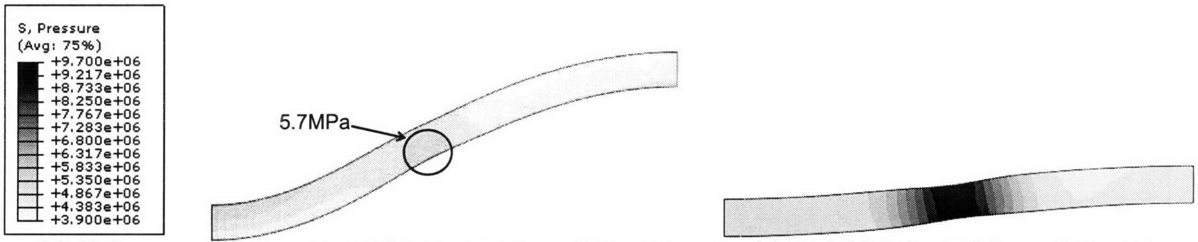

(a) (Pa) (b) Compliant GDL $\theta = 80^oC$,$\varphi = 16$,$t = 20s$ (c) Stiff GDL $\theta = 80^oC$,$\varphi = 16$,$t = 20s$

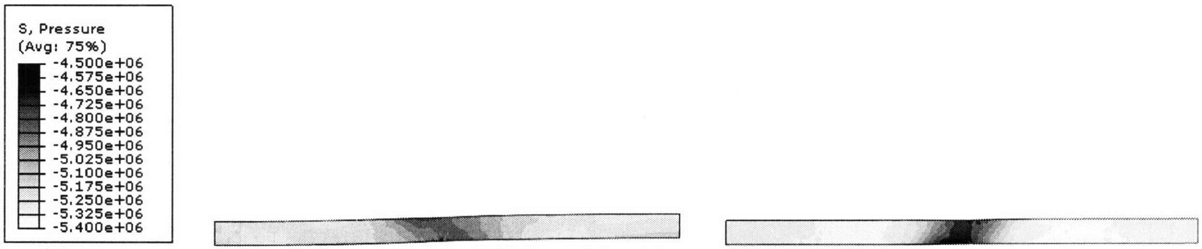

(d) (Pa) (e) Compliant GDL $\theta = 25^oC$,$\varphi = 1$,$t = 40s$ (f) Stiff GDL $\theta = 25^oC$,$\varphi = 1$,$t = 40s$

Figure 127: Comparison of the hydrostatic pressure for a compliant versus a stiff GDL in the alternating gas channels configuration.

(a) (Pa) (b) Compliant GDL $\theta = 80^oC$,$\varphi = 16$,$t = 20s$ (c) Stiff GDL $\theta = 80^oC$,$\varphi = 16$,$t = 20s$

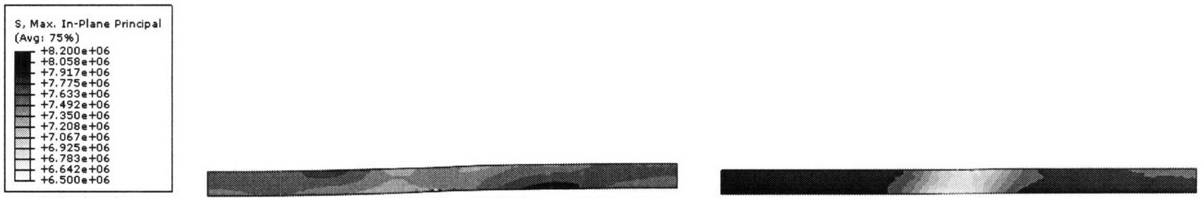

(d) (Pa) (e) Compliant GDL $\theta = 25^oC$,$\varphi = 1$,$t = 40s$ (f) Stiff GDL $\theta = 25^oC$,$\varphi = 1$,$t = 40s$

Figure 128: Comparison of the maximum principal stress for a compliant versus a stiff GDL in the alternating gas channels configuration.

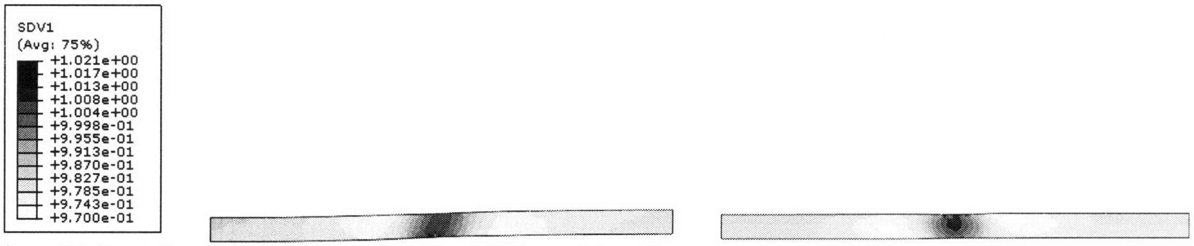

(a) Horizontal Plastic Deformation (b) Compliant GDL $\theta = 25^oC$,$\varphi = 1$,$t = 40s$ (c) Stiff GDL $\theta = 25^oC$,$\varphi = 1$,$t = 40s$

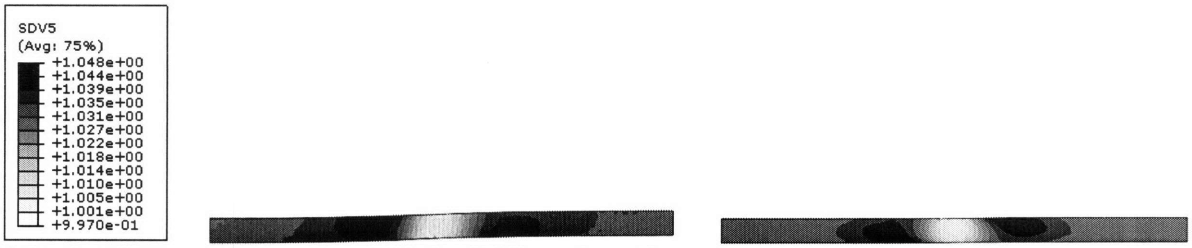

(d) Vertical Plastic Deformation (e) Compliant GDL $\theta = 25^oC$,$\varphi = 1$,$t = 40s$ (f) Stiff GDL $\theta = 25^oC$,$\varphi = 1$,$t = 40s$

Figure 129: Comparison of the horizontal and vertical plastic deformation ($\mathbf{F}^p_{11}$ and $\mathbf{F}^p_{22}$) for a compliant versus a stiff GDL in the alternating gas channels configuration.

slightly higher stresses at all points in time, but the difference is no more than a couple of percent, this can be at least partially attributable to the non-gradual yielding behavior which results in higher stress at strains below 0.1. The plastic deformation is slightly greater for the elastic-hygro-thermal-viscoplastic model than for the complete model, but again, this is not a large difference.

These results seem to indicate that there is not a significant difference between the two models, however, the prescribed loading conditions results in a relatively fast effective strain rate, it would be expected that the major difference between the two models would occur over longer time periods. To that end we both models through a single cycle in which the temperature and hydration are increased as before, but they are unloaded over a period of 100 seconds rather than 10 seconds. The stress states at the end of unloading are compared in figure 133. Given 100 seconds to unload rather than the 10 seconds of the above simulations, the elastic-hygro-thermal-viscoplastic and the complete models show significantly different quantitative results (although qualitatively they are still very similar). The complete model has larger Mises and maximum principal stresses and hydrostatic pressure than the partial model. There is almost no difference in the vertical plastic deformation between the two models. The horizontal plastic deformation is more uniform for the complete model than for the partial model.

The parameters explored in this chapter are really just the start of possibilities for the applications of the Nafion material model developed in chapter 4. Channel alignment and gas diffusion layer compliance for a double hygro-thermal cycle were varied while looking at a variety of measures which might be early predictors/indicators of MEA failure. These outputs included the Mises stress, maximum principal stress, hydrostatic pressure, and plastic deformation. Through these simulations the assumption that the deformation is in the small to moderate strain regime was confirmed with mechanical strains reaching around 0.35. The likelihood of a cumulative damage scheme was also confirmed with plastic deformation in the unloaded state increasing upon the second cycle. While the gas channel alignment changed the stress distribution, both the alternating and aligned configurations had similar magnitude stress components, and hydrostatic pressure on both loading and unloading, and plastic deformation upon unloading. In both cases the membrane has considerable freedom to deform in the vertical direction and little freedom to deform in the

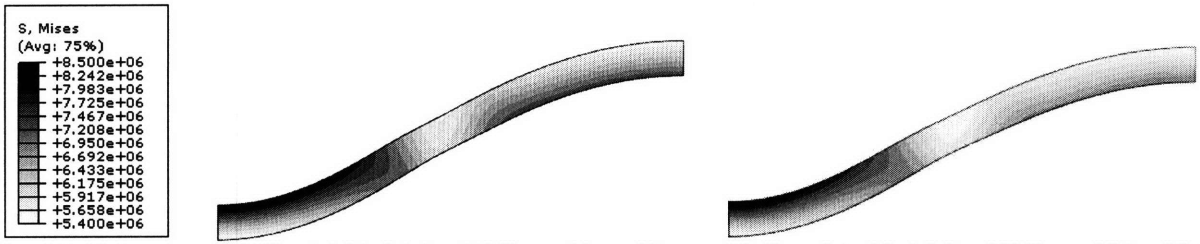

(a) (Pa) (b) Partial Model $\theta = 80^oC$,$\varphi = 16$,$t = 20s$ (c) Complete Model $\theta = 80^oC$,$\varphi = 16$,$t = 20s$

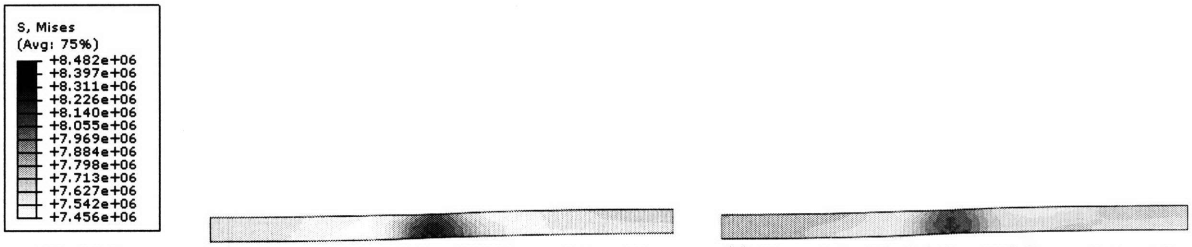

(d) (Pa) (e) Partial Model $\theta = 25^oC$,$\varphi = 1$,$t = 40s$ (f) Complete Model $\theta = 25^oC$,$\varphi = 1$,$t = 40s$

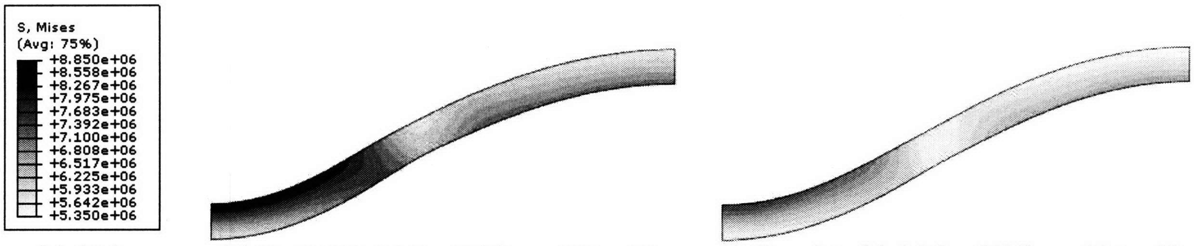

(g) (Pa) (h) Partial Model $\theta = 80^oC$,$\varphi = 16$,$t = 60s$ (i) Complete Model $\theta = 80^oC$,$\varphi = 16$,$t = 60s$

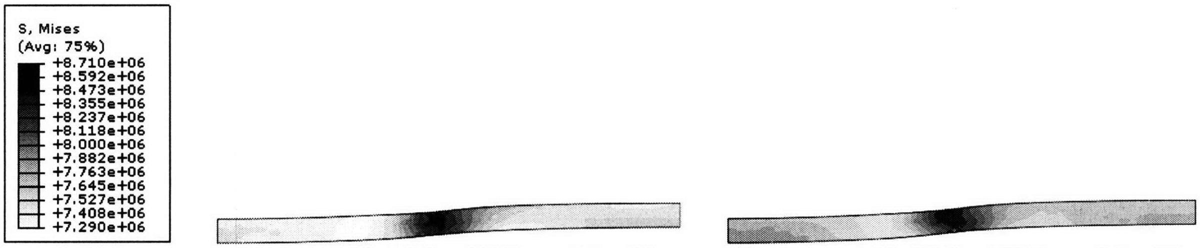

(j) (Pa) (k) Partial Model $\theta = 25^oC$,$\varphi = 1$,$t = 80s$ (l) Complete Model $\theta = 25^oC$,$\varphi = 1$,$t = 80s$

Figure 130: Comparison of the Mises stress of the elastic-hygro-thermal-viscoplastic model and the full model with alternating gas channels.

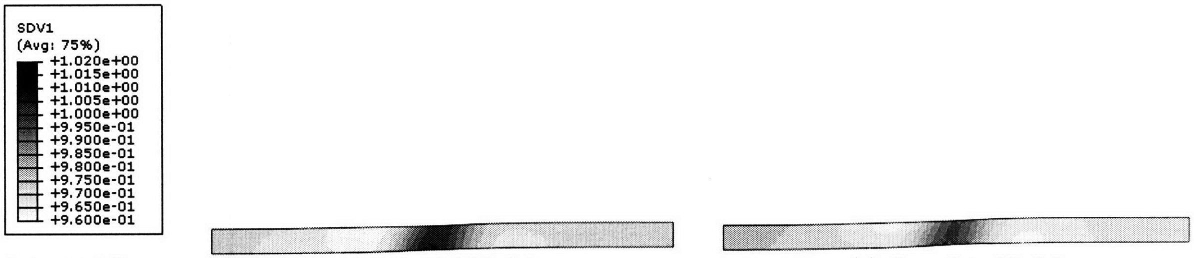

(a) $\theta = 25^oC$,$\varphi =$ 1,$t = 30s$

(b) Partial Model

(c) Complete Model

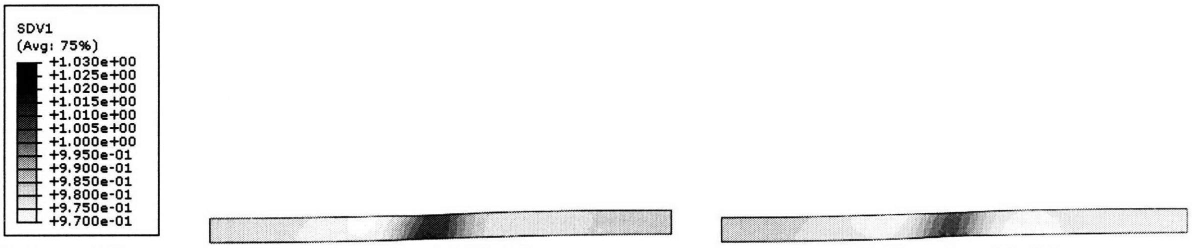

(d) $\theta = 25^oC$,$\varphi =$ 1,$t = 40s$

(e) Partial Model

(f) Complete Model

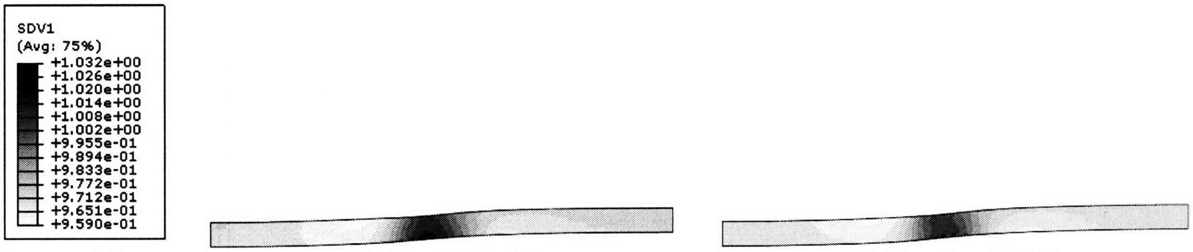

(g) $\theta = 25^oC$,$\varphi =$ 1,$t = 70s$

(h) Partial Model

(i) Complete Model

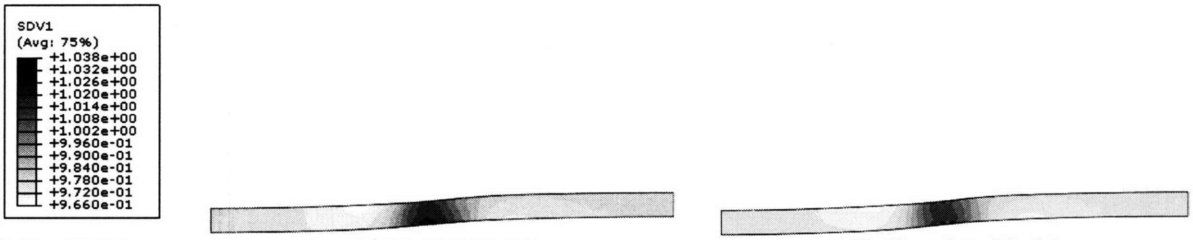

(j) $\theta = 25^oC$,$\varphi =$ 1,$t = 80s$

(k) Partial Model

(l) Complete Model

Figure 131: Comparison of the horizontal deformation gradient $\mathbf{F}^p_{11}$ of the elastic-hygro-thermal-viscoplastic model and the full model with alternating gas channels.

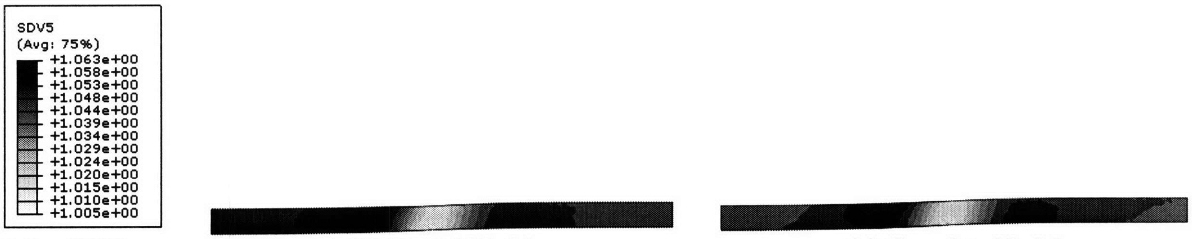

(a) $\theta = 25^oC$,$\varphi =$ 1,$t = 30s$ (b) Partial Model (c) Complete Model

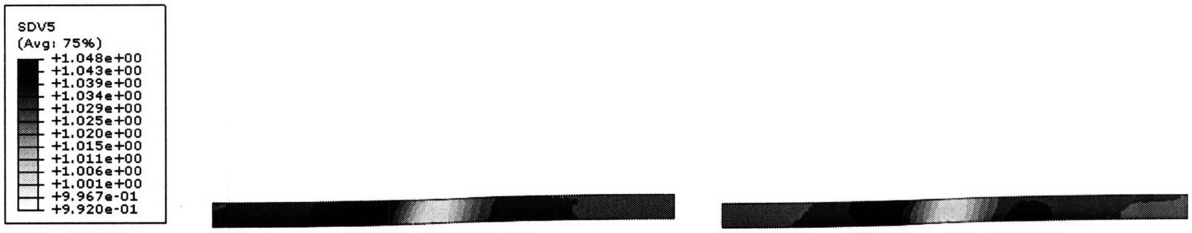

(d) $\theta = 25^oC$,$\varphi =$ 1,$t = 40s$ (e) Partial Model (f) Complete Model

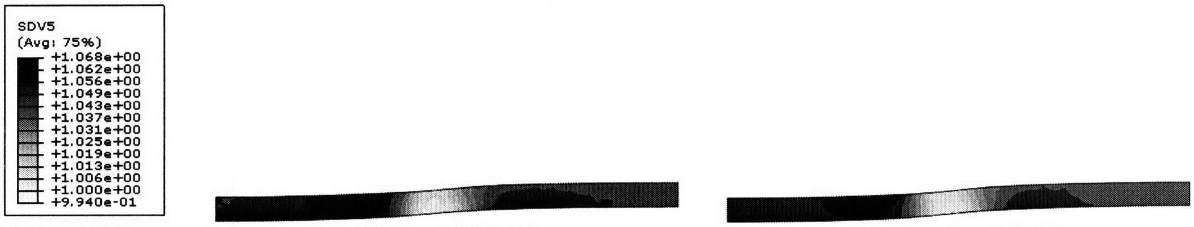

(g) $\theta = 25^oC$,$\varphi =$ 1,$t = 70s$ (h) Partial Model (i) Complete Model

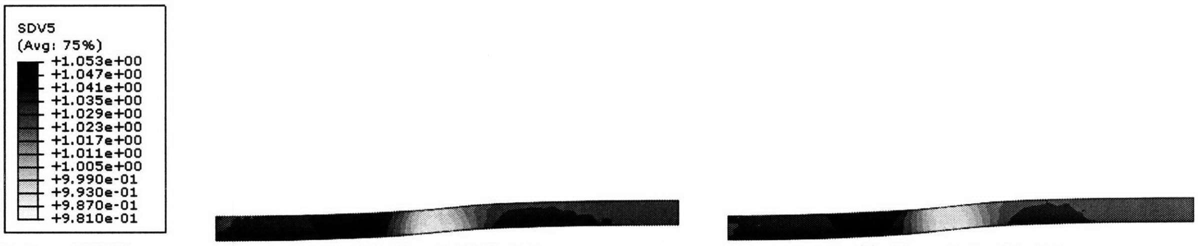

(j) $\theta = 25^oC$,$\varphi =$ 1,$t = 80s$ (k) Partial Model (l) Complete Model

Figure 132: Comparison of the vertical deformation gradient $\mathbf{F}^p_{22}$ of the elastic-hygro-thermal-viscoplastic model and the full model with alternating gas channels.

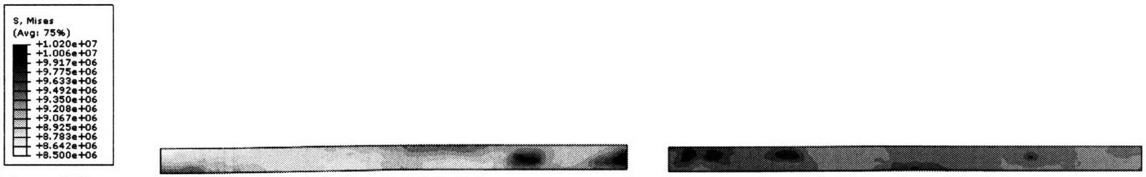

(a) Mises Stress (Pa) (b) Partial Model (c) Complete Model

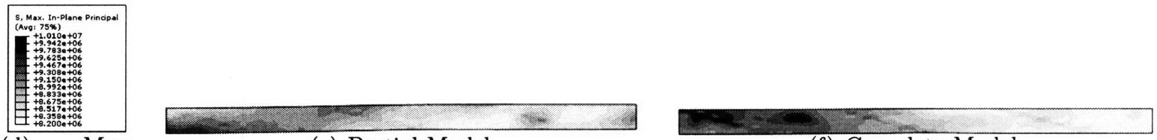

(d) Max Principal Stress (Pa) (e) Partial Model (f) Complete Model

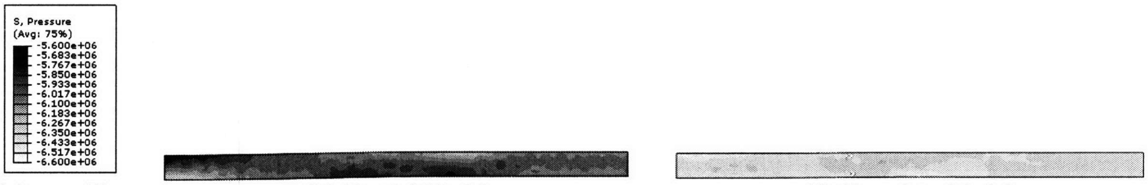

(g) Hydrostatic Pressure (Pa) (h) Partial Model (i) Complete Model

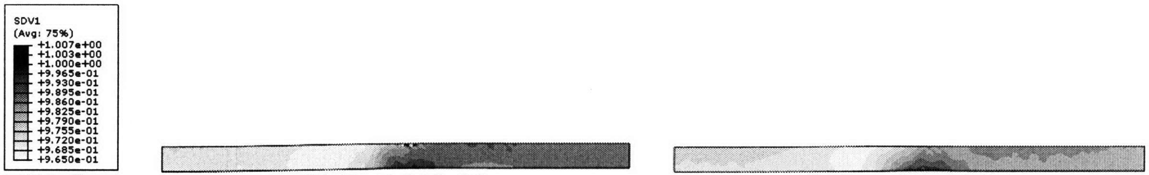

(j) $\mathbf{F}^p_{11}$ (k) Partial Model (l) Complete Model

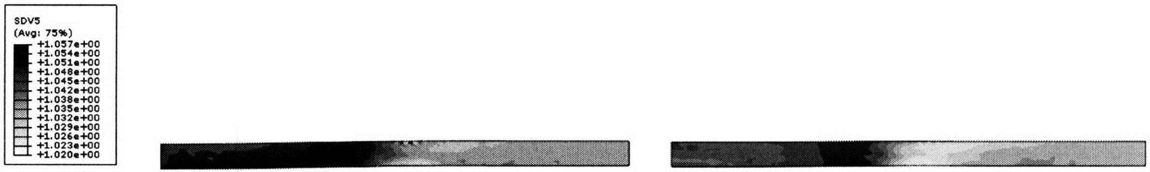

(m) $\mathbf{F}^p_{22}$ (n) Partial Model (o) Complete Model

Figure 133: Comparison of the partial and complete model at $\theta = 25^oC$,$\varphi = 1$,$t = 120s$ for $10s$ load, $10s$ hold and $100s$ unload (a-c) Mises stress, (d-f) maximum principal stress, (g-i) hydrostatic pressure (j-l) Horizontal plastic deformation ($\mathbf{F}^p_{11}$) (m-o) Vertical plastic deformation ($\mathbf{F}^p_{22}$).

horizontal direction. Decreasing the compliance of the gas diffusion layer significantly decreased the strain and increased the stress in the loaded condition, but made relatively little difference once unloaded. Even with this decreased compliance vertical deformation still faces much less resistance than horizontal deformation.

6 Conclusions and Future Work

A comprehensive set of uniaxial tensile tests was conducted on NRE212 to characterize the time, temperature, and hydration dependent mechanical behavior of recast Nafion. The stress-strain behavior was found to be strongly dependent on all three. In monotonic tensile loading, the stress-strain curve shows an initial linear elastic response, a gradual yielding, and strain hardening. The yield point is rate dependent with the yield stress and yield strain both increasing with increasing strain rate. The initial elastic slope and strain hardening slope do not have a significant rate dependence at room temperature. Under cyclic loading conditions the material exhibits a nonlinear elastic unloading and reloading, the basic character of this behavior is largely independent of strain rate, but does evolve with strain. An increase in temperature was found to decrease the elastic modulus and yield stress, and increase the yield strain and stress relaxation. An increase in hydration was found to decrease the elastic modulus, yield stress, and rate of stress relaxation and slightly increase the strain hardening slope.

The as-received material was compared to that put through a chemical pre-treatment procedure typically used by researchers trying to optimize fuel cell performance. The pre-treatment made no qualitative difference in the mechanical behavior, but did reduce the stress response of the material across the board.

X-ray diffraction analysis was conducted during tensile tests in order to understand the micromechanical mechanisms that correspond to the observed macroscopic mechanical behavior. Three peaks are observed, one in the SAXS and two in the WAXS, all of which are isotropic prior to deformation of the material. Using literature as a guide the SAXS peak is assigned to a diffraction from intra-cluster spacing from the phase separated sulfonic acid side groups; the low angle WAXS peak is assigned as the superposition of diffractions from the crystalline and amorphous intermolecular backbone spacing; the wide angle WAXS peak is assigned as diffractions from a few different characteristic intramolecular crystalline backbone spacings. All three peaks evolve when uniaxial tensile strain is applied; this evolution indicates that ionic clusters are becoming elliptical with the major axis in the direction of applied strain and that the backbone is aligning in the direction of applied strain. More specifically, the backbone motion is observed, through cyclic and stress relaxation tests, to correlate directly with strain, whereas the cluster shape change has a more complex relation that seemed to depend on both stress and strain. Backbone bundles deform and align with the strain as evidenced by their direct relation with strain during loading, unloading, and relaxation. In contrast, the ionic clusters evolve with strain and with stress where, for example, during the fixed strain condition of a stress relaxation test, there is cluster evolution during stress relaxation, implying that the portion of stress that relaxes is recovery from the cluster regions.

Using the mechanical and xray data in conjunction with information available in the literature, an existing conceptual model for Nafion under deformation was modified to better capture the micromechanical mechanisms. In this model bundles of the backbone are believed to rotate and align around the clusters as strain is applied and the clusters deform into an elliptical shape (with major axis aligned with the maximum principal strain). As strain is increased some of the backbone segments shear away from the cluster to which they are originally attached. When the applied load is removed the degree of recovery will depend both on the amount of shearing that has occurred and the freedom of motion of the backbone and clusters (i.e. the temperature and hydration).

From this conceptual model the first constitutive model for Nafion which accounts for the rate sensitivity and viscoplastic properties was developed. The model is able to capture all the major features of the tensile experimental data including non-linear loading, unloading, and reloading, strain rate dependent yield, strain dependent relaxation and cyclic behavior, and temperature and hydration dependent elastic modulus, yield, strain hardening, and stress relaxation.

Both the simplest and the fully developed constitutive model are then applied to a simulated fuel cell unit. The simulation confirms the phenomenology by which plastic strain is accumulated through each hygro-thermal cycle. The stress components both during loading and unloading are on the order of that required for yield, particularly in the horizontal direction which is constrained from expanding and contracting by the bipolar plates.

The Nafion material model and its application in a simulated fuel cell unit has provided us with an idea of the magnitude of stresses and strains experienced by the membrane in a fuel cell and a likely mechanism for accumulated failure. From here there are three important paths forward. Firstly, the model needs to be expanded to include water content as an output parameter rather than an input. In this simulation it was assumed that the water content at 80^oC inside the fuel cell would be the same as that at 80^oC in an unconstrained environment, while clearly the externally applied stresses would change the water the membrane could hold. It is also unrealistic to assume a uniform water distribution across the membrane. There are three main factors that determine the water distribution: electro-osmotic drag, water generation at the cathode, and diffusion. Electro-osmotic drag is the process by which protons conducted across the membrane drag water molecules across with them. This is related to the vehicular conduction mechanism mentioned in the introduction which makes Nafion a low resistance membrane when hydrated. The water generation at the cathode is the product of the chemical reaction among the hydrogen protons, electrons, and oxygen necessary for the completion of the fuel cell system of reactions. The water present at the cathode depends both on the current being generated by the fuel cell (i.e. the rate of reaction) and the water management system in place to remove the excess water (which otherwise will flood the gas channels and prevent oxygen from reaching the membrane). The diffusion acts to counter these first two forces both of which cause water to accumulate towards the cathode side of the membrane; diffusion drives water from areas of high concentration to areas of lower concentration. The rate of diffusion depends on the magnitude of the water gradient as well as the average hydration level, temperature, and external stresses. These non-uniformities could be causing greater stress concentrations leading to locally accumulated plastic deformation and therefore accelerating failure.

Within the context of short-term design solutions, this material model can be used to evaluate the effects of varying the boundary conditions on the membrane. To name a few possibilities, the bipolar plates and gas diffusion layers can be made of different materials, the gas channels can be arranged differently and with different aspect ratios, and the MEA can be assembled at elevated temperature or humidity. The final chapter of this thesis begins to look at this issue with the alternating versus aligned gas channels and the variation of gas diffusion layer stiffness, but there is a much broader set of parameters that can be varied.

The material model developed here can also help to guide longer term design of membranes to replace Nafion. Since it appears that the hygro swelling is the main driver of the plastic deformation, a material could be developed that does not need water for rapid proton conduction, needs water but does not swell nearly as much in its presence, or does swell but exhibits purely elastic behavior. The difficulty of course lies in designing a material that meets one of these three criteria without sacrificing electrochemical performance.

7 References

Elliott J.A., Hanna S., Elliott A.M.S., & Cooley G.E. (2000). Interpretation of the Small-Angle X-ray Scattering from Swollen and Oriented Perfluorinated Ionomer Membranes. *Macromolecules, 33,* 4161-4171.

Gasteiger H. & Mathias M. (2003). Fundamental research and development challenges in polymer electrolyte fuel cell technology, Materials for High Temperature PEM Fuel Cells. *The Energy Institute, Penn State University.*
Heijden P.C., Rubatat L., & Diat O. (2004). Orientation of Drawn Nafion at Molecular and Mesoscopic Scales. *Macromolecules, 37,* 5327-5336.

Halim J., & Scherer G.G. (1994). Characterization of Recast Nafion Films by Small- and Wide-Angle X-ray Scattering. *Macromolecular Chemistry and Physics, 195,* 3783-3788.

Haubold H.G., Vad T., Jungbluth H., & Hiller P. (2001). Nano Structure of Nafion: a SAXS Study. *Electrochimica Acta, 46,* 1559-1563.

Huang X., Solasi R., Zou. Y, Feshler M., Reifsnider K., Condit D., Burlatsky S., & Madden T. (2006) Mechanical Endurance of Polymer Electrolyte Membrane and PEM Fuel Cell Durability. *Journal of Polymer Science: Part B: Polymer Physics, 44,* 2346-2357.
Hsu W.Y. & Gierke T.D. (1982). Elastic Theory for Ionic Clustering in Perfluorinated Ionomers. *Macromolecules, 15,* 101-105.
James P.J., Elliot J.A., McMaster T.J., Newton J.M., Elliot A.M.S., Hanna S., & Miles M.J. (2000). Hydration of Nafion Studied by AFM and X-ray Scattering. *Journal of Materials Science, 25,* 5111-5119.

Kundu S., Simon L.C., Fowler M., & Grot S. (2005). Mechanical Properties of Nafion Electrolyte Membranes Under Hydrated Conditions. *Polymer, 46,* 11707-11715.

Kusoglu A., Karlsson A.M., Santare M.H., Cleghorn S., & Johnson W.B. (2006). Mechanical Response of Fuel Cell Membranes Subjected to a Hygro-Thermal Cycle. *Journal of Power Sources, 161,* 987-996.

Liu D., Hickner M.A., Case S.W. & Lesko J.J. (2006). Relaxation of Proton Conductivity and Stress in Proton Exchange Membranes Under Strain. *Journal of Engineering Materials and Technology, 128,* 503-508.

Liu D., Kyriakides S., Case S.W., Lesko J.J., Li Y., & McGrath J. (2006). Tensile Behavior of Nafion and Sulfonated Poly(arylene ether sulfone) Copolymer Membranes and Its Morphological Correlations. *Journal of Polymer Science Part B: Polymer Physics, 44,* 1453-1465.

Morris D.R., & Sun, X.J. (1993) Water-Sorption and Transport Properties of Nafion 117-H. *Journal of Applied Polymer Science, 50,* 1445-1452.
Page K.A., Landis F.A., Phillips A.K., & Moore R.B. (2006). SAXS Analysis of the Thermal Relaxation of Anisotropic Morphologies in Oriented Nafion Membranes. *Macromolecules, 39,* 3939-3946.

Porat Z., Fryer J.R., Huxham M., & Rubinstein I. (1995). Electron Microscopy Investigation of the Microstructure of Nafion Films. *Journal of Physical Chemistry 99,* 4667-4671.

Rubatat L., Rollet A.L., Gebel G., &Diat O. (2002). Evidence of Elongated Polymeric Aggregates in Nafion. *Macromolecules, 35,* 4050-4055.

Satterfield M.B., Majsztrik P.W., Ota H., Benziger J.B., & Bocarsly A.B. (2006). Mechanical Properties of Nafion and Titania/Nafion Composite Membranes for Polymer Electrolyte Membrane Fuel Cells. *Journal of Polymer Science Part B: Polymer Physics, 44,* 2327-2345.
Takamatsu T. & Eisenberg A. (1979) Density and Expansion Coefficients of Nafion Polymers. *Journal of Applied Polymer Science, 24,* 2221-2235.

Tang Y., Karlsson A.M., Santare M.H., Gilbert M., Cleghorn S., & Johnson W.B. (2006). An Experimental Investigation of Humidity and Temperature Effects on the Mechanical Properties of Perfluorosulfonic Acid Membranes. *Materials Science and Engineering A. 45,* 297-304.

Tang Y., Santare M.H., Karlsson A.M., Cleghorn S., & Johnson W.B. (2006). Stresses in Proton Exchange Membranes Due to Hygro-Thermal Loading. *Journal of Fuel Cell Science and Technology, 119,* 119-124.

Yeo S. & Eisenberg A. (1977). Physical Properties and Supermolecular Structure of Perfluorinated Ion-Containing (Nafion) Polymers. *Journal of Applied Polymer Science, 21,* 875-898.

Weber A.Z. & Newman J. (2004). A Theoretical Study of Membrane Constraint in Polymer-Electrolyte Fuel Cells. *Materials, Interfaces, and Electrochemical Phenomena, 50,* 3215-3226.